THE CHEMICAL AND PHYSICAL PROPERTIES OF THE OH, CN AND C_2 JETS IN COMET HALE-BOPP (1995 O1)

By

SUSAN MARIA LEDERER

A DISSERTATION PRESENTED TO THE GRADUATE SCHOOL
OF THE UNIVERSITY OF FLORIDA IN PARTIAL FULFILLMENT
OF THE REQUIREMENTS FOR THE DEGREE OF
DOCTOR OF PHILOSOPHY

UNIVERSITY OF FLORIDA

2000

Copyright 2000

by

Susan Maria Lederer

This is dedicated to my family, who has supported me during every step of my education and my life.

ACKNOWLEDGEMENTS

My sincerest thanks go to Dr. Humberto Campins who agreed to advise me even when his schedule was quite full, and who continued his role as my advisor long after his commitments to UF had passed. He taught me to think as an independent scientist, yet guided me and encouraged me through the difficult times. He has remained an active, committed advisor in my research, and his guidance has been invaluable. I would also like to thank Drs. David Schleicher, David Osip, Michael A'Hearn, and Stephen Larson for their guidance in observational astronomy, cometary science, and my research project. My research would not have progressed without the input of all these people.

I would like to thank my committee members, Drs. Elizabeth Lada, Richard Elston, Stanley Dermott, and Martin Vala. I particularly thank Dr. Lada for her help as my pseudo-advisor in Dr. Campin's absence, Dr. Vala who agreed to sit on my committee only months before my final defense, and Dr. Jonathan Williams who agreed to sit in on my defense for Dr. Lada with less than a week's notice.

I would also like to thank Dr. Casey Lisse who was always willing to discuss my research, and who spent many hours filling my thesis with red ink to improve its contents. I wish to thank Drs. Amy Lovell and Nalin Samarasinha for helpful discussions and their willingness to share pieces of their Monte Carlo codes. I also thank Jeff Julian for his amazing ability to create 3D figures, and for his willingness to help in any way at a moment's notice. Dr. Larry Wasserman (Lowell Observatory) also deserves credit for helping me solve never-before-seen problems while observing at 3 a.m. I also thank him for sharing his ephemerides program and altering it to generate additional information that was crucial to my Monte Carlo routines. I

would also like to express my appreciation for Amy Newberry, whose expertise in the English language helped improve not only the grammar, but also cut down the infinite number of commas scattered through this thesis.

Any acknowledgement would be incomplete without mention of all of the people at the University of Florida. Thanks to the dedication of our office staff, including Glenda, Ann, Audrey and Debra – I was always registered for classes on time, was always paid, and was able to travel to distant lands (and not-so-distant lands). My officemates, Scott, James, Jim, and Elisha, made the long hours in the space sciences building enjoyable with enlightening conversations ranging from Gator football to the possibility of life existing in the universe, and everything in between.

I cannot begin to list all the friends who have given me support throughout this thesis. I am very grateful for David, Teresa, Alexes and Krystina Ciardi for making me part of their family, always keeping the door open for me, and feeding me many healthy meals throughout the last two years. I thank Joanna Levine for many stress-relieving mocha breaks. I am also indebted to the many friends who have continuously encouraged me from afar, including Bob Thompson, Sean Powell, Sheila Snow, Jamie Ballard, and Melissa Benedict. This list would not be complete without mentioning Barb Colba (my favorite teacher), who taught me that learning was fun and school was cool at the ripe old age of 5, and continues to support me from afar even today.

I am deeply grateful for my extended family who supported me throughout my entire education. I thank my father, Ken, and mother, Kath (whose spirit will always be with me), for encouraging me to learn from childhood through graduate school. They will always be close friends as well as parents. I particularly thank my dad for encouraging me to follow my insatiable curiosity about the physical world and heavens and enter the world of research. He knew I would be happiest in a profession where learning never ends. My mom taught me that excelling to be your

best is always the most rewarding, despite peer pressure. She was always there with a comforting hug or smile, despite the difficulties. I thank my sister, Jennifer, for playing the role of confidant, in every respect, throughout my life and often after midnight; my brother, Matthew, for challenging me to think and grow; and my sister, Katie, for her openness in life and her enveloping hugs. I would also like to thank Lou for showing me support when I barely knew him, and for emanating a passion for life that has influenced us all. I also wish to express my gratitude to my fictive family, Karin, Dave, Katie, Ben, and Meghan Olson, who has been my second family throughout my entire life. I also wish to thank my parents; grandparents, Walter Schneider and Mary Lederer; and my aunt and uncle, Ruth and Dean Twedt – their generosity and support allowed me to gain the fullest education possible. Without them, I'm sure my educational endevours would have lasted years longer. Finally, I wish to thank David Schwenk for his infinite patience throughout the final stages of my dissertation; for his support of my work and my life; and for his infectious smile, energy, and love. These are the people who helped me maintain my sanity and drive, and to whom I will always be indebted.

TABLE OF CONTENTS

ACKNOWLEDGEMENTS iv

LIST OF TABLES ix

LIST OF FIGURES x

ABSTRACT xii

CHAPTERS

1 INTRODUCTION 1

1.1 The Oort Cloud and Kuiper Belt 5
1.2 Properties of the Coma 5
1.2.1 Cometary Jets 6
1.2.2 Comet Hale-Bopp 8
1.2.3 OH as a Tracer of H_2O 10
1.2.4 Jet Source: Gas or Grain? 12
1.3 Synopsis 14

2 OBSERVATIONS AND DATA REDUCTION 15

2.1 Facilities and Instrumentation 15
2.2 Data Reduction 16
2.2.1 Initial Data Reduction 16
2.2.2 Absolute Calibration 23
2.2.3 Image Processing and Enhancement Routines 25
2.3 Projected Expansion Velocities 26
2.4 Summary 30

3 MONTE CARLO MODELING 31

3.1 Introduction 31
3.1.1 Haser Model 32
3.1.2 Vectorial Model 32
3.1.3 Hydrodynamic Models 33
3.1.4 Monte Carlo Model 34
3.2 Monte Carlo Models Developed for This Work 34
3.2.1 Gas Source Versus Grain Source 35
3.2.2 Non-collisional Isotropic Model 36
3.2.3 Collisions 40
3.2.4 Collisional Jet Models 47

3.3 Summary 50

4 ANALYSIS AND DISCUSSION 53

4.1 Introduction 53
4.2 Data Analysis 54
4.2.1 Jet Identification 54
4.2.2 Comparing the Morphology of OH, CN, and C_2 62
4.2.3 Jet Widths 67
4.2.4 Evolution of the Jets with Time 68
4.3 Monte Carlo Model Analysis 70
4.3.1 Gas versus CHON Grain Source 73
4.3.2 Initial Parent Velocity and Alpha Parameter 83
4.3.3 Range of Initial Parent Velocities 86
4.3.4 Daughter Velocity 86
4.3.5 Lifetimes of Parent and Daughter 89
4.3.6 Radiation Pressure 94
4.3.7 Phase Angle, PA_{Sun}, Sun's Cometocentric Location 94
4.3.8 Number and Positions of the Active Areas 98
4.3.9 Opening Angle of the Active Areas 101
4.3.10 Strength of the Jets and Solar Insolation 102
4.4 Results 103
4.4.1 Expansion Velocities and Jet Widths 103
4.4.2 Projected Locations of Active Areas on the Nucleus . . . 107
4.4.3 Jet Source: Gas vs Grain 116
4.5 Discussion 129
4.5.1 Morphology 129
4.5.2 Effect on Production Rates 132
4.5.3 Composition of the nucleus and extended source 133
4.5.4 Implications for the Heterogeneity of the Nucleus 134
4.6 Summary 136

5 CONCLUSIONS 137

5.1 Introduction 137
5.2 New Results 138
5.3 Directions for Future Work 140

APPENDIXES

A DUST PRODUCTION ($Af\rho$) 143

B THE HASER MODEL 145

REFERENCES 147

BIOGRAPHICAL SKETCH 155

LIST OF TABLES

1-1 Branching ratios of water 11

2-1 Narrowband filter characteristics 17

2-2 Comet Hale-Bopp observing details 17

3-1 Monte Carlo model parameter space 38

3-2 Collisional cross sections 46

4-1 Species-dependent model input parameters 72

4-2 Model input parameters 72

4-3 Projected expansion velocities 104

4-4 Projected jet widths 107

4-5 Locations of model active areas 109

4-6 Haser model production rates 134

LIST OF FIGURES

2-1 March time sequence 28

3-1 Monte Carlo model: Collisional and non-collisional models 48

3-2 Radial profiles of data and best-fit models (April 26, 1997) 51

4-1 OH, CN, and C_2 data (March 6, 1997) 55

4-2 OH, CN, and C_2 data (April 26, 1997) 56

4-3 OH data with various image processing techniques applied 58

4-4 CN data with various image processing techniques applied 59

4-5 C_2 data with various image processing techniques applied 60

4-6 Continuum data with various image processing techniques applied . . 61

4-7 Gas images before and after continuum correction (March 6, 1997) . . 63

4-8 Gas images before and after continuum correction (April 26, 1997) . . 64

4-9 CN continuum contamination analysis 66

4-10 Radial profile of jets 69

4-11 OH data and models with gas and triangular CHON grain jet sources 74

4-12 CN data and models with gas and triangular CHON grain jet sources 75

4-13 C_2 data and models with gas and triangular CHON grain jet source . 76

4-14 Radial profiles of the data and best-fit models for all gas species . . . 77

4-15 Radial profiles of OH data and models in the sunward direction . . . 78

4-16 Radial profiles of OH data and models in the anti-sunward direction . 79

4-17 Radial profiles of CN data and models in the sunward direction . . . 80

4-18 Radial profiles of CN data and models in the anti-sunward direction . 81
4-19 Radial profiles of C_2 data and models in both directions 82
4-20 Acceleration (α) parameter analysis (images) 84
4-21 Acceleration (α) parameter analysis (radial profiles) 85
4-22 Range of initial parent velocities parameter analysis (images) 87
4-23 Daughter velocity parameter analysis (images) 88
4-24 Daughter velocity parameter analysis (radial profiles) 90
4-25 Parent lifetime parameter analysis (radial profiles) 92
4-26 Daughter lifetime parameter analysis (radial profiles) 93
4-27 Radiation pressure parameter analysis (images) 95
4-28 Cometocentric coordinate system 97
4-29 Sun-Comet-Earth geometry between March 1 and May 1, 1997 99
4-30 Phase angle and position angle parameter analysis (images) 100
4-31 Opening angle parameter analysis (images) 102
4-32 OH, CN, and C_2 images in (r,θ) space 105
4-33 Radial profiles used to calculate expansion velocity 106
4-34 CN active area parameter analysis (images) 111
4-35 C_2 active area parameter analysis (images) 112
4-36 OH active area parameter analysis (images) 114
4-37 OH data and models with gas, CHON grain, and icy grain source jets 119
4-38 Data and models with nucleus-peaked CHON source 124
4-39 Data and models with triangular CHON grain source (April 22, 1997) 125
4-40 Data and models with triangular CHON grain source (April 23, 1997) 126
4-41 Data and models with triangular CHON grain source (April 26, 1997) 127

Abstract of Dissertation Presented to the Graduate School
of the University of Florida in Partial Fulfillment of the
Requirements for the Degree of Doctor of Philosophy

THE CHEMICAL AND PHYSICAL PROPERTIES
OF THE OH, CN AND C_2 JETS IN
COMET HALE-BOPP (1995 O1)

By

Susan Maria Lederer

December 2000

Chairman: Dr. Humberto Campins
Major Department: Astronomy

Comet Hale-Bopp is the brightest comet observed in the last 25 years, and has afforded us an opportunity to gain new insights into the physical and chemical properties of comets. Coma jets are evident in continuum (dust), CN, C_2 images, and for the first time in any comet, in OH narrowband images. In this study, the source of the coma jets is investigated through Monte Carlo modeling. An extended source that does not peak in productivity at the nucleus, combined with a nuclear gas source, is required to reproduce the data for all three gas species. Sub-micron organic CHON grains are the favored candidate for the extended source. Results from Monte Carlo modeling indicate that approximately 40% of the OH, 50% of the C_2, and 75% of the CN is produced by the extended source. The balance for each is created by a nuclear gas source. Compared with the nuclear gas source, the composition of the extended source is depleted in OH by a factor of $\sim$4 to 7, and depleted in C_2 by a factor of $\sim$2.

Jet width and projected expansion velocities are estimated. The latter indicates that the gases in the coma accelerate to distances of at least 100,000 km from the nucleus. Comet Hale-Bopp's high production rates and large collisional zone explain the acceleration in the coma.

The number (5) and the locations of the gas jets necessary to reproduce the observed coma morphology for all three species are constrained for images taken during April, 1997. Four of the five active areas on the comet's surface appeared to be emitting the same relative mixture of OH, CN, and C_2. The fifth area (located at $\sim 12°$S latitude) is richer in OH than the other active areas. This suggests that the composition of the nucleus is not entirely homogeneous. A high thermal inertia, which would allow production of the radicals throughout the cometary night, is not necessary to explain the existence of the anti-sunward gas jets. Instead, active areas that exist in near-twilight conditions throughout the comet's rotation period produce the bulk of the anti-sunward morphology.

CHAPTER 1
INTRODUCTION

The word comet is derived from the Greek word $\kappa o \mu \varepsilon \tau \epsilon$, meaning "the long-haired one." Comets are some of the most beautiful and inspiring objects in the heavens, however, historically they have been feared and viewed as bad omens. Today we know they are remnants from the formation of our planetary system.

Comets are among the most chemically and physically primitive members of our solar system. Astronomers study comets for clues about the conditions prevalent in the early solar nebula, about 4.5 billion years ago. With this in mind, many questions arise: Can we obtain any information concerning the amount of processing each comet has gone through, thus resulting in departures from its original primitive state? If so, can we work backwards to learn about its primitive state for clues about the conditions present when the comet formed early in the solar system's history? Is the coma created by a homogeneous or heterogeneous nucleus? What does this say about how the comet formed and about the evolution it has undergone since then? What can we learn about the physics and chemistry responsible for creating the coma?

Beyond the intellectual quest to understand comets and the to understand history of the solar system, comets are interesting objects that relate directly to not only the Earth as we know it today, but will likely play a role in the Earth's future as well. Two key ingredients necessary for life on Earth reside in comets: water and organic molecules; comets are regarded as a possible source for both ingredients on Earth.

It has been proposed that most of the Earth's water came from comets bombarding the planet during the final stages of the Earth's formation (e.g., Bockelée-Morvan et al. 1998, Delsemme 1999).[1] Studies of the deuterium content in comets can be used to estimate how much cometary water was supplied to the Earth during the period of heavy bombardment. In situ mass spectrometer measurements of Comet Halley (Eberhardt et al. 1995) and radio spectroscopy of Comets Hyakutake (Bockelée-Morvan et al. 1998) and Hale-Bopp (Meier et al. 1998) of HDO yielded a surprisingly similar deuterium to hydrogen ([D]/[H]) isotopic abundance ratio of $\sim 3 \times 10^{-4}$. This value is in line with the [D]/[H] ratio of dense cores of molecular clouds. The [D]/[H] ratio of the solar nebula, on the other hand, is an order of magnitude lower (Bockelée-Morvan et al. 1998). The observed [D]/[H] ratios imply that the ices incorporated in comets consist of material that formed in the cores of dense molecular clouds, and that the material has not undergone the same processing as the inner solar nebula. The value for Earth's oceans lies between the two (approximately half that of the cometary [D]/[H] ratio), at a value much higher than expected for a planet that formed in the solar nebula. Because the Earth's [D]/[H] ratio is lower than that found in comets, some argue that comets cannot be the sole, or even primary, source of water on the Earth. However, Delsemme (1999) suggests that the [D]/[H] ratio in comets that formed in Jupiter's zone was diminished to values consistent with the water in the Earth's oceans, and that comets from this reservoir may have supplied most of the water on Earth (80%); Comets Halley, Hyakutake and Hale-Bopp do not represent this class of comets.

Oró (1961) proposed that the organic material necessary for life to form on Earth may have been transported to the inner solar system from the outer solar system. Studies of the atmosphere of the early Earth suggest that it was not conducive

[1]Water and organics delivered *before* the final stages of Earth's formation were lost in the hot environment that existed during the Earth's initial stages of formation.

to the production of primitive organic material (Chang et al. 1983), though it was suitable for sustaining life. There are indications that the concentration of organics increases with heliocentric distance, beginning with the asteroid belt at 2.7 AU, continuing with the satellites of the giant planets, and ending with comets in the outer reaches of the solar system (Hartman et al. 1987, Huebner 1990). Analysis of mass spectrometer data taken during the Comet Halley flybys indicates that dust comprises 10% of the mass of the nucleus, and that organic (CHON only) grains comprise about 6 to 40% the mass of cometary dust (Huebner 1990); however, the mass spectrometers may not have sampled the large particles well. More recent evidence shows that there is a gradient of dust compositions ranging from grains composed of predominantly organic material to organic/silicate mixtures (including silicate grains with an organic mantle) to predominantly silicate dust (Lawler 1993). Sixty to eighty percent of the particles detected by the mass spectrometer are estimated to be either CHON grains or CHON-silicate mixtures. Chyba (1990) and Oró (1999) discuss the possibility that comets were the source of prebiotic organics delivered to the Earth. Some scientists question whether cometary organics would survive an impact with the Earth. While arguments have been posed both for and against this possibility, it appears likely that organics incorporated in impacting comets, whose diameters are less than a few hundred meters, would survive (Chyba and Sagan 1997).

Comets are a rich resource of organic material and volatiles which may have made life on Earth possible billions of years ago. Once again, these objects may be needed to support life in space in the future. Roughly 80% of nucleus is water ice, therefore these objects could be a valuable resource to any long-term manned missions in the future.

While comets may have contributed to the formation of life on Earth, they almost certainly have been a cause of death as well. It seems that an asteroid or a comet was responsible for the demise of the dinosaurs 65 million years ago (Alvarez et

al. 1980, Wickramasinghe and Wallis 1994, Sharpton and Marin 1997). A sedimentary layer unusually rich in iridium marks the Cretaceous/Tertiary (K/T) boundary and is coincident with the extinction of the dinosaurs as well as other species. The elevated level of iridium, which is also found in meteorites and is very rare in the Earth's crust, suggests that a non-terrestrial object such as a comet or an asteroid was responsible for the global devastation. The discovery of a crater in the Yucatan peninsula that is associated with the KT boundary, the 300 km Chicxulub crater, supports this theory (Izett 1991, Alvarez et al. 1992, Blum et al. 1993). Such events may occur as often as every few million years (Crovisier and Encrenaz 2000).

Impacts by much smaller objects are less devastating, and are much more common. Unquestionably, comets have impacted the Earth in the past; comets are believed to be a source of some craters still evident on Earth's surface (Spray, Kelly, and Rowley 1998). Early in the 20th century, an explosion 8 km above a forest in Siberia flattened more than a thousand square kilometers of forest. This explosion, known as the Tunguska event, released energy equivalent to 10 megatons of TNT. No remnant impactor was found, as would be expected for a small, low tensile strength object such as a comet or small meteoroid (Huebner 1990). Fortunately, this explosion occurred over an unpopulated region of the Earth.

We were reminded of the reality that comets are a threat to Earth when Comet Shoemaker-Levy 9 impacted Jupiter in July 1994. We do not yet have a system to intercept a comet if we were to find one on a collision course with Earth. We do not know whether comets are a relatively solid dirty ice-ball, or if they are rubble piles held together by a miniscule amount of gravity and a very low tensile strength; nor do we have an accurate knowledge of their composition. However, cometary research, and information that will result from four spacecraft missions bound for comets over the next decade, will greatly increase our knowledge of comets. We can use research designed to understand the nature of the composition, density, and tensile strength of

comets to prepare ourselves to deflect comets so their orbits do not intersect Earth's orbit if the need arises in the future.

1.1 The Oort Cloud and Kuiper Belt

There are two known reservoirs of comets in the solar system. The first was proposed by Jan Oort in 1950. By tracing the orbits of about 20 comets backwards in time, he was able to show that their orbits were originally quasi-parabolic. This placed their original perihelia well beyond the orbits of any planets in our solar system. The Oort cloud is now known to be a vast reservoir of comets with a spherical distribution. Perhaps as many as 10^{12} comets, whose semi-major axes are as large as 40,000 to 100,000 AU from the Sun, reside in the Oort cloud (Crovisier and Encrenaz 2000). These comets originally formed between Jupiter and Neptune, and were subsequently ejected by the giant planets into the Oort cloud.

The second source of comets is the Edgeworth-Kuiper Belt (EKB). It is a disk of comets whose orbits lie beyond Neptune's orbit, where they formed. These may represent the planetesimals that formed at the outer edge of the solar nebula where the density of the planetesimals and nebula was too low to encourage the formation of another planet. The EKB was theorized to exist by both Kenneth Edgeworth (1949) and Gerard Kuiper (1950). The first Kuiper Belt object was discovered in 1992, confirming the existence of the EKB (Jewitt and Luu 1993). Since then, hundreds of Kuiper Belt objects have been discovered (e.g., Tegler and Romanishin 1998, 1999).

1.2 Properties of the Coma

All cometary activity originates in the nucleus. However, the direct study of cometary nuclei is difficult primarily because of the presence of a coma when the comet is active, and because the comet is faint when it is inactive far from the Sun. The most common way to sample the nucleus remotely is by analyzing

the material that vaporizes into the coma. Therefore, many of the chemical and physical properties of the nucleus and regions on the nucleus where the activity of the comet originates (nuclear source function) are inferred from studies of the coma. By studying the morphology of cometary comae, we can address questions about the initiation, evolution, and termination of active areas on the nucleus, and the processes that may alter the comet's activity level (from the active state to dormancy to extinction). We can also investigate the chemical and physical properties of the active regions, jets, and the ejecta; temporal variations; possible migration of the active regions on the nucleus; and their effects on the evolution of the nucleus and coma. (Sekanina 1991).

1.2.1 Cometary Jets

The comae of some comets are diffuse and featureless; in others, spiral shapes, fans, and other coma jet morphology are observed. Discrete active areas on the surfaces of cometary nuclei eject concentrations of gas and dust, creating the jets we observe. The interplay of the locations of active areas on an irregularly shaped rotating body viewed at various phase angles from the Earth may also affect the morphology we observe. Dust jets have been observed in many comets (e.g., Halley, Swift-Tuttle, and Hale-Bopp); unambiguous gas jets, on the other hand, have only recently been discovered. The first report of collimated gas jets in a comet without an associated dust jet was presented by A'Hearn et al. (1986b) for Comet Halley. Since then, CN, C_2, and C_3 jets have been reported in Comet Halley by several authors (A'Hearn et al. 1986a,b, Cosmovici et al. 1988 Hoban et al. 1988). In Comet Halley, two of the three CN jets did not coincide spatially with dust jets observed at visible wavelengths; A'Hearn et al. also noted that the third jet originates from the same region of the nucleus as the dust jet, but the gas jet follows a different path after ejection.

The jets in Comet Halley were observed out to distances of 88,000 km, far outside of the collisional zone.[2] This posed an interesting question: What was the source of these gas jets? Because of adiabatic expansion, gas molecules released directly from the nucleus should appear completely isotropic at these distances. Because dust jets did not coincide with these gas jets, dust that is efficient at scattering optical wavelengths could not be the source. Instead, A'Hearn et al. (1986a,b) attribute these jets to an extended source of sub-micron "CHON" grains which are not apparent at visible wavelengths.

CHON particles, composed of the organic materials carbon, hydrogen, oxygen, and nitrogen, are compositionally different from silicon-bearing dust particles and, therefore, represent an important and distinct component of cometary solid grains. They were detected by mass spectrometers (aboard the Giotto and Vega spacecrafts) that directly sampled the coma of Comet Halley in March 1986 (Langevin et al. 1987, Kissel et al. 1986a,b, Jessberger and Kissel 1988, 1991). Recent laboratory experiments suggest that CHON grains may represent an interstellar component of cometary dust (Lien 1998). The large content of these organic grains was a surprise, and CHON grains have subsequently been invoked as contributing roughly half of both CN and CO gases observed in the coma of Comet Halley (A'Hearn et al. 1986, Eberhardt et al. 1987).

Two jets reported by Clairemidi and Moreels (1990) and Clairemidi et al. (1990, 1992) were detected in continuum (dust), OH, NH, CN, C_2, and C_3, spectro-images of Comet Halley. In contrast to the jets reported by A'Hearn et al. (1986a), the two jets identified by Clairemidi et al. have both a gas and dust jet counterpart. Spectro-images are images that are reconstructed from spectra taken across a grid of

[2]When the mean free path of a particle between collisions is equal to the distance between the particle and the nucleus, that particle has reached the edge of the collisional zone. This is the region in the coma where molecule-molecule collisions dominate population statistics.

locations in the coma. Each spectrum is translated into a brightness for that location [pixel] and an image results. If, like the CN and C_2 jets, the OH and NH jets are produced by sub-micron CHON grains, we should see OH and NH jets that are not spatially coincident with the dust jets. It is important to understand that the signal obtained at each gas bandpass contains contributions from both the gas and dust (continuum). An accurate continuum removal from the gaseous components is not a trivial task. Therefore, any traces of signal due to dust large enough to scatter optical wavelengths in the Clairemidi et al. gas data could have led to an erroneous report of jets created by the gas species. Thus, while gaseous jets with no dust jet counterpart have been reported for the CN, C_2, and C_3 species in Comet Halley, the same is not true for the OH and NH jets.

The opportunity to search for such OH jets presented itself recently. Older technology limited OH imaging capabilities. The availability of new blue-sensitive Charge-Coupled Device (CCD) detectors and new narrowband filters allowed for high signal-to-noise images of all gas species observed (OH, NH, CN, C_2, and C_3) in an unusually bright comet, Comet Hale-Bopp.

1.2.2 Comet Hale-Bopp

Comet Hale-Bopp is believed to be a somewhat evolved (not dynamically new), long period Oort cloud comet. During its passage through the inner solar system beginning in 1995, gravitational interactions with Jupiter acted to modify its orbital period from 4,210 years to 2,380 years. Comet Hale-Bopp has been classified as a long period, Oort cloud comet (Marsden 1997). It is chemically similar to a 'typical' Oort cloud comet when compared with the Lowell Observatory optical photometric database of >100 comets (Schleicher et al. 1997). Comets in the database fall into two main groups based on OH, NH, CN, C_2, and C_3 abundances: 'typical' and carbon-chain depleted. The latter are depleted in C_2 and C_3 with respect to OH, and

therefore with respect to water. So far, all Oort cloud comets and about half of the Kuiper Belt objects display 'typical' abundances.

Comet Hale-Bopp is the brightest comet observed in more than 20 years, no doubt due in part to its size. Size estimates of the nucleus range from 20 to 50 km as determined from OH production rates (Schleicher et al. 1997), Hubble Space Telescope (HST) imaging (Weaver and Lamy 1999), and thermal emission (Jorda et al. 1999). Observations have been obtained from the time of discovery, July, 1995 at 7.16 AU, to perihelion, 0.91 AU. Comet Hale-Bopp was still being followed as it receded from the Sun in January, 2000. At this time, it was beyond 10 AU (Pearce 2000). *This is the only comet that has been observed with CCD technology over such a large range of heliocentric distances.* This has allowed us to monitor its activity as it changed over a large range of heliocentric distances, 1 to 10 AU (e.g., Biver et al. 1997).

Digital processing of images has allowed for a detailed investigation of the coma morphology of Comet Hale-Bopp, unlike anything possible in previous comets. In addition, the advancement of Monte Carlo techniques used to model cometary comae (Combi 1987, Combi et al. 1988) has allowed a refined analysis and interpretation of the signals detected by these modern detectors.

Jets have been detected in Comet Hale-Bopp data in several species. Sunward dust and C_2 jets were reported by Clairemidi et al. (1997) and Rousselot et al. (1997). In addition, both Larson et al. (1997) and Mueller et al. (1997) have identified CN and dust jets and report that certain CN jets (in the anti-sunward direction) do not overlap spatially with any dust jets. Larson et al. suggest that the anti-sunward CN features support an extended coma source for the CN jets. If, as Larson et al. suggest, CHON particles are indeed the extended source of the CN in Comet Hale-Bopp, it is possible that OH and other gas jets are also produced by CHON grains.

Gas jets in OH, NH, CN, C_2, and C_3 in Comet Hale-Bopp are identified in this work and by Lederer et al. (1999). All species have 'sunward' jets as well as 'anti-sunward' jets without a spatially coincident dust counterpart. This assures that the jets in all these species are unquestionably due to the gas, and are not created by the underlying continuum. This is the first identification of OH and NH jets without an optical dust jet counterpart for any comet. In contrast with the Comet Halley spectro-imaging data (Clairemidi 1990a,b, 1992), the gas jets apparent in my Comet Hale-Bopp images are distinctly different from the morphology of the dust jets (e.g., gas jets are wider than the dust jets, show complete spirals, and have a more complex spatial structure). Comet Hale-Bopp's gas jets also do not spatially coincide with dust jets in some portions of the images. The underlying signal created by the dust in the NH and C_3 images is so high that exposure times short enough to prevent saturation in the CCD images (which is required to absolutely calibrate the images and allow the continuum to be subtracted from the images) resulted in low signal-to-noise ratios of the gas after the absolute calibration was completed. In this work, the analysis is focused on the OH, CN, and C_2 jets because the signal in the NH and C_3 jets is very weak.

1.2.3 OH as a Tracer of H_2O

Understanding the source of OH in comets is particularly important because OH measurements are used to infer the production rates of water. It is currently presumed that the primary, or in most cases, the sole source of OH is H_2O (see Section 4.5.2). H_2O is the dominant volatile component in comets and the major driver of cometary activity at heliocentric distances (r_h) < 3AU, but it is very difficult to observe directly from the ground due to atmospheric water absorption.

Because it is difficult to observe H_2O directly, and H_2O primarily dissociates into OH (Table 1-1), OH traditionally has served as the main indirect way to investigate a comet's water production. Observing OH in the UV has its advantages and

disadvantages. The underlying continuum (ie. the contribution from light scattered by dust at this wavelength and not due to the fluorescence of OH) at the 3090Å emission band of OH is relatively low because the Sun does not produce as much radiation at UV wavelengths. This means that an accurate continuum subtraction is more forgiving during the absolute calibration process. However, while this wavelength is observable from the ground, strong systematic variations due to atmospheric variability make this line difficult to well calibrate from the ground (see Chapter 2 for a complete discussion on atmospheric extinction problems associated with OH).

When water is the parent of OH, it is relatively simple to model and interpret. Branching ratios of water and lifetimes (τ) of H_2O and OH have been well studied both in the laboratory and astronomically, and are known more accurately than most other species in comets. Both branching ratios and lifetimes (Table 1-1) vary with the solar cycle (quiet vs. active Sun) and are subject to the Swings effect (the variation of solar flux that can be absorbed by cometary gases as a function of the comet's radial velocity and therefore the Doppler shift with respect to the Sun). The solar cycle and Swings effect each contribute a variation of 25% in the OH lifetime, which creates a total variation of 50%. The lifetime of OH during solar minimum (which applies to Comet Hale-Bopp at perihelion) is 1.4×10^5 s (Budzien, Festou, and Feldman 1994).

Table 1-1: Branching ratios of water.

Dissociation Species	Quiet Sun (%)	Active Sun(%)
$H_2O + \eta\nu \longrightarrow$	$\tau_{H_2O} = 7.94 \times 10^4 s$	$\tau_{H_2O} = 4.35 \times 10^4 s$
$H + OH\ (\chi^2\Pi)$	87.6%	85.3%
$H_2 + O^*$	4.9%	5.6%
$H + OH(A^2\Sigma^+)$	4.4%	5.2%
$H_2O^+, H + OH^+, H_2 + O^+, OH + H^+$	3.2%	3.9%

Note: Branching ratios of water for both the quiet and active Sun at 1 AU (Huebner 1990). Lifetimes are from Crovisier 1989.

If, however, an extended CHON source is a significant contributor of OH, then assuming all OH comes from water is an error, and the current methods for translating OH abundances to water abundances must be re-evaluated.

1.2.4 Jet Source: Gas or Grain?

Gas jets were, at one time, theorized to be improbable due to the rapid diffusion of molecules into space. Instead, a uniform spatial distribution was expected (A'Hearn et al. 1986a,b, Larson 1988). Due to adiabatic expansion, any gas molecules that came from a jet of molecular water were expected to become isotropic too quickly to allow gas jets to be discerned in images. Instead, the organic CHON particles discovered by the Giotto and Vega spacecraft were suggested as the source of the CN jets observed by A'Hearn et al. (1986a,b). Several mechanisms responsible for ejecting gases from CHON grains have been suggested by Crovisier (1999) including:

- Thermal dissociation (pyrolysis) from hot grains, which depends on the total absorbed solar flux;
- Photolysis of chemical species from UV radiation from the Sun; and
- Sputtering of OH directly from the grains following impacts of high energy solar particles, which depends on the solar wind flux at the comet's distance.

A hot grain that thermally dissociates releases radicals directly from its surface due to its high temperature (400 to 500 K). A slow speed thermal dissociation would aid in retaining the jet enhancement observed (Lamy and Perrin 1988). This was suggested as the mechanism responsible for the CO originating from grains in Comet Hale-Bopp by DiSanti et al. (1999). All three mechanisms were discussed as possibilities for Comet Halley's CN jets (Combi and Fink 1997, Lamy and Perrin 1988, Combi 1987). For thermal dissociation, CHON grains heat up as they move away from the nucleus, resulting in a production rate that increases with distance from the nucleus. But as molecules are released, the surface area of the grain decreases.

Eventually, the shrinking surface area begins to dominate, and the production rate then decreases as the grain moves even farther from the nucleus. The observed effect is a production rate that does not peak at the nucleus. This effect was observed in the CO production rate of Comet Halley (Eberhardt et al. 1987) and was described as a 'triangular source.'

The differences in the coma locations of the dust and gas jets were justified by velocity sorting. The smaller CHON grains were accelerated nearly to the speeds of the gas while the larger dust grains, which scatter optical wavelengths efficiently, were only accelerated to perhaps half the velocity of the gas (Gombosi et al. 1986). If a sub-micron grain source was responsible for the gas jets, the collimation would be retained because grains would follow a path dictated by their initial ejection direction and solar radiation pressure. The jets observed in Comet Halley were not located in the collisional zone. Thus, CHON grains were not coupled to the gas. Unlike the gas, adiabatic expansion does not play a significant role with solid grains, thus the range of velocities of the grains and the size of the active area on the nucleus responsible for the jet would dictate how diffuse the jet appears.

Instead of invoking CHON grains as a source of the radicals, Combi (1987) suggested that the collimation would remain intact through a spatially localized source of parents, but this theory could not explain the radial profile of the surface brightness for Comet Halley. The radial distribution indicated that the source of the CN jets actually peaked in production at a distance of 8,000 km (Klavetter and A'Hearn 1994) from the nucleus. Similarly, Comet Halley's CO jets displayed a peak production at 9,000 km (Eberhardt et al. 1987). This evidence supported the CHON grain extended source hypothesis. Klavetter and A'Hearn reported that 40 to 60% of the CN (depending on how many jets were present) originated in an extended source in Comet Halley's jets and not in its nucleus.

While the production rates of Comet Halley were too low to invoke collimation through collisions, it has been suggested that this mechanism could act to collimate jets in Comet Hale-Bopp because of its high production rate (10^{31} s^{-1}, Schleicher et al. 1997, Combi et al. 1997). However, the radial distribution of CO in Comet Hale-Bopp has been shown to require an extended source that peaked at a distance of 5,000 km from the nucleus when Comet Hale-Bopp was at 1.5 AU from the Sun; this supports an extended grain source (DiSanti et al. 1999). Di Santi reported that roughly half of the CO originated from an extended source.

1.3 Synopsis

In this dissertation, OH, CN, and C_2 jets in Comet Hale-Bopp are analyzed. The morphology, intensity variations, and radial profiles of the jets have been analyzed in an effort to constrain the source of the jets and the composition of the parent particles. In Chapter 2, the observations of Comet Hale-Bopp and data reduction techniques applied to the data are discussed. Chapter 3 describes the time-dependent, collisional Monte Carlo model developed here to recreate the observations in an effort to understand the source of the jets. In Chapter 4, the results and implications of this analysis are discussed. They indicate that an extended source in the coma must be invoked to explain the OH, CN and C_2 jets in this comet. Chapter 5 summarizes the conclusions and discusses future work in this area.

CHAPTER 2
OBSERVATIONS AND DATA REDUCTION

2.1 Facilities and Instrumentation

Data were obtained at Lowell Observatory with the 42″ (1.1 m) Hall Telescope and a CCD (charge-coupled device) camera (Table 2-2). The TI 800^2 (2x2 binned) CCD was employed on February 26, 1997. The 2048^2 CCD (also 2x2 binned) was available beginning March 1 and was used on March 1-6, and April 22, 23, 25, and 26, 1997. The 2048^2 CCD is more sensitive in the blue, allowing better quality OH observations. The scale of the resultant images is 0.72″/pixel for the TI chip and 1.14″/pixel for the 2048^2 CCD. A pulse counting photoelectric photometer was also used with the 31″ (0.8 m) telescope on February 26, March 5-7, April 13-14, and May 1, 1997.

With the impending approach of Comet Hale-Bopp, a new set of narrowband filters designed specifically for comets was funded by NASA. This new filter set was developed at Lowell Observatory during 1996 and was available for use in 1997 (Table 2-1). Each filter isolates either the light that fluoresces from a particular gas species including OH (3090 Å), CN (3870 Å), and C_2 (5141 Å), or the light scattered by dust continuum filters centered at 3448 Å, 4450 Å, 5260 Å, and 7128 Å.

The central wavelengths and bandwidths of this filter set were chosen to minimize the contamination in each filter from species other than the target species. However, certain gas species contaminate not only several continuum bands but also other gas filters (e.g., C_3 contaminates images taken with both the UV continuum and CN filters). In addition, an underlying contribution due to scattered light from the dust (the continuum) is responsible for a portion of the signal obtained in all gas

images. The gas contamination (when applicable) and underlying continuum (for the gases) are estimated for each filter and eliminated during the absolute calibration process (see Section 2.2.2 for a detailed explanation).

The February/March data include five photometric nights with supporting extinction star data, and at least 2 to 3 images per filter per night. March 2 and 4 were neither photometric nor spectroscopic, so no OH data were taken on those nights. April 26, 1997 was the only night during the April run that maintained photometric conditions long enough to allow us to obtain supporting extinction star data. However, April 22 and 23 were photometric while the comet was available, which allowed quality data to be taken with all filters. Again, 2 to 3 images per filter were taken per night in April. The OH data are most strongly affected by atmospheric extinction and therefore are the least forgiving of the species during questionable sky conditions (see below). As a result, OH data were taken on April 25, but the quality was too poor to analyze. Data taken with the photoelectric photometer on nights bracketing the April 22 and 23 observations were used in conjunction with the standard star data obtained on April 26 to absolutely calibrate the data on April 22 and 23. Because OH images include the least amount of continuum contamination, minor errors in the continuum subtraction that might result from using standard star data taken on other nights are less noticeable for the OH images than the CN or C_2 images.

2.2 Data Reduction

2.2.1 Initial Data Reduction

Each digital image taken must undergo a series of processing steps[1] to translate the total counts detected by the CCD at the telescope to a unit of measure that can be universally understood such as flux density (ergs/s/cm^2/Å) or production

[1]All the data reduction routines were developed here using IDL (Interactive Data Language).

Table 2-1: Narrowband filter characteristics.

Species	Central λ(Å)	$\Delta\lambda$(Å)
OH	3090	62
UV continuum	3448	84
CN	3870	62
Blue continuum	4450	67
C_2	5141	118
Green continuum	5260	56
Red continuum	7128	58

Note: The filters isolate either the continuum (the light scattered by dust) or emission lines from the gas.

Table 2-2: Comet Hale-Bopp observing details.

Dates	r_H(AU)	Δ(AU)	Phase Angle	PA_s	Species	Detector
Feb 26	1.090	1.53	40.3	151°	dust, OH, CN, C_2	CCD,Phot
Mar 1	1.062	1.48	42.0	154°	dust, OH, CN, C_2	CCD
Mar 2	1.054	1.47	42.5	155°	dust, CN, C_2	CCD
Mar 3	1.045	1.45	43.0	156°	dust, OH, CN, C_2	CCD
Mar 4	1.037	1.44	43.5	157°	dust, OH, CN, C_2	CCD
Mar 5	1.029	1.43	44.1	158°	dust, OH, CN, C_2	CCD,Phot
Mar 6	1.021	1.41	44.5	159°	dust, OH, CN, C_2	CCD,Phot
Mar 7	1.013	1.40	45.0	160°	dust, OH, CN, C_2	CCD,Phot
Apr 13	0.938	1.48	33.3	222°	dust, OH, CN, C_2	Phot
Apr 14	0.943	1.50	33.3	224°	dust, OH, CN, C_2	Phot
Apr 22	0.987	1.62	36.0	240°	dust, OH, CN, C_2	CCD
Apr 23	0.994	1.63	35.3	242°	dust, OH, CN, C_2	CCD
Apr 25	1.009	1.67	34.0	246°	dust, OH, CN, C_2	CCD
Apr 26	1.016	1.69	33.3	247°	dust, OH, CN, C_2	CCD
May 1	1.057	1.77	30.1	255°	dust, OH, CN, C_2	Phot

Note: Details include the dates the observations were taken, the heliocentric distance of the comet (r_H), the geocentric distance of the comet (Δ), the phase angle (Sun-comet-Earth angle), the position angle of the Sun (PA_s), the species that were observed, and the detector(s) used (CCD and/or photoelectric photometer). The plate scale is 1165 km/pixel, and 1390 km/pixel for March and April, respectively. The highlighted dates are those days that the gas images are modeled with Monte Carlo models.

rates (molecules emitted/s). The initial data reduction corrects for signal detected in the comet image that was not created by the comet (e.g., sky background created by moonlight, and the underlying bias) and accounts for signal that should have been detected but was lost between the comet and the detector (e.g., due to atmospheric extinction). The gas images must be processed further to eliminate the signal generated in that bandpass by the dust. The final absolutely calibrated image includes signal generated solely by the target species; the signal is then converted to units of flux density. A model (e.g., Haser model, Haser 1957) can then be applied to the resulting gas image to determine how much gas per unit time is being emitted by the comet. This is referred to as the total production rate quoted in molecules/s of the comet.

The images were bias subtracted, flat fielded, and sky subtracted. The CCD detector was cooled with liquid nitrogen which lowered the temperature to the point that the underlying dark current, the signal that is created by a warm detector, was negligible. Therefore, subtracting dark images from the comet images was unnecessary. A master bias image was created for each night typically using 10 bias frames. The bias level is the baseline signal that is inherent in each image because CCDs are electronic detectors. This should generate a uniform background noise level. Unfortunately, the 2048^2 CCD was initially wired improperly. This resulted in a 'striped' effect seen in not only the bias images, but also in low signal comet images. In an attempt to correct for this effect, discrete Fourier transforms were used to transform the data into frequency space, filter out the frequencies that represented the bias striping, and re-transform the data back. Unfortunately, discrete Fourier transforms do not deal well with the strongly peaked signal at the central condensation. The resultant images were too distorted to properly analyze the jets, especially near the nucleus. No satisfactory method was found to simultaneously eliminate the bias striping and retain the morphology of the comet without creating unacceptable artifacts

such as these. When possible, images that were not affected by these stripes (true for the high signal-to-noise images) were analyzed; no additional processing was applied to account for the bias problem. A set of master flat field images was created (one master flat image per filter) for each observing run to correct for pixel to pixel variations across the chip that are not created by the source (e.g., due to detector gain, optics, throughput, etc.). The variation across the chip from these effects is $\pm 15\%$. Each data image was normalized by the appropriate master flat image. A separate sky image was taken for each filter. A median value was extracted from these images and subtracted from the comet images. For those nights when no sky images were taken, a sky value extracted from standard star images was used because signal from the cometary coma fills the entire image for all comet images taken (i.e., a sky value cannot be extracted from the comet images). The star images were taken just before and after the comet images in a nearby part of the sky.

Each image was then corrected for atmospheric extinction and adjusted to a standard magnitude scale using images of standard stars of spectral type B taken throughout the course of the night. B type stars are chosen for the following reasons: they exhibit little (if any) variability; they have a strong UV flux; few spectral features are apparent; and one can access a range of stars displaying appropriate magnitudes for CCD detectors and photometers which are scattered across the sky to allow the observer to obtain standard stars at airmasses similar to those followed by the comet. A full list of standard stars following these criteria was calibrated specifically for the filter set used and was available at Lowell Observatory (Farnham et al. 2000). A 'standard star' is defined as any star used for calibrating the comet data to the standard magnitude scale. The standard stars were preferentially chosen in the same region of the sky as the comet.

Standard stars with more than one observation taken at a variety of airmasses are used to calculate the extinction coefficients (k) and are given the additional

designation of 'extinction star.' The extinction coefficients are computed by fitting a straight line through a plot of the DN (brightness) value of the extinction star (in magnitudes) vs. airmass, which yields magnitudes of extinction per airmass. Brightness values are extracted by applying an aperture to the 2-dimensional star images. The airmass was calculated via the standard cubic polynomial:

$$X = secZ - 0.0018167(secZ-1) - 0.002875(secZ-1)^2 - 0.0008083(secZ-1)^3 \quad (2\text{-}1)$$

where X is airmass and Z is the apparent zenith distance:

$$Z = Z_{true} - \frac{60.4tan(Z_{true}) - 0.0668tan^3(Z_{true})}{3600} exp(-h/8) \quad (2\text{-}2)$$

Z_{true} is the true zenith distance, calculated from the object's right ascension and declination and h is the elevation of the observing site in kilometers (Farnham et al. 2000).

In general, observations of each extinction star were taken at a range of airmasses bracketing those at which the comet was observed. When more than one extinction star was followed, an average of the extinction coefficients was calculated for each filter. The instrumental magnitude of the comet beneath the Earth's atmosphere, mI, was corrected for extinction to yield instrumental magnitude above the Earth's atmosphere, mI_o, by

$$mI_o = mI - k * X \quad (2\text{-}3)$$

A global solution for Δm, the zero point correction used to translate instrumental magnitude to the standard magnitude scale, was calculated using all standard star observations taken throughout the night (excluding those observations which were suspect in quality). The instrumental magnitude of the comet above the Earth's atmosphere was translated to the standard magnitude of the comet by:

$$m_o = mI_o + \Delta m \quad (2\text{-}4)$$

OH presents a particular set of problems when correcting for atmospheric extinction. Unlike the other gas species, in OH the extinction is produced by a combination of Rayleigh scattering (from molecules in the atmosphere), aerosols (e.g., dust in the atmosphere), and the ozone present in the stratosphere. The amount of extinction from both Rayleigh scattering (typically 40 to 50% of the total extinction) and aerosols (5 to 20% of the extinction; strongly site dependent) is dependent on the elevation one observes at, and can be represented by a linear relation of magnitudes of extinction/airmass as described above. The ozone in the Earth's atmosphere, on the other hand, lies at an altitude of 15 to 30 km above the Earth's surface, so the extinction due to ozone (40 to 50% on average) is not a function of the altitude of the observer. Furthermore, the amount of extinction due to ozone varies significantly and non-linearly with wavelength across the OH bandpass, and is very sensitive to the total ozone above the observer. A plot of extinction vs. airmass for OH is curved and thus one cannot use the method described above to correct OH images for atmospheric extinction. Instead, a 'local' airmass (X_{local}), which does change linearly with airmass, was employed. This local airmass is calculated by assuming the ozone lies in a slab parallel to the Earth's surface between the observer and the object and results in the local zenith angle Z_{local} related to X_{local} by:

$$X_{local} = sec(Z_{local}) = \frac{R + H}{((R + H)^2 - R^2 sin^2(Z_{true}))^{-1/2}} \tag{2-5}$$

where R is the radius of the Earth (6378 km) and H is the altitude of the slab (22 km).

The instrumental magnitude above the atmosphere for OH, mI_o, is computed via:

$$mI_o = mI - G_{R_{OH}} - E_{A_{OH}} X - G_{O_{OH}} \tag{2-6}$$

where $G_{R_{OH}}$ is the total extinction from the Rayleigh component, $E_{A_{OH}}X$ corrects for extinction due to aerosols, and $G_{O_{OH}}$ is the extinction due to ozone. Instrumental magnitude is translated to actual magnitude as described above (Eq. 2-4). For a complete description of how to calculate $G_{R_{OH}}$, $E_{A_{OH}}$ and $G_{O_{OH}}$ and more details on the absolute calibration process, see Farnham et al. (2000)

Comet Hale-Bopp, during the month both prior to (March) and following (April) perihelion, was available for a very limited time; approximately one hour at sunrise or sunset, respectively, and at high airmasses. Thus, while the comet was available, we obtained cometary data and observed standards prior to or following, respectively. On nights when conditions were photometric only during the short time that the comet was available, no extinction star data were taken with the CCD. On the nights when simultaneous photoelectric photometry was obtained, we relied on the extinction star observations taken with the photometer for the k coefficients (February 26 and March 6, and 7, 1997). It was possible to take both comet data and extinction star data using the photometer because it took a small fraction of the time to take photometry observations compared with the CCD images. All standard star observations taken with the CCD were used to calculate the Δm values. March 2 and 4, 1997 were non-photometric so absolute calibration was not possible for these nights.

Conditions deteriorated rapidly following the comet observations taken on April 22, 23, and 25, and no extinction star data were taken with the photometer. Therefore, extinction parameters from CCD images taken on April 26, 1997 and photometry obtained on April 13, 14 and May 1, 1997 were used to absolutely calibrate comet images taken on these nights. OH, which is the filter with the least amount of underlying continuum, fared well in this process. Both CN and C_2 have increasingly greater percentages of underlying continuum (see below), and the detailed morphology shows traces of residual continuum in the sunward direction in certain images.

The images were centered on the comet's photo-center and trimmed from 1024^2 pixels to 301^2 pixels. The final field of view of these images is $171''$ (176,000 km) per side for the March data and $285''$ (348,000 km) per side for the April data. In no case is there evidence that the gas jets extend beyond these trimmed fields of view. The images were also filtered to remove cosmic ray hits using the IDL routine sigma_filter.pro.

2.2.2 Absolute Calibration

After the images were calibrated to translate instrumental magnitude (m_o) into a standard magnitude scale, they were converted to linear units of flux, f:

$$f = 10^{-0.4m_o} \tag{2-7}$$

The flux generated in each filter by a V=0 magnitude star (F_{0xx}) is known *á priori* and is used to make the conversion to absolute flux density, F (ergs/s/cm^2/Å)

$$F = F_{0xx} f \tag{2-8}$$

where F_0 is the absolute flux of a 0 magnitude star in the xx filter, the same filter the comet image was taken with (either OH, CN, or C_2). F_{0xx} is given by:

$$F_{0xx} = F_{0v} \frac{f_{XX}}{f_{5556}} 10^{-0.4(m_{xx}-V)} \tag{2-9}$$

where $F_{0v} = 3.52 \times 10^9$erg/cm^2/sec/Å at 5556 Å; f_{XX}/f_{5556} is the ratio of the flux of the standard star in the xx filter with respect to the flux at 5556 Å; m_{xx} is the standard star's magnitude in the specified filter (xx); V is the standard star's magnitude in a Johnson V filter. F_{0xx} values are listed in Farnham et al. (2000).

Ideally, the only remaining signal in the gas images would have originated from the target gas species and the dust that reflects light within that bandpass. Continuum images should detect only light scattered by the dust. Theoretically, then, one could simply use the continuum images to estimate the amount of underlying

continuum in each gas image and subtract that to yield the signal emitted purely from the gas. The underlying continuum contributes approximately 10 to 20% (OH), 20 to 30% (CN), and 60 to 70% (C_2) of the total signal in these gas filters, respectively. However, special attention had to be given to several of the filters due to additional contaminations. An even distribution of continuum filters covering the frequency sampled by the gas species is essential to estimate the underlying continuum in the gas images. However, the wings of the C_2 and C_3 are very broad and made it impossible to cover frequency space evenly without a portion of these gases contaminating the continuum filters. The locations of the green and UV filters were chosen to minimize this contamination from the C_2 and C_3, respectively. At the same time, the continuum underlies the gas images. Thus, one must iterate to determine simultaneously the amount of the gas contamination in the dust images and the amount of underlying continuum in the gas images. C_3 also contaminates the CN filter.

After estimates of each gas contamination were computed and eliminated, the underlying continuum contribution was computed for each gas image and subtracted. Continuum images taken with filters whose wavelengths bracket the gas filters were used to interpolate the amount of underlying continuum in the gas images. Preference was given to employ the blue continuum filter for as many gases as possible since there is no underlying gas contamination in this filter, and the bandpass is closer in wavelength to the gas species compared with the red continuum filter.

The resulting continuum images contain signal purely from light scattered by the dust. Likewise, the gas images contain signal emitted purely from the from the gas.

The flux density can then be translated to production rates [molecules/s] for the gases and to the quantity $Af\rho$, a quantity used to a describe the relative amount of dust production. The former requires a model such as a Haser model. Details

on how to compute $Af\rho$ and a brief description of the Haser model can be found in Appendix 1, and A'Hearn (1983).

2.2.3 Image Processing and Enhancement Routines

Several techniques were applied to the data to enhance the jets and insure that they were not merely artifacts of the image processing techniques applied. The first, an unsharp mask, is designed to accentuate pixel to pixel brightness gradients. This emphasized the jets quite nicely, but the central portions of the resulting images were saturated because of rapid changes in brightness near the nucleus and therefore was not the main technique used to analyze the data. Details on unsharp mask routines can be found in Larson and Slaughter (1991).

The minimum azimuthal subtraction (MAS) technique solved the problems with saturation near the central condensation. In this technique, a radial profile is extracted from the data. This profile represents the minimum brightness values found within concentric annuli about the central condensation, each one pixel in width. The minimum for each annulus is an average of the dimmest 10% of the pixels. A polynomial is fit to the resultant profile to yield a smooth drop in signal with distance from the nucleus. The polynomial-fit radial profile is swept around in azimuth to create a 2-D template representing the minimum isotropic component of the cometary signal. This template is then subtracted from the data to yield an image representative of the non-isotropic component. A portion of the isotropic component is created by the jets, so this technique does not isolate the entire signal created by the jets; it is simply the non-isotropic component. Because the template is subtracted from the data as opposed to normalizing the data by template, this routine preserves the flux calibration (unlike images processed with the unsharp mask routine). Thus, these images are not restricted to purely qualitative analyses.

The asymmetric brightness in the sunward direction compared with the anti-sunward direction was emphasized using the MAS technique. This created a problem

for viewing the continuum images. Because the asymmetry is very dramatic in the continuum images, it was difficult to find a range of brightness values which simultaneously accentuated the morphology in the sunward and anti-sunward directions.

The wedge-subtraction technique is a modified version of the MAS technique. It accentuates the jets in all directions and simultaneously flattens the sunward/anti-sunward brightness asymmetry. It is similar to the azimuthal subtraction (MAS), but instead of using the azimuthally averaged radial profile where each value represented the average minimum value in an entire annulus, the radial profiles of 20° sections of each annulus were used to create each portion of the template. Radial lines can be seen in some of the processed data images (particularly CN, C_2, and dust) and are an artifact caused by the variation in solar insolation between the sunward and anti-sunward directions. The final template is comprised of all the individual wedges. This technique was used to enhance the jets but was not used for the quantitative analysis.

2.3 Projected Expansion Velocities

The observed expansion velocity of the jets in the processed images is the velocity at which the gas or dust expands away from the nucleus of the comet, projected onto the plane of the sky. The true expansion velocity can be derived from the projected expansion velocity, and is an important parameter for several reasons. First, models designed to calculate production rates rely on the expansion velocity as an input parameter. Second, Monte Carlo programs used to simulate the cometary coma, such as the one developed here, also require the expansion velocity as an input parameter. Third, the expansion velocity itself may yield clues regarding the physics and chemistry taking place in the coma. For example, collisions can act to heat the coma and accelerate the gas and entrained dust when faster moving hydrogen atoms collide with slower moving heavy particles, such as OH, and transfer part of their

kinetic energy to the heavy particles (see Section 3.2.3 for a detailed explanation); observed acceleration, then, suggests that collisions are an important mechanism at work in the coma. For the purposes of this work, note that significant accelerations are observed in Comet Hale-Bopp and are accounted for in the Monte Carlo model. The acceleration observed (on the order of 1 cm/s^2, comparable to the radiation pressure acceleration of 2 cm/s^2) increases the expansion velocity to at least 2 to 2.5 km/s by the time the gases reach roughly 100,000 km. In comparison, the typically adopted expansion velocity of the coma in most comets observed to date is 1 km/s at 1 AU. High production rates and the observed acceleration also indicate that collisions play a significant role in the coma of Comet Hale-Bopp and, therefore, were added to the models.

Jets can be used to determine the projected expansion velocity of the coma, as well as whether the gas and dust are accelerated in the coma. In this work, I have indirectly inferred the expansion velocity of the parents of the OH, CN, and C_2 jets by assuming that the mean outflow velocity of the parent will be the same as the mean outflow velocity of the jets. In practice, several methods were used to extract the projected expansion velocity of the parent. For the March data, a particular jet was followed by fitting a Gaussian profile to the peak of the jet through a temporal sequence of images taken over the course of nine days (Method A). Although the comet was only observable for a period of 1 to 1.5 hours on any given night, the combination of the Earth's rotational period and the comet's sidereal period ($\approx 0.4712 \pm 0.0002$ days, or 11.3 hours, Farnham et al. 1999) conspired in a favorable way. The comet rotated two full rotations plus roughly 40 minutes in 24 hours. Thus, one can observe the progression of the comet's morphology in 40 minute intervals from night to night. Hence, the March data sequence represents roughly one full cometary rotational period (Fig. 2-1). This method of following the shells as they propagate

through the coma was also used by Lisse et al. (1997) to estimate the expansion velocity of dust using thermal infrared images.

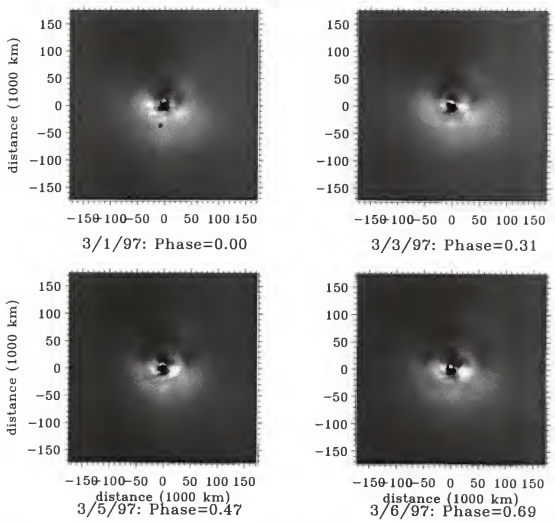

Figure 2-1: March time sequence. The images here demonstrate the evolution of Comet Hale-Bopp's jets with time. The images were taken between March 1 and March 6, 1997. The rotational phase is noted assuming the comet's sidereal period is 11.3 h and 0 phase begins with the image taken on March 1, 1997. The image on March 3, for example, demonstrates the morphology of the comet nearly one third of a rotation later (Phase=0.31).

Due to poor observing conditions in April, a similar temporal sequence was not available. April 26, 1997 was the only night in April when extinction stars were observed and an accurate continuum removal was possible. Instead, the best image taken in each filter on this night was used to estimate the projected expansion

velocity of each species. The simpler morphology aided in making this approach a viable option. The technique used is the same method used by Klavetter and A'Hearn (1992, Method B). I first unwrapped the (x,y) image into (ρ, θ) space where ρ is the projected distance from the nucleus. Then the jet was followed as it advanced with θ. Because its rotational period ($P_{rotation}$) is known, the relation between $\Delta\theta$ and dt is known:

$$dt = P_{rotation} \times \frac{\Delta\theta}{360^{\circ}} \tag{2-10}$$

The projected expansion velocity is computed by determining how far in ρ the jet moves over a given change in θ and therefore time (Fig. 4-33).

As a check, another method (Method C) was applied to the April images. It is similar to Method A applied to the March data, except that only one image is used as opposed to a temporal sequence. The jet closest to the central condensation in a given theta direction is presumed to become the next farthest jet one rotational period later and the third farthest jet after an additional rotation. A time sequence of thermal IR dust images taken by Lisse et al. (1997) in April, 1997 validates this assumption. The distance between the first and second, second and third, and first and third jets is then calculated. These distances are used in conjunction with the known rotational period of the comet to calculate the projected expansion velocity.

The analysis here suggests that projection effects must be taken into account to determine the actual expansion velocity; and the gas in the coma is accelerating. Maximum projected velocities of the gases range from 0.6 km/s to 1.0 km/s, depending on the direction (position angle) one looks, indicating projection effects must be accounted for. Velocity also clearly increases in a particular direction as the jet progresses from the nucleus which indicates that the coma is accelerating. These effects are both accounted for in the Monte Carlo models discussed in Chapter 3.

2.4 Summary

CCD images of Comet Hale-Bopp were obtained at Lowell Observatory using narrowband filters to isolate OH, CN, C_2, and dust. The images were fully calibrated to yield images representative purely of the species that each filter is designed to detect. The images were then processed using several techniques with the goal of enhancing the jets that are detectable at low levels in the original images. These jets can be used to determine the projected expansion velocities of the gases and dust in the coma. The techniques developed to calculate this velocity are described. In the following chapter, the models developed and used to analyze the coma are discussed further.

CHAPTER 3
MONTE CARLO MODELING

3.1 Introduction

Comparison of observations with models leads not only to a more accurate interpretation of the cometary images, but also allows one to extract information otherwise impossible to infer. For example, we can directly obtain column densities of gases from the data, but how can we extrapolate to give the total production rates of the comet as though we had an infinitely large aperture? We see jets in images, but how can we ascertain the source of the gas jets? Do they originate purely from more complex molecules, or do grains play a role in creating these jets? Can we extrapolate inward from the jets in the coma to determine where the active areas are located on the surface? Does it appear that the same active areas are responsible for all the gas jets, or do the individual areas appear to be inactive for certain species and active for others? Do all the active areas emit the same relative abundances of the gas species? What does this imply about the heterogeneity of the comet? All of these questions can only be answered after proper models are developed.

Astronomers have been creating mathematical models to understand cometary gas emission for more than a century (Bredikhin 1903). Cometary modeling advanced considerably with Haser's insight to analyze production rates (number of molecules emitted by the comet per second) in a cometary gas coma using Bessel functions (Haser 1957). The advent of computers and numerical modeling aided astronomers in taking another significant step forward: discretely simulating cometary comae. Since then, several types of models have been designed to recreate the coma of a comet including hydrodynamic models (Marconi and Mendis 1982a,b, Gombosi et al.

1985, Mendis et al. 1985), the vectorial model (Festou 1981a,b), and Monte Carlo models (Combi and Delsemme 1980, Combi and Smyth 1988, Combi, Bos and Smyth 1993). Each has its strengths and weaknesses, and one must choose which model to use based on the information one wants to extract.

3.1.1 Haser Model

Haser (1957) was one of the first to create a model that describes the gas particle density distribution of a cometary coma. It is one of the most basic coma models, but has stood the test of time. The Haser model presumes that parent gas molecules are ejected isotropically from the nucleus with a constant radial velocity and lifetime. The parent then decays into the observed daughter product, which also expands strictly radially away from the coma, in the same direction as the parent, with a constant velocity. The daughter then decays, according to its lifetime. In the process of photodissociation, the daughter radical will be given an additional ejection velocity and is ejected in a random direction; however, these effects are neglected in the Haser model. While it is understood that this is not physically realistic, the Haser model has been shown to yield reasonable estimates of gas production rates with very little computational effort and is therefore used regularly. Further details of this model can be found in Appendix 2.

3.1.2 Vectorial Model

A vectorial model is essentially a Haser model modified to include with one major improvement: the excess energy imparted to the daughter product is accounted for. The daughter molecule is given the freedom to move away from the parent in any direction, unlike the Haser model where the daughter necessarily moves radially away from the nucleus (Festou 1981a, b). In the vectorial model, one must integrate over each parameter included (e.g., velocity of the daughter [speed and direction] and

distance the molecule is from the nucleus) in the model, which becomes computationally intensive as additional parameters are added. According to Festou (1981), the vectorial model yields production rate estimates to within a factor of 20% when applied to optical data ($\sim 10^5$ km from the nucleus) and 60% for radio data ($\sim 10^6$ km from the nucleus) compared with the Haser model.

3.1.3 Hydrodynamic Models

For the collisional regime (the very innermost coma), hydrodynamic codes have traditionally been used to reproduce the behavior of the coma (Marconi and Mendis 1982a,b, Mendis et al. 1985, Gombosi et al. 1985). These models are based on the assumption that the gas and dust in the coma are completely coupled and acts as a compressible fluid. The models employ the equations of mass, momentum, energy conservation and the ideal-gas law:

$$\frac{\delta \rho}{\delta t} + (\mathbf{u} \cdot \Delta)\rho + \rho(\Delta \cdot \mathbf{u}) = 0 \tag{3-1}$$

$$\rho \frac{\delta \mathbf{u}}{\delta t} + \rho(\mathbf{u} \cdot \Delta)\mathbf{u} + \Delta p = -\mathbf{F}_{gd} \tag{3-2}$$

$$\frac{1}{\gamma - 1}\frac{\delta p}{\delta t} + \frac{1}{\gamma - 1}(\mathbf{u} \cdot \Delta)p + \frac{\gamma}{\gamma - 1}p(\Delta \cdot \mathbf{u}) = Q_{ext} - Q_{gd} \tag{3-3}$$

$$P = \frac{\rho k T}{m} \tag{3-4}$$

where t is time, ρ is the gas mass density, p is gas pressure, $\mathbf{u}$ is the gas velocity, $\mathbf{F}_{gd}$ is the gas to dust momentum transfer rate, γ is the gas specific heat ratio, Q_{gd} is the gas to dust energy transfer, and Q_{ext} is the external heating rate. This is the basic physics used to describe gas dynamic models. However, these models are computationally intensive, and can only describe the coma when the gas and dust particles are fully coupled, within the first few hundred or thousand kilometers from the nucleus. These models are only applicable to the inner few pixels of my comet images.

3.1.4 Monte Carlo Model

Monte Carlo models of a gas coma, like vectorial models, allow the isotropic ejection of the daughter molecule in the parent's frame of reference, but without having to integrate over each parameter. Instead, one computes the trajectories of a large number of individual particles,[1] typically on the order of 10^6, as they journey through the coma. A collection of particles is followed, and the locations of each surviving daughter radical are tabulated at the end of the simulation. The simulation is run for a long enough time to assure that quasi-steady state is achieved (see Section 3.2.2 for further explanation).[2] Additional parameters can be included, and one simply calculates the new trajectory of each individual particle accordingly.

3.2 Monte Carlo Models Developed for This Work

For a comet such as Comet Hale-Bopp, the jets are located at distances that are neither fully collisional where hydrodynamic codes are valid, nor completely collisionless where the number of parameters one must integrate over is more limited. Rather, the jets exist in a transition region between the two regimes, traditionally the most difficult to model. However, Monte Carlo techniques and faster computers have made this problem tractable with some effort. Several versions of Monte Carlo codes were developed here to investigate the source of the jets and coma (gas versus grain):

- A collisionless isotropic model;
- A modified version of this code that includes a first order effect of collisions;

[1] The word 'particle' is a generic reference to those particles that can either be gas or dust, depending on the specifications of the input parameters of the model; for example, the path of the particle might start out as the parent CHON particle and then continue as a gas molecule after it dissociates.

[2] A simulation that generates 10^6 to 10^8 particles requires anywhere from a few minutes to 30 minutes (depending on the input parameters) running on a Pentium III, 450 MHz computer.

- A collisionless jet model; and
- A jet model including first order collisions.

These are based on work by Combi and his collaborators (Combi and Delsemme 1980, Combi and Smyth 1988, Combi, Bos and Smyth 1993).

3.2.1 Gas Source Versus Grain Source

Gas jets were, at one time, theorized to be improbable due to the rapid diffusion of the daughter products from the parents (A'Hearn et al. 1986a). Collisions have been suggested as a mechanism that could inhibit the diffusion of daughter products, however, Comet Halley's production rates were low enough that collisions were too infrequent to maintain the observed collimation. If, however, the gases originated from CHON grains in the cometary coma, then one could expect to see the resultant collimated morphology because CHON grains do not expand adiabatically upon ejection. Alternatively, Combi (1987) suggested that a localized source of parents could result in the collimation. However, the radial profile could only be matched with jets originating from an extended source whose production of the observed radicals did not peak at the nucleus, but rather at a distance of $\sim 10^4$ km away from the nucleus (Klavetter and A'Hearn 1986). Therefore, CHON grains were invoked as the source of the CN jets in Comet Halley.

The size of the coma's collisional zone, R_{coll} is defined as the distance at which the mean free path of a particle is equal to the distance to the center of the comet's nucleus (Combi et al. 1997). This can be approximated by (Huebner 1990):

$$R_{coll} = \frac{Q_{gas}\sigma}{4\pi v} \tag{3-5}$$

where Q_{gas} is the total gas production rate, $\sigma = 3 \times 10^{-15}$ cm^2 is the collisional cross section, and v the typical outflow velocity. At 1 AU (Astronomical Unit), Comet Halley's total gas production rate was 7×10^{29} s^{-1}. If an average outflow velocity of 1.0 km/s is assumed, the collisional zone is 17,000 km, but Halley's jets were evident

to 88,000 km. In contrast, Comet Hale-Bopp's total gas production rate was near 10^{31} s^{-1} at 1 AU, 20 times higher than Comet Halley, with an outflow velocity of 2 to 2.5 km/s. Thus, Comet Hale-Bopp's collisional zone is roughly 240,000 km. The jets in Comet Hale-Bopp's coma are evident to roughly 125,000 km.

Because the jets are evident inside the collisional zone of Comet Hale-Bopp, it has been suggested that collisions could act to collimate the gases and therefore an extended CHON grain source is not necessary to produce the observed jet morphology. As a result, models were simulated with (1) a molecular gas source, (2) a CHON grain source, and (3) combinations of molecular gas + CHON grain sources. The molecular gas source is presumed to decay exponentially with time. The radial profile of the daughters created by this source is necessarily peaked at the nucleus where the strongest concentration of parent molecules exist. The CHON source is described by a triangular function whose production first linearly increases and then decreases with time such that the peak production occurs at some distance from the nucleus. A triangular source was found to successfully describe the CN and CO jets in Comet Halley by several authors (Eberhardt et al. 1987, Klavetter and A'Hearn 1994, Samarasinha et al. 1994). An extended source of CO that peaked away from the nucleus was also observed by DiSanti et al. (1999) for Comet Hale-Bopp. It is possible that this extended source observed in Comet Hale-Bopp could also be responsible for the CN, C_2, and OH jets.

3.2.2 Non-collisional Isotropic Model

Version (1) of the Monte Carlo model is based on the very basic isotropic, non-collisional Monte Carlo model described by Combi (1980). A collection of particles is ejected from a point source and followed until the end of the simulation. The basic parameters in this model include:

(a) the source of the observed radical: *gas* or *CHON*

(b) the lifetime of the parent (nuclear) gas source OR the time it takes

for production from a parent grain (extended) source to peak: τ_p

(c) the lifetime of the observed daughter radical: τ_d

(d) the radial velocity of the parent: v_p. Xie and Mumma (1996) demonstrated that the tangential velocity, V_{tan} was much smaller than V_r, and therefore, only radial velocity is accounted for.

(e) the radial velocity of the daughter: v_d

(f) acceleration due to radiation pressure: a_{rp}

(g) the total integration time: t_F

(h) the total number of parent particles ejected: N_t

The lifetimes and velocities tested were based on published values (Table 3-1). Best fit parameters are discussed in Section 4.3 and are listed in Tables 4-1, 4-2, and 4-5. and are discussed in Chapter 4. The choices of input parameter values are based on a combination of theory and astronomical observations. Parent and daughter lifetimes and velocities are determined by comparing model results (based initially on theory) with observations of comets. The parent lifetime of CHON grains is based on theoretical calculations using laboratory produced material that may reflect the properties of organic grains in comets. The initial parent velocity is based on results of hydrodynamic models, and the choice of α (see Section 4.3.2) based on results from comparing Monte Carlo models to OH radio data (Lovell 1999). Acceleration due to radiation pressure is given by Combi (1980) and results in a good fit to the data. The choice of pole position is based on the comparison of Monte Carlo models with jets observed in Comet Hale-Bopp (see Section 4.3.7 for references). The total integration time, t_F, is long enough to assure that steady state is reached (see below). The total number of radicals generated throughout the simulation was chosen to yield a signal-to-noise comparable to the images (10^6 to 10^7 parent particles).

The lifetimes in Monte Carlo models will be either longer than or equal to those used in Haser models, which assume only radial motion. This can be understood

Table 3-1: Monte Carlo model parameter space.

Parameter	Range
τ_{CHON} (sec)[a]	0.50 to 6.0×10^4
τ_p(OH) (sec)[b]	4.0 to 10.0×10^4
τ_p(C_2) (sec)[c]	2.0 to 4.0×10^4
τ_p(CN) (sec)[d]	2.0 to 3.0×10^4
τ_d(OH) (sec)[b]	1.0 to 2.0×10^5
τ_d(C_2) (sec)[c]	0.50 to 1.9×10^5
τ_d(CN) (sec)[d]	2.0 to 4.5×10^5
v_p (km/s)[e]	0.1 to 1.0
dv_o (km/s)	0.0 to 1.0
α^e	0.0 to 1.0
v_d (km/s)[f]	0.1 to 2.0
$(\alpha_p, \delta_p)^g$	(240 to 290,-40 to -70)

Note: Input parameters were tested over the ranges listed. Ranges are based on values found in the literature when possible or based on values that were reasonable. The ranges listed account for error bars in estimated values.

[a]DiSanti et al. 1999, Klavetter and A'Hearn 1994, Lamy and Perrin 1988.

[b]Budzien, Festou, and Feldman 1994, Combi, Bos and Smyth 1993, Cochran and Schleicher 1993.

[c]Ellis and Neff 1992, Schulz et al. 1993, Combi and Fink 1997 and references therein.

[d]Schulz et al. 1993, Samarasinha 1992, Klavetter and A'Hearn 1994, Krasnopolosky 1991.

[e] Lovell 1999.

[f] Combi, Bos and Smyth 1993, Klavetter and A'Hearn 1994, Ellis and Neff 1992.

[g] Vasundhara and Chakraborty 1999.

more easily through a description of scalelengths (scalelength = lifetime * velocity) which can be used in lieu of lifetimes when the velocity outflow is constant (an implicit assumption of Haser models). When daughter products are ejected isotropically from the parent, they are given a tangential component to their motion (with respect the parent's radial motion) as well as a radial component. Thus the actual scalelength, which is the vectorial sum of both the tangential and radial scalelengths, will be longer than the Haser (radial only) scalelength if the daughter ejection velocity is not negligible compared to the parent.

A parent molecule is created at time, t_p, and is ejected in a random direction (θ_p, ϕ_p). Parents are emitted preferentially sunward according to Lambert's law (Wallace and Miller 1958):

$$n = \frac{1}{2} n_o (1 + cos\theta) \tag{3-6}$$

where n is the number of parents ejected in the θ direction, n_o is the number of parents ejected in the $\theta = 0$ direction, and $\theta = \theta_p$ is the angle from sunward. After a certain time, t_d, the parent decays into the daughter through a distribution representative of an exponential decay (photodissociation of the parent gas) or a triangular distribution (production from a parent grain). The daughter is emitted isotropically in the parent's frame of reference. At t_{gd}, described by an exponential decay, the observed radical decays into a granddaughter product.

The trajectories of the parent and daughter are calculated and vectorially added together to give the final location of the particle at time t_F. The particle is only tabulated if it is a daughter radical at t_F, the final (end) time of the simulation. The model must be integrated over a timeframe sufficient to achieve quasi-steady state, $t_F \approx 5 \times (\tau_p + \tau_d)$. After $t = 5 \times (\tau_p + \tau_d)$, over 99% of the parents ejected at $t = 0$ have dissociated so that at any time in the future one's results are, on average, the same. The total integration time chosen is 5× greater than the maximum $(\tau_p + \tau_d)$ tested

for CN. This combination gives the largest possible value for t_F. For consistency, the same t_F is used for all species.

Using Monte Carlo techniques, random numbers (R_i = random number) are generated. The random number generator used here was taken from numerical recipes called the L'Ecuyer routine (Press et al. 1992). It includes a Bays-Durham shuffle and added safeguards. This routine returns a uniform random deviate between 0.0 and 1.0 (exclusive of the endpoint values) and is non-repeating for the first 2×10^{18} particles generated. The computer's clock time was used to seed the code. The random numbers are used to compute the following:

- The time the parent is ejected from the nucleus: $t_p = t_F R_i$;
- The direction the parent is ejected: $\phi_p = 2\pi R_i$, $cos\theta_p = 1 - 2R_i$;
- The time the parent dissociates into the observed daughter:

  $t_d = t_p - \tau_p ln(R_i)$ for a molecular source. OR

  For the extended source (CHON grains), a triangular function was used which increases and decreases linearly with time according to:

  $t_d = t_p + \tau_p (R_i)^{1/2}$ from $t = 0$ to t_{Peak} and

  $t_d = t_p + \tau_p (2 - (R_i)^{1/2})$ from t_{Peak} to $2t_{Peak}$;
- The direction the daughter is emitted: $\phi_d = 2\pi R_i$, $cos\theta_d = 1 - 2R_i$; and
- The time the daughter (observed radical) dissociates into the granddaughter: $t_{gd} = t_d - \tau_d \ ln(R_i)$.

3.2.3 Collisions

As mentioned earlier, with Comet Hale-Bopp's production rates peaking at 10^{31} molecules per second near perihelion, collisions clearly played an important role in the coma. The production rates in Comet Hale-Bopp were high enough to suggest that heating due to collisions (see below) is responsible for the acceleration observed in the coma out to distances of at least 100,000 km from the nucleus.

The timescale between collisions is

$$\tau_{coll} = \frac{1}{n\sigma v_{th}} \tag{3-7}$$

where n is the density of the coma, $\sigma = 3 \times 10^{-15}$ cm^2 is the hard-sphere collisional cross section and $v_{th} \approx 0.1$ km/s is the thermal speed of neutral species. Near the nucleus, collisions occur at a rate of 100 s^{-1} for a Comet like Halley, but for Comet Hale-Bopp, whose total production rate is 20 times higher, the rate is 2000 s^{-1}. At 10,000 km, assuming the speed has risen to 1 km/s due to adiabatic expansion, the rate of collisions for Comet Hale-Bopp drops to 0.003 s^{-1}.

The majority of the energy that results from the photodissociation of water is imparted to the daughter molecules as translational energy (Festou 1981b). The kinetic energy of the molecule is the energy that can be transferred in a collision. The mechanical energy transfer per collision is given by

$$\Delta E = \frac{1}{2} m(\Delta v)^2 \tag{3-8}$$

where m is the mass of the radical and Δv is the change in velocity due to the collision. For a collision with a water molecule near the nucleus moving at 0.1 km/s, this is approximately 10^{-22} J, which is less than 10^{-3} eV. When water dissociates into H + OH, conservation of energy and momentum dictates that the H atoms are released with typical velocities of 20 to 30 km/s, while OH is ejected with a velocity of 1.05 km/s. When OH dissociates, the H atoms are released typically with speeds near 8 km/s (Combi and Smyth 1988). Thus, while H atoms are lighter, their speeds are higher, and a collision with one of the faster H atoms involves an energy exchange of 2.6 eV. However, due to their small mass (compared with the heavier radicals, e.g., water and OH) only 10% of their kinetic energy is transfered in each collision, requiring 20 to 50 collisions to completely thermalize (Combi 1987, Combi and Smyth 1988).

An additional component of H atoms with typical speeds of 4 km/s has also been observed. This observation is theorized to be a consequence of the thermalization of hydrogen atoms through collisions with heavier molecules in the collisional zone (Kitamura, Ashihara and Yamamota 1985). The exchange of energy during collisions and subsequent thermalization of the hot H atoms acts to accelerate the gas in the coma. For a comet with high production rates like Comet Hale-Bopp, the density and therefore rate of collisions and energy exchange continues for greater distances.

To investigate the effects of collisions, collisional models were produced to compare with the collisionless models and with the data. The following effects were included in the collisional Monte Carlo code: an acceleration representative of heating due to collisions; and collisional re-direction, where a new direction is generated at the time of the collision (θ_d, ϕ_d). The code calculates both the distance the molecule travels and the time elapsed between collisions.

The additional parameters added to the collisional versions of the models include:

(i) the acceleration parameter due to collisions: α
(assuming the basic power law described by Lovell (1999), Eq. 3-9)

(j) a range of the initial velocity distribution (in addition to v_p): $dv_o = \pm 50\%$

(k) the collision cross sectional area between the radical observed and the background coma gas: σ

(l) the gas production rate in the coma: $Q = 10^{31}$ at 1 AU.

The acceleration parameter and initial velocity, α and V_o, are correlated; the effects of increasing one can be compensated by decreasing the other, resulting in a family of solutions. Initial guesses of this combination were taken from Lovell (1999). The amoeba.pro routine was used to fine-tune the values chosen. The amoeba routine performs a multidimensional minimization of the function evaluated, in this case the

radial brightness profile. It is based on the downhill simplex method of Nelder and Mead (Press et al., 1999 and references therein) and is included in IDL's general library of functions.

A range of initial velocities dv_o was incorporated and affects the width of the jets. The range of $dv_o(\pm 50\%)$ was chosen to match the widths of the jets observed in Comet Hale-Bopp. Gas production rates of Comet-Hale Bopp were generated with the Haser model (e.g., Schleicher et al. 1997).

The simple power law employed by Lovell (1999) is used to account for the acceleration due to collisional heating within the collisional zone:

$$V_{exp} = V_o \left(\frac{rr}{r_{nucleus}} \right)^{\alpha} \tag{3-9}$$

where V_{exp} is the radial outflow velocity, V_o the initial velocity, $r_{nucleus}$ is the size of the nucleus, and α is the exponent. This is not a rigorous solution, but such a function was found necessary to fit Lovell's radio observations of the OH radial velocity. Incorporating acceleration with this representation also allowed me to recreate the jets at the right locations in my Monte Carlo models, and thus is consistent with my data as well.

The total radial distance a radical moves, rr, in time t is found by integrating Equation 3-9 from 0 to t:

$$rr = \left(\frac{r_{nucleus} + V_o t(1-\alpha)}{r_{nucleus}^{\alpha}} \right)^{1/(1-\alpha)} \tag{3-10}$$

Once the radical is beyond the collisional zone, collisional heating no longer acts to accelerate it. Therefore, at distances beyond the collisional zone, the radical is given a constant velocity with a value equal to the velocity it acquired before crossing into the non-collisional regime (roughly 2 km/s).

The tangential velocity was demonstrated to be small compared to the radial velocity by Xie and Mumma (1996). Thus, the parent particles, whether molecules

or CHON grains, are emitted by the nucleus and move strictly radially away from the nucleus; therefore, the direction of motion does not change for parents. Daughter products do collide with other particles, and at each collision, their direction of motion changes (i.e., collisional redirection). When the daughter is produced (or scattered), the local value of the number density is used to determine its collisional pathlength. The collisional pathlength, l, is the distance the radical will travel before it collides with another molecule. Collisions for an individual radical continue until t_F is reached. The time elapsed between each collision is calculated and added to the total time elapsed, t_{total}. Each path the daughter takes from inception to collision (and to any subsequent collisions) is added vectorially to give the final daughter position at t_F.

The collisional pathlength is related to the number density through:

$$N(r(l')) = \frac{Q}{4\pi v}\frac{1}{(r(l'))^2} \tag{3-11}$$

where $r(l') = (r_o^2 + l'^2 + 2r_o l' cos\theta)^{1/2}$ is the distance from the nucleus and l' is a point along this path. Using Monte Carlo techniques, one can relate the number density to a random number, R_i through

$$-ln(R_i) = \sigma \int N[r(l')]dl' \tag{3-12}$$

This becomes

$$-ln(R_i) = \frac{\sigma Q}{4\pi}\int_0^1 \frac{[1 - 2\beta(l' + r_o cos\theta)/r(l') + \beta^2]^{1/2}}{v(r(l'))^2} dl' \tag{3-13}$$

where $\beta = v/v_l$, the ratio of the outflow speed of the coma to the particle speed.

The above integral can be used to find the Monte Carlo collisional pathlength. If one assumes that (a) the outflow velocity is constant and (b) the thermal speeds of the molecules can be neglected ($\beta = 0$), the integral defining the collisional pathlength can be solved analytically. A first order approximation of the collisional pathlength results. However, (a) is only valid for a non-collisional coma which does

not accelerate, and (b) is a valid approximation for the fast H atoms that are moving much faster than the surrounding coma; (b) is not valid for heavy molecules such as OH, CN, and C_2.

Combi and Smyth (1988) improve upon Kitamura, Ashihara, and Yamamoto's approximation by modifying it to allow for a particle's variable speed with distance from the nucleus. They note that speed changes slowly compared with any reasonable collision lengths, therefore, one can assume that a simple inverse-square law referenced to the local value of the density can be used. The resultant form for the collisional pathlength, l, is based on the equation:

$$l = r_o \left[sin\theta tan \left(\frac{\pi}{2} - \theta - \frac{sin\theta ln(1 - R_i)}{r_o \sigma N(r_o)} \right) - cos\theta \right] \tag{3-14}$$

where

r_o = the radial location of the molecule at the beginning of its journey,

θ = the angle the molecule is moving with respect to the outward radial vector,

R_i = a random number,

σ = collisional cross section between the observed radical and the coma gas,

$N(r_o) = Q/(4\pi V_{exp} r_o^2)$ the number density of scatterers at r_o,

Q = gas production rate of the coma.

The scatterers are assumed to be either water or OH molecules, and the cross section used is an average of the cross sections of these two molecules (Table 3-2). The cross section for H_2-OH or CO-OH scattering is the same as that for OH-OH collisions, so the scattering holds for OH scattering from any of these molecules. Collisions between water molecules and OH dominate out to roughly half of the collisional zone radius (Combi, Bos and Smyth 1993). Half the collisional zone is roughly 120,000 km for Comet Hale-Bopp, which is where the jets are located (see

Section 3.2.1). The images shown here are 176,000 km per side for the March data and 348,000 km per side for the April data.

Table 3-2: Collisional cross sections.

Observed Radical - Coma gas	Cross section [cm^2]
OH - H_2O	3.2×10^{-15}
OH - OH	3.0×10^{-15}
OH - H_2	3.0×10^{-15}
OH - CO	3.0×10^{-15}
CN - H_2O^*	1.0×10^{-15}
C_2 - H_2O^*	1.0×10^{-15}

Note: Cross sectional areas of collisions between coma gas and the observed radical. (Combi et al. 1996, *Combi 1985)

This portion of the code is based on the work of Combi and Smyth (1988), and a full derivation can be found there.

Equation 3-14 is an good approximation for fast moving H molecules, but not for the much slower moving OH, CN, and C_2 molecules where the outflow velocity of the coma is likely to be comparable to the speeds of the observed radicals. Combi, Bos, and Smyth (1993) further refined the above approximation to account for collisions between heavy molecules. The integral equation that approximates collisions between heavy gas molecules is:

$$-ln(1-R_i) = \frac{Q\sigma}{4\pi c_o r_o \gamma} \times \int \frac{v_{\lambda'}[erf(v_{\lambda'})(1+1/2v_{\lambda'}^2) + exp(-v_{\lambda'}^2)/\pi^{1/2}v_{\lambda'}]}{(1+2\lambda' cos\theta' + \lambda'^2)} d\lambda' \quad (3\text{-}15)$$

where

$$v_{\lambda'} = \gamma \left[1 - 2\beta \frac{\lambda' + cos\theta}{(1+2\lambda' cos\theta' + \lambda'^2)^{1/2}}\right]^{1/2} \quad (3\text{-}16)$$

and

Q = Coma gas production rate,

σ = the collision cross sectional area for collisions between the observed radical

and the coma gas,

c_o = coma outflow speed (assumed to be the same as the radical's speed),

r_o = initial radial distance from the nucleus,

$\gamma = u\alpha^{1/2}$,

$\alpha = m/2kT$ assuming a coma predominantly of water,

$T = 103 r_{heliocentric}^{-1.10}$ (Lovell 1999)

$\lambda' = l'/r_o$ = the collisional pathlength normalized to r_o,

θ = direction of motion for the observed radical with respect to radially outward from the coma,

$\beta = c_o/u$,

$u = V_{exp}$ = speed of the observed radical.

However, unlike the approximation for fast moving H molecules, this integral cannot be solved analytically and inverted to yield an expression for the collisional pathlength. Instead, Combi, Bos and Smyth have developed a method to approximate this integral. They note that the numerator in the integral varies only weakly along an individual pathlength for one collision. One can assume that the numerator is a constant equivalent to the value at $\lambda = 0$, which describes the conditions at r_o. The remaining integral is then equivalent to Equation 3-14 above, which can be solved analytically and results in a first-order approximation for collisions between heavy molecules. One then replaces the initial guess with half the distance of the predicted first-order approximation and recalculates the collisional pathlength.

3.2.4 Collisional Jet Models

Collisions play a role in collimating the jets. The modeled jets in the collisionless model were different from the collisional model, which were also a much better fit to the observations (Fig. 3-1). Given the emphasis on studying the jets, and the

likelihood that collisions play a dominant role in this comet, the collisional jet model was adopted.

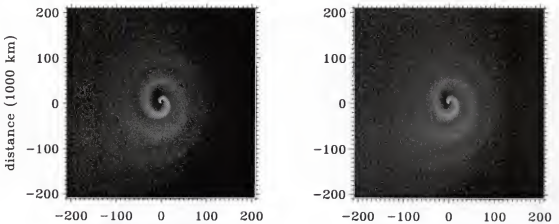

Figure 3-1: Monte Carlo model: Collisional and non-collisional models. This demonstrates the difference between the collisional and collisionless model. The collisions act to collimate the jets; the effect is strongest near the nucleus where the collisions occur the most frequently.

The following additional free parameters are required for the jet model that generates jets, and therefore must be time dependent. This includes not only the parameters outlined in the isotropic model (parameters a-c,e-l above), but also the following:

(m) total number of parent particles ejected in one time step: $N_{particles}$

(n) timestep: dt

(o) rotational period of the comet's nucleus: $P_r = 11.3$ h

(p) orientation of the north pole of the nucleus: $lat_{pole}, long_{pole}$

(q) position angle of the Sun projected onto the plane of the sky: PA_{Sun}

(r) the Sun-Comet-Earth phase angle: *phase*

(s) total number of jets: N_{jets}

(t) location of each jet on the comet, assuming a spherical nucleus: $lat_j, long_j$

(u) opening angle of each jet: *width*

(v) strength of each jet: S_j (to allow variable contributions from jet to jet)

The program is run for a total time of t_F, broken into Nt timesteps where each timestep is dt seconds long. The total number of timesteps is $Nt = t_f/dt$. The comet rotates $d\phi$ degrees per timestep, dt, where $d\phi = dt\ 360°/P_r$. $N_{particles}$ and dt were chosen to generate an image with a signal-to-noise comparable to the observed image. The rotational period of Comet Hale-Bopp is well known ($\approx 0.4712 \pm 0.0002$ days, or 11.3 hours, Farnham 1999). The orientation of the north pole is approximately the location given by Vasundhara and Chakraborty (1999) (hereafter VC), modified to best fit the jet morphology in my images. Pole locations fit by VC, Samarasinha (1998), and Licandro et al. (1997), and references therein were also tested for this parameter but did not fit as well as the VC estimate. The position angle of the Sun projected onto the plane of the sky and the phase angle are known from ephemerides.

The jet parameters (lat_j, $long_j$, $width$, S_j) are the least well constrained of all the parameters. The locations of jets reported by VC were used as first guesses. No reliable automatic method of testing these parameters was found. Instead, approximate fits by eye were used as initial guesses for (Δlat, $\Delta long$, $\Delta width$, ΔS_j). All the 'good' fits to the morphology improved the radial profiles fits, which are easier to see and quantify. Hence, every refinement to the model made to fit the morphology was checked to see if it produced a better radial profile fit. The amoeba.pro routine in IDL (see Section 3.2.3) was applied to the radial profiles to quantitatively determine the best fit (see Table 3-1 for the parameter range and Tables 4-1, 4-2, and 4-5 for best fit parameters).

The jet locations themselves are defined in cometocentric coordinates (comet-centered). When generating a jet, the individual particles are given a direction (θ, ϕ) with respect to radially outward (where radially outward is centered on the jet). An individual particle's cometocentric coordinates are then calculated. This is then translated to heliocentric coordinates to determine solar insolation. The position of

the Sun with respect to the comet's north pole is used to translate from cometocentric to heliocentric coordinates. Finally, the particle's coordinates are translated to geocentric coordinates, as we would see projected onto the plane of the sky. Details of the coordinate transformations can be found in Smart (1977), VC99, and Rhode and Sinclair (1992).

To compare the model output to the data, an image of a molecular gas isotropic source was added to the jet image. The effects of collisions and acceleration were also included in the isotropic source. The relative contribution from the CHON source and the nuclear gas source were varied until the resultant radial profile of the model fit the data (Fig. 3-2). This image was then convolved with the point spread function from that evening's observations to better represent the effects of the instrument and the atmosphere. Finally, an image representing random noise was added to simulate the effects of the system noise. The resultant model images were then processed in the same manner as the data.

3.3 Summary

Both a Haser model and Monte Carlo models are employed to analyze aspects of the physics and chemistry that are responsible for the gas coma (including both the diffuse and jet components). The Monte Carlo model was fully developed here and was based largely on a number of Monte Carlo models discussed in the literature. The Monte Carlo models describe a second generation gas with radiation pressure acceleration and an isotropically ejected daughter. Jet models include a time-dependent model with a rotating nucleus that has several active areas producing jets. Daughter radicals undergo collisional redirection and acceleration in the collisional zone where the jets are most evident.

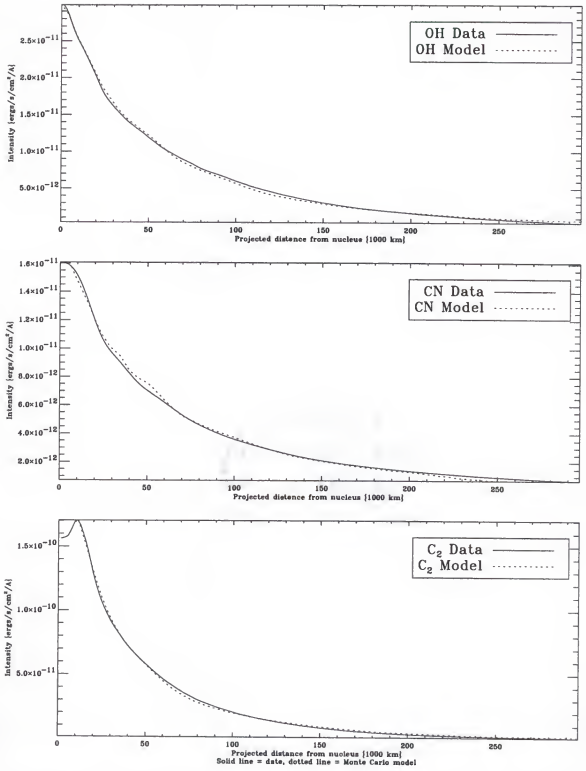

Figure 3-2: Radial profiles of data and best-fit models (April 26, 1997). April 26, 1997: Radial profiles of the data (solid line) and the Monte Carlo model that best fits the data (dotted line) for OH, CN and C_2. Random errors associated with the Monte Carlo process are smaller than the thickness of the line.

While the code at its final stage is certainly more complex than was anticipated, limitations and approximations dictate that the code is not a true representation of reality in every sense (as is true for any model). Modifying the code to include a non-spherical nucleus, a particle size distribution for the extended source, grain fragmentation, and modeling differences between a pure CHON source and CHON mantled grain with a refractory core are examples of how this code might be improved. However, the main science-driving questions can be answered without these improvements.

Chapter 4 discusses the effect each parameter has on the simulated comet images. It also includes the analysis of the model as it applies to the data and the results.

CHAPTER 4
ANALYSIS AND DISCUSSION

4.1 Introduction

Comet Hale-Bopp's jets can be used to address many questions regarding the properties of the coma: Is the source of the gas jets a nuclear gas source or an extended grain source? How many discrete active areas on the nucleus are responsible for the observed jets, and where are they located? Does the nucleus isotropically emit gas and/or dust in addition to the active areas; if so, how much material do the discrete areas eject compared with a diffuse, isotropic source? Can the composition of the proposed parent(s) of each source be constrained? Why does the morphology of the jets vary from one gas species to the next? In this chapter, both the results from this study and how they apply to these questions are discussed. In fact, all of these questions are partially or wholly addressed by my results.

The answers to these questions contribute to the understanding of both the chemical properties of the comet as well as the physical processes necessary to produce jets. If an extended source in the coma is responsible for creating the gas jets, it is essential to characterize that source before one can determine the composition of the gases that are evaporating directly from the nucleus and the dust that is entrained in the gas. The composition and the homo/heterogeneity of a comet will yield insight into how it formed, as well as the conditions present where it formed in the solar nebula. Thereby, this information will lead to a better understanding not only of comets, but also of the conditions present during the formation of the solar system.

4.2 Data Analysis

In this section, the methods used to identify OH, CN, and C_2 gas jets in Comet Hale-Bopp are discussed. Similarities and differences in the morphology and widths of the gas jets are examined. The evolution of these jets is described as well as how the changes in morphology aided astronomers in extracting valuable information about this comet, including the rotational period and the orientation of the comet's north pole -- two parameters that are critical input parameters for my coma models.

4.2.1 Jet Identification

Dust and gas jets (OH, CN, C_2) in Comet Hale-Bopp were identified here (Lederer et al. 1997, Figs. 4-1, 4-2). This is the first identification of OH jets without coincident dust jets for any comet. OH is particularly important since it is used as a tracer of water, the comet's most abundant component and the main driver of cometary activity within 3 AU of the the Sun. In all cases, the apparent extent of the jet activity is within $\sim 130,000$ km or $125''$ of the central condensation in the March data, and within $\sim 125,000$ km or $100''$ in the April data. This is consistent with the extent of the CN jets reported in Comet Halley, which were evident to at least 88,000 km (A'Hearn et al. 1986a, b).

The morphology of the gas jets can be discerned in the raw images, but is faint. To increase the contrast of the jets, several image processing routines were applied including an unsharp mask and several versions utilizing azimuthally-averaged subtraction (see Section 2.2.3). To insure that the features were real and not artifacts of the processing, each enhancement technique was applied to the images and compared the results (Figs. 4-3, 4-4, 4-5, 4-6). The general morphology of the jets is consistent with each technique, which lends confidence to the identification of the jets. The MAS (Minimum Azimuthal Subtraction) technique retains the sunward /

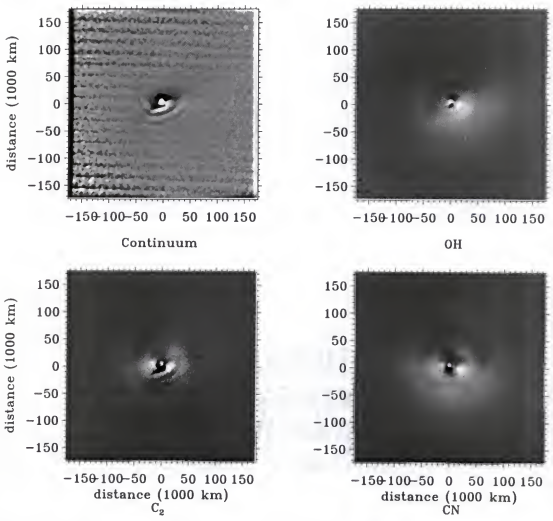

Figure 4-1: OH, CN, and C_2 data (March 6, 1997). Images were taken in continuum (dust), OH, CN, and C_2 narrowband filters. The continuum image here is processed with an unsharp mask while the other images are processed with the MAS technique. The sunward morphology in C_2 that resembles the dust may be residual continuum contamination. Note that the OH morphology greatly differs from both the CN and C_2. North is down and east is left on all images presented here. The position angle of the Sun in March is PA_{Sun}=151°.

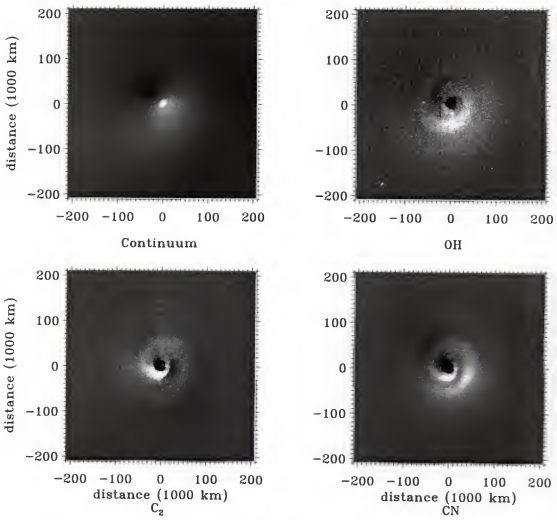

Figure 4-2: OH, CN, and C_2 data (April 26, 1997). Dust jets are only visible in the sunward direction while gas jets are evident in both the sunward and anti-sunward directions. The anti-sunward gas jets are somewhat weaker in approximately the anti-solar direction, and brighter in the sunward direction (PA_{Sun}=247°) to roughly PA=300 degrees (westward on the CCD).

anti-sunward asymmetries and thus was applied to the majority of the images presented here. Most dust images shown were processed with an unsharp mask because a strong sunward/anti-sunward difference rendered the MAS technique inadequate (Fig. 4-6).

Each image processing method yields the same conclusion: jets are evident in all species, including dust, OH, CN, and C_2. The continuum (dust) images show varying jet structure, but the structure is generally restricted to the projected sunward direction. The sunward direction is approximately the lower half of the March images and the right half of the April images. In contrast, the gas images display jet structure in both the sunward *and* the anti-sunward directions (i.e., in the upper (March) or left (April) half of the image). There is some indication of a low signal anti-sunward dust jet very near the nucleus (within $\approx$ 15 to 20″ of the central condensation) in both the March and April images. These are faintly discernible on the computer display, but not in any hardcopy of the images. In contrast, the gas jets extend well beyond this distance in the anti-sunward direction.

The existence of gas jets with no spatially coincident dust jets is significant because part of the signal in the gas images is due to the underlying continuum, which can be difficult to accurately eliminate. If the continuum is not properly removed, this could lead to an erroneous report of jets created by the gas. Thus, one must be careful in identifying gas jets if a spatially coincident dust jet is apparent. For example, before the continuum is removed, the dust jets in March seem to coincide with gas jets on the sunward side in all gas species. At first glance, this appears to be true for the CN and C_2 images in April, but there are distinct differences between dust jet and OH jet morphology during April. After the continuum is removed, it is apparent that the gas jets are thicker than the dust jets in all images and in both months. Since there is no evidence for dust jets (past $\approx$ 10 to 15″ of the central condensation) in the anti-sunward direction, these jet features can confidently be

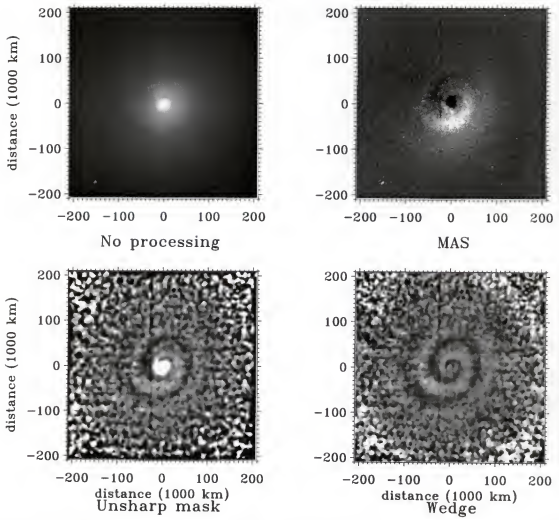

Figure 4-3: OH data with various image processing techniques applied. April 26, 1997: Montage of OH data images. The first is OH with no image processing routine applied. The Minimum Azimuthal Subtraction (MAS) routine, an unsharp mask, and the wedge subtraction routine were applied to the images as noted. A gaussian filter is applied to the images that were processed with the unsharp mask and wedge subtracted routines to smooth the background noise. All images are stretched to further accentuate the jets.

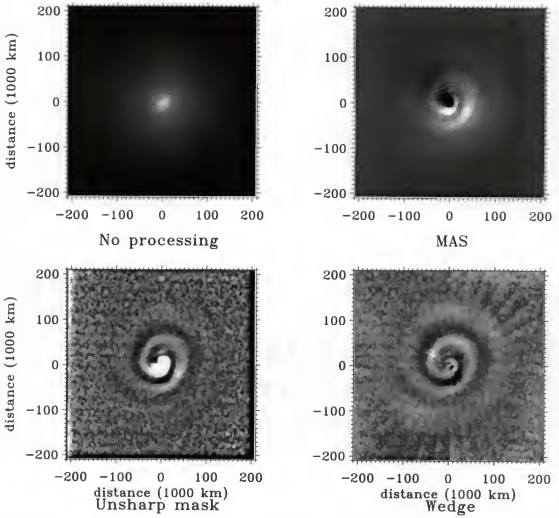

Figure 4-4: CN data with various image processing techniques applied. April 26, 1997: Montage of CN images. Same as Figure 4-3.

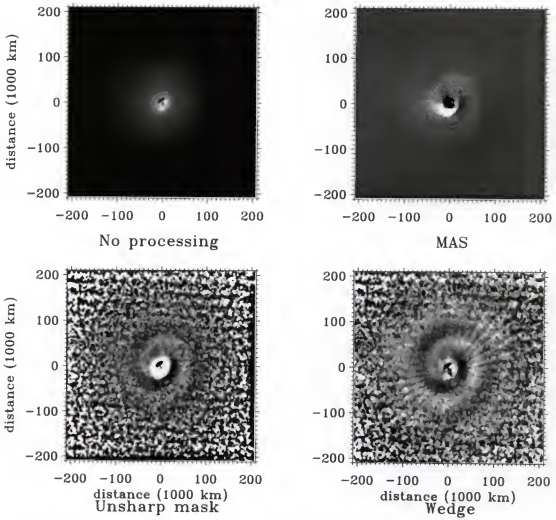

Figure 4-5: C_2 data with various image processing techniques applied. April 26, 1997: Montage of C_2 images. Same as Figure 4-3.

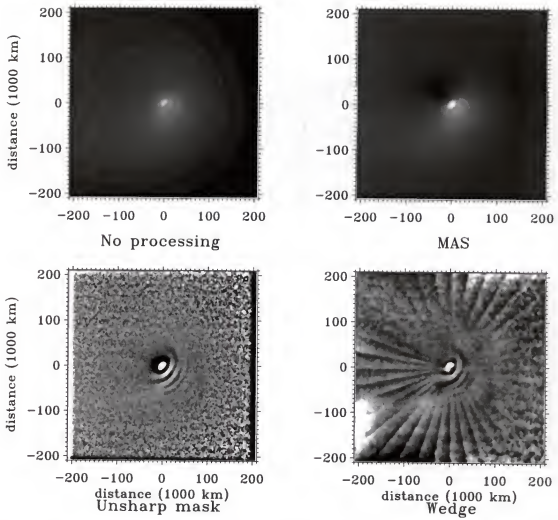

Figure 4-6: Continuum data with various image processing techniques applied. April 26, 1997: Montage of continuum images. Same as Figure 4-3.

attributed to the gas. The same is true in the sunward direction after an accurate continuum subtraction is applied.

Estimates of the underlying continuum are made from analyzing the signal in a 56″ square aperture. This size was chosen to allow comparison with the results from the photoelectric photometer. The 56″ square photometer aperture was chosen to monitor any changes throughout the course of a night because it is large enough that minor errors in centering the comet in the aperture have little effect on the data, yet it is small enough that the sky background does not dominate the signal. The amount of underlying continuum decreases with increasing aperture.

The continuum contributes only 10% of the total signal in 56 square arcseconds in the OH images. Hence a less-than-perfect continuum subtraction from OH images, while still a concern, is not nearly as problematic when identifying jets in the OH images as it is for the C_2 images whose raw signal includes $\approx$ 60 to 70% continuum. This is evident when comparing the continuum contaminated versus continuum subtracted OH images taken in April (Fig. 4-8). However, this does not hold for the March OH data (Fig. 4-7). An accurate continuum subtraction is critical for OH as well as the other gas species when identifying the gas jets in the sunward direction for this month.

4.2.2 Comparing the Morphology of OH, CN, and C_2

Before the filter set was calibrated, the continuum subtraction was not possible. At that time, it appeared that the carbon species jets behaved one way and the OH jets another. A comparison of the anti-sunward jets showed that the CN and C_2 jet peaks and troughs overlap spatially, though the CN jets are better defined than the C_2 jets. The reverse is true for the OH anti-sunward jets – where OH peaks, CN and C_2 display troughs and vice versa. However, after the continuum subtraction was completed, it became clear that the apparent correlation between the carbon

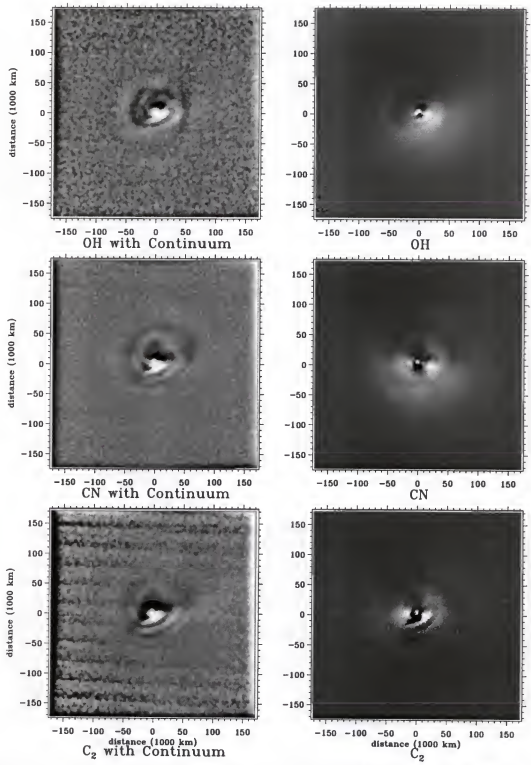

Figure 4-7: Gas images before and after continuum correction (March 6, 1997). The MAS technique is applied to all pure gas images. An unsharp mask is applied to the continuum contaminated gas images to allow a greater contrast of the jets.

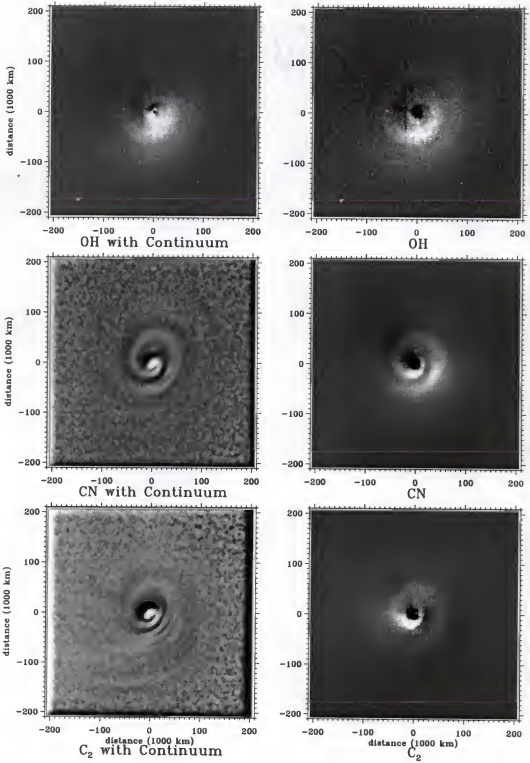

Figure 4-8: Gas images before and after continuum correction (April 26, 1997). The MAS technique is applied to all images except the continuum contaminated CN and C_2 images. An unsharp mask is applied to the latter images to allow better contrast of the jets.

species and anti-correlation between these species and OH does not hold in the sunward direction (Figs. 4-7, 4-8). In the sunward direction, CN and C_2 look quite different. The C_2 jets are broader and are projected at distances farther from the nucleus than the CN jets. Surprisingly, OH and CN, while not precisely the same, resemble each other in the sunward direction. Here the locations of the OH and CN troughs approximately correspond to the peaks of the C_2 jets and vice versa.

At first glance, one might assume that an incorrect amount of continuum was subtracted from the CN image, but the C_2 and OH images were properly calibrated. Two dust jets do coincide with the brightest sections of the CN spiral in the sunward direction. Perhaps the contribution from these dust jets is responsible for the increased brightness where the OH and CN overlap in the sunward direction. This raises the question: if a different amount of continuum were subtracted, would the morphology of the sunward CN jet reflect the morphology of the C_2 jet? Two possible scenarios could result in an incorrect continuum subtraction. First, the automatic calibration routine may not have calculated the right ratio of underlying continuum in the CN images. This could occur if the photometric conditions varied between the time when the CN images were taken and the continuum images were taken. To test this theory, a greater amount of continuum was subtracted from the CN image than the automatic calibration routine determined was present, ranging from a few percent more to twice as much continuum. Even after subtracting so much continuum that artifacts were created in the near-nucleus sunward spiral jet, the CN jet that is coincident with the sunward OH jet did not disappear (Fig. 4-9).

Alternatively, one might suspect that the locations of the dust jets moved a significant distance between the times when the CN and dust images were taken. Perhaps that offset was great enough that the continuum was not accurately removed during the absolute calibration process. However, only 3 minutes separated the time between the CN and dust exposures shown in Fig. 4-9. In contrast, 5 minutes and 16

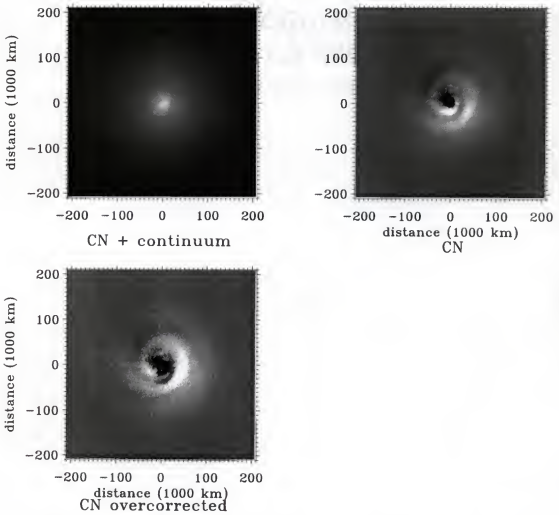

Figure 4-9: CN continuum contamination analysis. April 26, 1997: a) CN before the continuum was subtracted, b) pure CN after the correct amount of continuum was subtracted, and c) CN after twice as much continuum was subtracted. This demonstrates that the brightest portion of the jet in the sunward direction is created by CN, not by any underlying contribution due to dust.

seconds separated the time between the dust and C_2 exposures, and the movement of the dust jets was small enough that the dust could be accurately eliminated from the C_2 images. Recall that the underlying contribution from the continuum is nearly three times higher in the C_2 images compared with the CN images. Therefore, a significant shift in locations of the dust jets should have a more apparent affect in the continuum corrected C_2 images than the CN images. Physically, the dust reaches an actual expansion velocity of approximately 1 to 1.5 km/s. In 3 to 5.25 minutes, the dust jets have moved between 180 to 500 km, corresponding to a maximum of 1/3 of a pixel in my images, which is not enough to create an incorrect continuum subtraction.

In general, one should consider any gas jets whose morphology coincides with the dust jets to be suspect. However, the above arguments suggest that the contrast differences in the sunward direction are due to a greater amount of gas present in the sunward jets and not due to continuum contamination.

4.2.3 Jet Widths

The CN jets have relatively well defined edges in contrast with the other gas species. Compared with the CN jets, the OH jets appear more diffuse, as though either the collisions are collimating the CN more effectively. Alternatively, the CN could be emitted directly from CHON grains and the OH could be a secondary product from the CHON grains (e.g., if H_20 is emitted from the CHON grains with a very low initial velocity and the OH is emitted from the H_20 molecule). C_2 appears more diffuse than either the OH or the CN, especially in the innermost coma. This might result if C_2 were a granddaughter and/or great-granddaughter product of the organic grains. CHON grains might emit C_3 and/or C_2H_2, possible precursors of C_2. If both OH and C_2 are granddaughter products, the parent molecules emitted from the CHON grains must be moving slowly compared with the speed of the grains. The velocity of the granddaughters would need to be confined as well to allow the

observed radicals to retain their identity as a jet, yet appear more diffuse than the CN jets. Collisions could restrict their velocities.

Jet widths were measured by plotting brightness in a given direction as a function of ρ, projected distance from the nucleus, and fit with a Gaussian profile. The full width at half maximum (FWHM) is used as jet width. The portion of the jets closest to the nucleus (within roughly 10 to 15,000 km or 15″ of the nucleus) was not measured because the strong contamination from the continuum made it difficult to determine where to mark the FWHM of the inner portion of the jet.

At their thinnest, the OH and CN jets are roughly 8,000 km. In both cases, this occurs in the anti-sunward direction. The C_2 jets are approximately 20,000 km at their thinnest point. At their widest, all three species are roughly 50,000 km. The precise FWHM of the more distant jets is more difficult to ascertain (Fig. 4-10). This is due in part because the wider jets are less well defined (i.e., more diffuse) and lower contrast with respect to the signal in the surrounding regions. In addition, the jets are asymmetric, partially because the signal drops as the coma expands away from the nucleus, and partially because several active areas are responsible for the spiral morphology (see Section 4.3.8). This made it difficult to fit Gaussian profiles to these jets. In all cases, errors in jet width are $\approx$10%. The jet morphology remains relatively confined within projected distances of $\approx 70,000$ km. Beyond this distance, the jets become very diffuse very quickly, perhaps because collisions are significantly less frequent by these distances. Alternatively, this diffusion may be due to the destruction of the parent grains – namely, all the radicals produced by grains are created within 70,000 km and simply diffuse beyond this point.

4.2.4 Evolution of the Jets with Time

Comet Hale-Bopp reportedly underwent a series of jet formation, evolution, and dissipation between August and October, 1995 as indicated by monitoring BVRI filter images (Kidger, ApJ). A more dramatic change occurred throughout the months

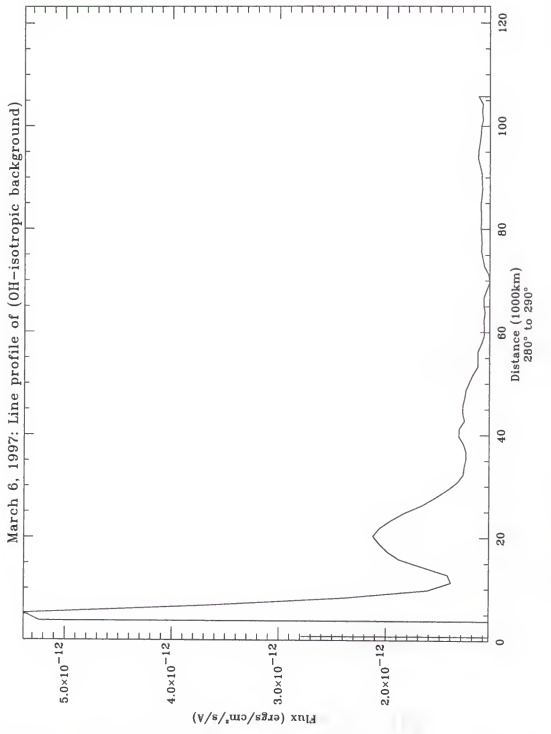

Figure 4-10: Radial profile of jets. March 6, 1997: Radial profile the OH jets between position angles of 280 to 290°. An isotropic background was subtracted from the image before the radial profile was extracted. Gaussian profiles were fit to each jet to determine their widths.

preceding the comet's approach to perihelion in 1997 and prior to our observations. Six months before perihelion, the jets displayed a morphology commonly described as 'porcupine' or 'hedgehog'-like. The jets appeared as straight, radial rays originating at the central condensation and did not change appreciably with time. This made any attempts at determining its period of rotation essentially impossible. However, by February (two months before perihelion), the morphology of the jets changed from porcupine-like rays to curved arcs and spiral shapes. Astronomers were able to apply various techniques to this latter morphology to calculate the period of Comet Hale-Bopp. The results demonstrated remarkable consistency of 11.3 hours. (Jorda et al. 1997, Farnham et al. 1999, Sarmecanic et al. 1997). This is a crucial input parameter in my Monte Carlo models.

The morphology also changed significantly after perihelion, allowing several groups to estimate Comet Hale-Bopp's pole orientation (e.g., Samarasinha et al. 1997, Vasundhara and Chakraborty 1999, hereafter VC99). April's morphology suggested that the pole was pointing almost directly toward Earth and made estimating the pole position easier. My April images display the simple spiral morphology that facilitated astronomers in determining the pole position. Through the models, it was determined that the VC99 pole orientation best fits the data analyzed here.

4.3 Monte Carlo Model Analysis

The set of model input parameters chosen affect the following observable quantities in the data:

- The behavior of the radial profile (surface brightness vs. ρ, distance from the central condensation);
- % Enhancement of the jets above the diffuse background;
- Jet width;
- Projected expansion velocities; and

- General morphology.

The radial profile of a model that invokes a pure nuclear gas source demonstrates the need for an extended source. Near the nucleus, the model's radial profile is much too steep compared with the data. However, adding an extended source eliminates this discrepancy if the correct balance of radicals from gas and grain sources are combined. Thus, the radial profiles are used to determine the correct gas to grain ratio when testing the accuracy of each parameter. To aid in determining how accurately the model reproduces the data for a given set of input parameters, a program was applied that calculated the gas to grain ratio that best fit the data. The model is also normalized to the total flux of the data. This method was used to create radial profiles to analyze each of the parameters discussed below. Once 'good' fits to the morphology were attained, the parameters were refined through a quantitative analysis of the model's radial profile fit to the data using the amoeba routine in IDL (see Section 3.2.3). In all cases, the Monte Carlo statistical errors are smaller than the thickness of the lines plotted.

While certain parameters affect several of the observable quantities, others might only create noticeable changes in one observable. Therefore, it is important to watch how the parameters affect each of the above listed observables. A full range of parameters was tested based on estimates found in the literature when possible and are listed in Chapter 3 (Table 3-1). Reasonable estimates were made for the remaining parameters. The parameters were narrowed down initially by determining the best fit by eye, and were further refined through applying the amoeba routine to the radial profile as described in Chapter 3. The best-fit parameters are listed in Tables 4-1, 4-2, and 4-5. In this section, the effects caused by each parameter are discussed.

Table 4-1: Species-dependent model input parameters.

Parameter	OH	CN	C_2
τ_g (sec) [$\pm 0.2 \times 10^4$]	8.2×10^4	2.5×10^4	2.6×10^4
τ_p (sec) [$\pm 0.2 \times 10^4$]	4.0×10^4	3.0×10^4	3.4×10^4
τ_d (sec) [$\pm 0.2 \times 10^4$]	1.9×10^5	3.5×10^5	1.5×10^5
v_p (km/s) [± 0.01]	0.4	0.4	0.4
dv_o (km/s) [± 0.03]	0.15	0.22	0.25
α [± 0.002]	0.13	0.13	0.13
v_d (km/s)[± 0.1]	1.05	0.5	1.2

Note: Input parameters vary depending on the radical observed, including τ_g, the time it takes for production of parents to peak for a grain source; τ_p, the lifetime of the parent gas; τ_d, the lifetime of the daughter; v_p, the initial velocity of the parent; dv_o, the range of initial velocities; α, the acceleration parameter due to heating in the coma; and v_d the daughter velocity.

Table 4-2: Model input parameters.

Parameter	March	April
Source	grain or gas	grain or gas
$N_{particles}$	600	600
t_F (sec)	2.4×10^6	2.4×10^6
dt (sec)	3000	3000
P_r (°/dt)	26.530	26.530
pixel size (km)	1165	1392
α_p (°)	285	285
δ_p (°)	-55	-55
Day	1,3,5,6	22,23,26
Time of exposure (hours)	image dependent	image dependent
PA_{Sun} (°)	154 to 159	239 to 247
phase (°)	42.0 to 44.5	33.4 to 36.0
a_{rp} (cm/s^2)	2.0	2.0

Note: Additional input parameters that are not dependent on the observed radical include the source generating the radical (grain, gas); $N_{particles}$, the total number of particles generated per timestep; t_F, the length of the simulation; dt, the length of each timestep; P_r, the period of rotation of the nucleus in one timestep; dt, the length of each timestep; pixel size, the size of each pixel in kilometers; α_p and δ_p, the right ascension and declination of the comet's pole; the day and time the comet image was taken; PA_{Sun}, the position angle of the Sun; *phase*, the Sun-comet-Earth phase angle; and a_{rp}, the acceleration due to radiation pressure. Some vary depending on the month (e.g., pixel size). Others vary depending on time the image was taken (PA_{Sun}, *phase*).

4.3.1 Gas versus CHON Grain Source

The morphology of the gas jets depends on the source of the radicals. In the data images, one can see that the jet brightness appears to peak not at the nucleus but rather at some distance away. This effect is illustrated in Figs. 4-11, 4-12, and 4-13 where in the bottom left image, the jets are created through a nuclear gas source jet while on the top right, an extended CHON source jet is active. The morphology of the OH model matches the data remarkably well when a diffuse nuclear molecular source is combined with a triangular extended source (see Section 3.2.2 for a description of the triangular source).

The behavior of the radial profiles also indicates that a source peaked at some distance from the nucleus is required to reproduce the profiles (Fig. 4-14), as will be discussed in Section 4.3.3. The radial profile cannot be reproduced with a pure molecular gas source whether collisions act to collimated their path or not. However, collisions may help to explain why the jets observed in Comet Hale-Bopp were much more confined than the jets observed in Comet Halley at similar projected distances from the nucleus.

Radial profiles representing wedges in the sunward and anti-sunward directions demonstrate how well the models reproduce the jets observed in the data. The OH models fit the data well in all directions; maximum errors in the model fits range from 8 to 10% where the jets are located (within 100,000 km) (Figs. 4-15 and 4-16, respectively). The maximum error in the intensity of the CN jets is 13% in the anti-sunward direction (Fig. 4-18) and range from 10 to 17% in the sunward direction (Fig. 4-17). The C_2 jets are the least constrained of the three species, and the maximum errors in the radial profiles (which range from 15% in the sunward direction to 23% in the anti-sunward direction) reflect this (Figs. 4-19).

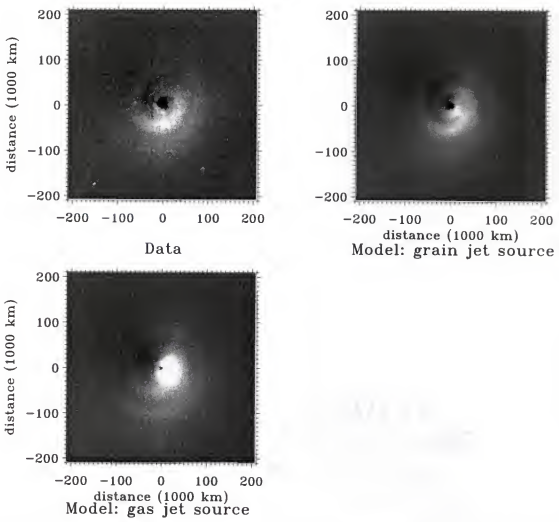

Figure 4-11: OH data and models with gas and triangular CHON grain jet sources. April 26, 1997: a) OH data, b) the Monte Carlo model of OH with an extended grain jet source + diffuse molecular gas source, and c) the Monte Carlo model of OH with a nuclear gas jet source + diffuse molecular gas source. The jets produced with a nuclear gas source are too bright near the center and too dim far from the nucleus to accurately recreate the jet morphology. Jets produced by a grain source (b) reproduce the jets seen in the data well.

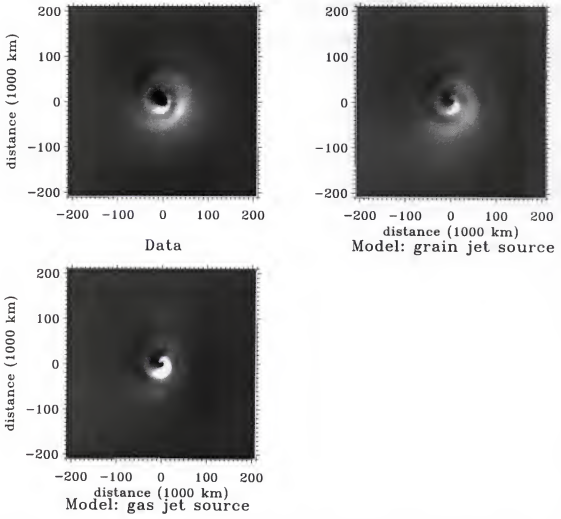

Figure 4-12: CN data and models with gas and triangular CHON grain jet sources. April 26, 1997: Same as Figure 4-11 for CN.

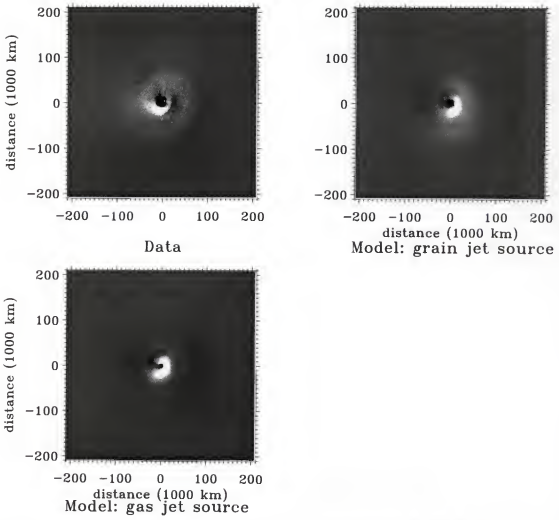

Figure 4-13: C_2 data and models with gas and triangular CHON grain jet source. April 26, 1997: Same as Figure 4-11 for C_2.

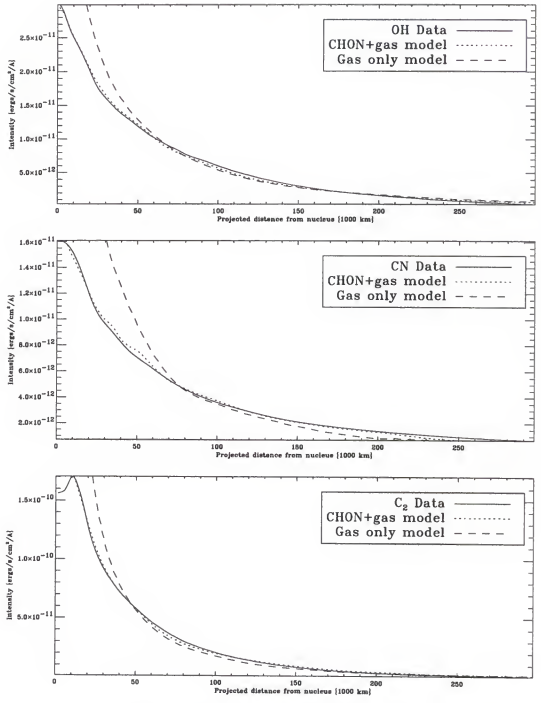

Figure 4-14: Radial profiles of the data and best-fit models for all gas species. April 26, 1997: Radial profiles of the data, the Monte Carlo model that combines an extended CHON grain jet source plus a diffuse gas source (CHON+gas model), and the Monte Carlo model that combines a nuclear gas jet source plus a diffuse gas source (Gas only model). The radial profile of the model that employs an extended CHON grain source matches the data well; a nuclear gas jet source does not fit the data near the nucleus with any combination of input parameters.

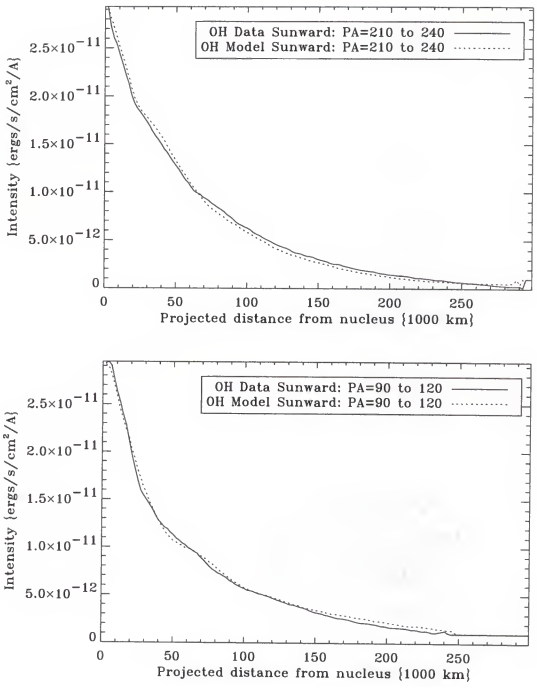

Figure 4-15: Radial profiles of OH data and models in the sunward direction (April 26, 1997). The profiles represent the average intensity as a function of distance from the nucleus within 30° wedges. The position angles included in the wedge are noted in the plots. Errors range from less than 1% to 8% for both plots.

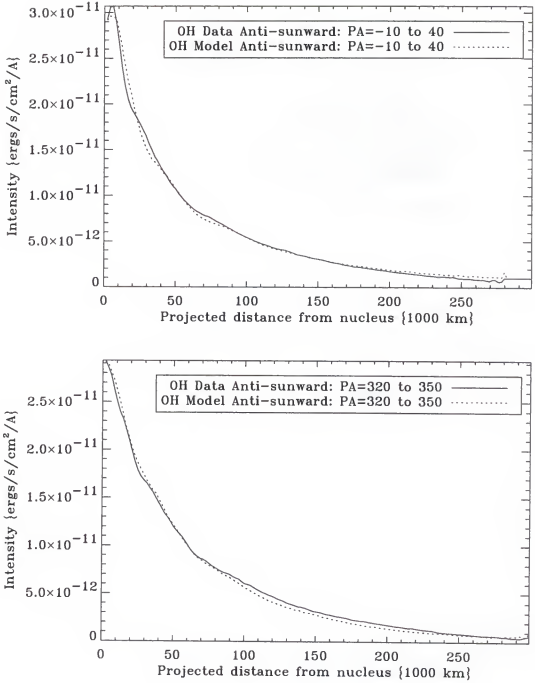

Figure 4-16: Radial profiles of OH data and models in the anti-sunward direction (April 26, 1997). The profiles represent the average intensity as a function of distance from the nucleus within a 50° wedge for the upper plot and within a 30° wedge for the lower plot. A larger wedge was used for the upper plot to improve the signal-to-noise of the resultant profile. Errors range from less than 1% to 10%.

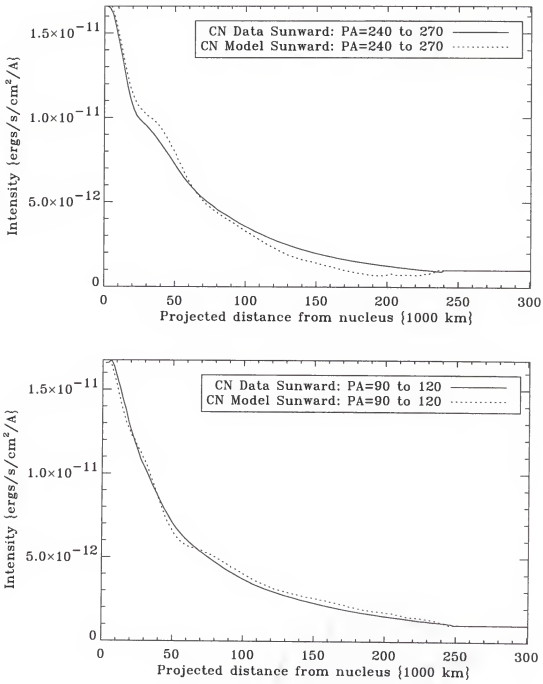

Figure 4-17: Radial profiles of CN data and models in the sunward direction. Same as Figure 4-15 for CN. Errors range from less than 1% to 17% for the upper plot and less than 1% to 10% for the lower plot.

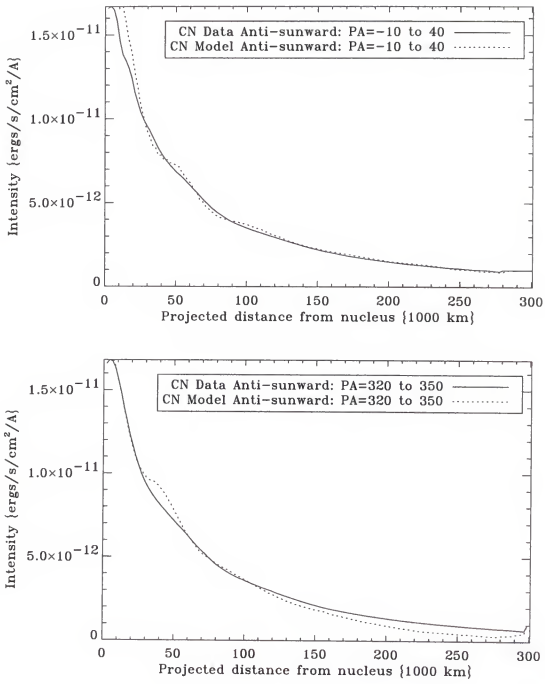

Figure 4-18: Radial profiles of CN data and models in the anti-sunward direction. Same as Figure 4-16 for CN. Errors range from less than 1% to 13% for both plots.

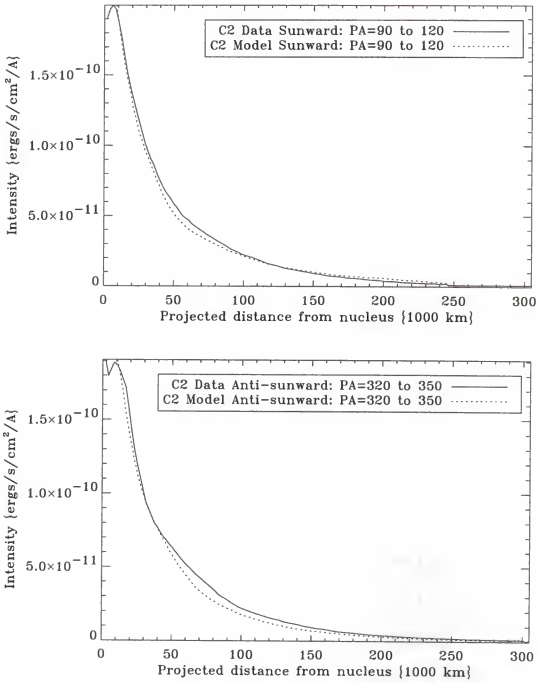

Figure 4-19: Radial profiles of C_2 data and models in both directions (April 26, 1997). Here, the upper plot represents the sunward direction. The lower plot represents the anti-sunward direction. The profiles represent the average intensity as a function of distance from the nucleus within 30° wedges. One direction is represented for each direction since the morphology of C_2 is more simplistic. Errors range from less than 1% to 15% in the upper plot and from less than 1% to 23% for the lower plot.

4.3.2 Initial Parent Velocity and Alpha Parameter

The data show that the gases accelerate as they move away from the nucleus, as can be seen by the change in expansion velocity with distance from the nucleus (Table 4-3). This effect is included in the models through the combination of two parameters: the initial parent velocity, v_p, and the alpha parameter, α, as described in Chapter 3. This set of parameters affects (a) the projected expansion velocity, (b) the morphology (by affecting where the jets are located), and (c) the radial profile.

If v_p and α create an acceleration that is too low, the projected expansion velocity is too low and the spiral jets are wound too tightly. The reverse is true if these parameters create an acceleration that is too high (Fig. 4-20). The radial profile is affected because the morphology affects how the brightness changes with distance from the nucleus. If the peaks of the jets do not fall at the proper locations, the resultant radial profile will be too high at the distances where the jets are incorrectly located in the model, and too low at distances where the jets were supposed to have reached (Fig. 4-21). Finally, the locations of the jets are partially dependent on these two parameters, thus it is important to find a set of v_p and α that works for *all species* to determine the locations of the jets. For example, if the combination of v_p and α results in an acceleration that is slightly different from another set of v_p and α, the longitudes of the jets derived by the model may be slightly higher or lower.

As was noted in Chapter 3, a family of solutions exists for this parameter. The data do not allow a unique determination of v_p and α; rather, they allow us to find a set that correctly reproduces the observed acceleration. Values of 0.4 and 0.13 respectively are consistent with the best fit velocity parameters (0.5 and 0.14, respectively) found by Lovell (1999), using radio data taken on March 20, 24, and 30, 1997, one month prior to my April observations.

Furthermore, hydrodynamic models demonstrate that the flow velocity near the surface of the nucleus begins near sonic speeds of 0.38 km/s (Marconi and Mendis

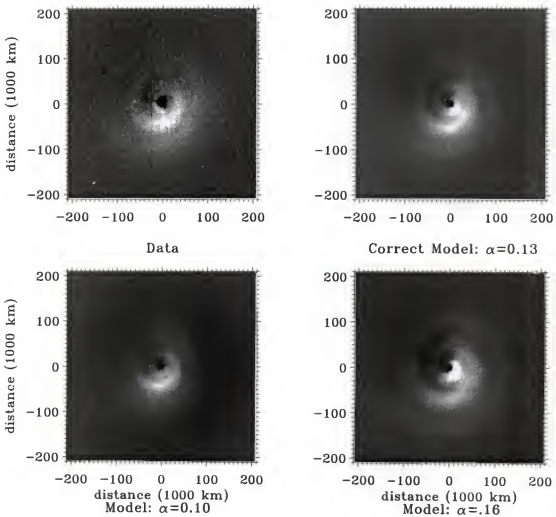

Figure 4-20: Acceleration (α) parameter analysis (images). April 26, 1997: OH images of a) the data, b) the Monte Carlo Model with the best fit (v_p, α) combination, where $\alpha = 0.13$, yields the correct acceleration in the coma c) the Monte Carlo Model with too little acceleration, $\alpha = 0.10$, and d) the Monte Carlo Model with too much acceleration, $\alpha = 0.16$. Similar effects are observed when α is held constant and v_p is decreased or increased.

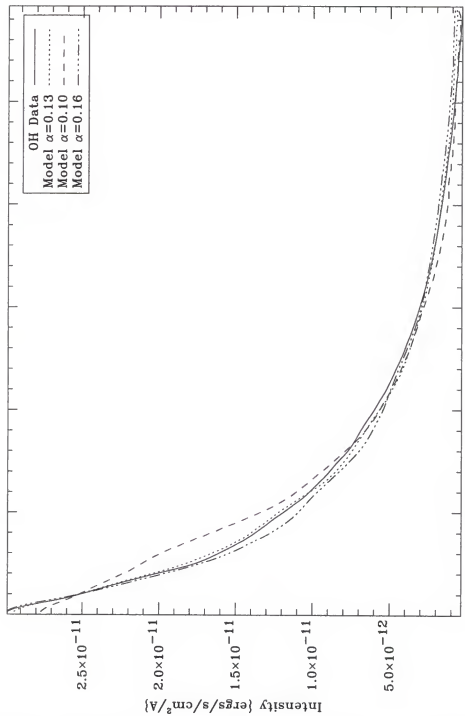

Figure 4-21: Acceleration (α) parameter analysis (radial profiles). Radial profiles that correspond to the images in figure 4-20.

1982a,b, 1983, Ip 1983, Crovisier 1984). Molecules then increase their speed due to adiabatic expansion to near 1 km/s as they flow away from the nucleus. These findings support the choice of 0.4 km/s as the velocity of the parent upon release from the nucleus.

4.3.3 Range of Initial Parent Velocities

The jet width increases dramatically for all species beyond 70,000 km of the central condensation in the images. The jets themselves are no longer discernible beyond 125,000 km. This effect is controlled in part by the range of initial parent velocities. Physically, the parent grains will be swept away from the nucleus with a range of speeds. When all grain parents are given the same initial velocity, the jets are too narrow and are conspicuous well beyond distances that the jets are seen in the data (Fig. 4-22). If the range is too high, the jets lose their identity too close to the nucleus. Allowing an appropriate range of initial velocities, ranging from ± 0.05 km/s for OH to ± 0.125 km/s for the carbon species, creates a morphology consistent with the data.

4.3.4 Daughter Velocity

The daughter velocity affects both the radial profile and morphology. Using a single jet as an example, one can see that the jet created with a higher daughter velocity fades into an isotropic background at distances much closer to the nucleus than the jet created with a much lower daughter velocity (Fig. 4-23). Using a very low daughter velocity allows the jets to retain their identity at distances beyond that which is seen in the data. This is consistent with the fact that the CN jets, which require a lower daughter velocity, are distinct at distances well beyond those of the C_2 jets, which are reproduced with a higher daughter velocity.

Because the jet peaks and troughs can cancel one another if they overlap, the act of increasing the daughter velocity too much (e.g., to 2.0 km/s) actually acts

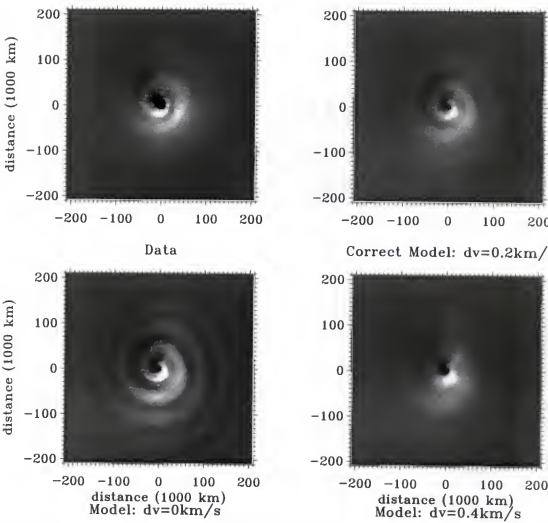

Figure 4-22: Range of initial parent velocities parameter analysis (images). April 26, 1997: CN images of a) the data, b) the Monte Carlo Model with the best fit range of initial parent velocities, dv = 0.2 km/s, c)the Monte Carlo Model with the same initial parent velocity for all particles, dv = 0 km/s, and d) the Monte Carlo Model with a range of initial velocities that is too large, dv = 0.4 km/s. CN is used as an example here instead of OH because it demonstrates the effects of changing this parameter more clearly.

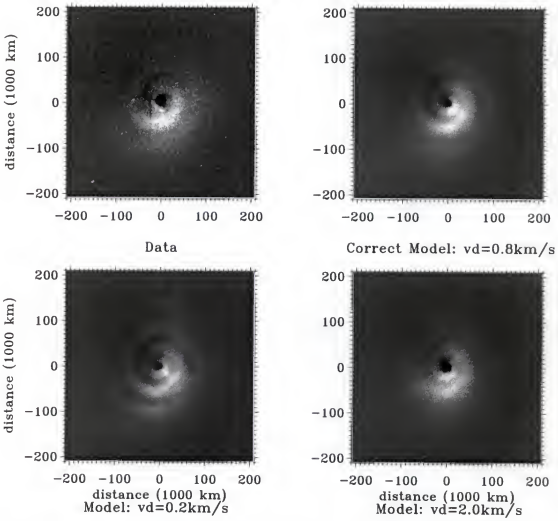

Figure 4-23: Daughter velocity parameter analysis (images). April 26, 1997: OH images of a) the data, b) the Monte Carlo Model with the best fit daughter velocity, $v_d = 0.8$ km/s, c) the Monte Carlo Model with a daughter velocity that is too low, $v_d = 0.08$ km/s, and d) the Monte Carlo Model with a daughter velocity that is too high, $v_d = 20$ km/s.

to 'erase' the morphology of the jets (Fig. 4-23). However, a daughter velocity of 0.5 km/s for the CN, and 0.8 km/s for OH allows the jets to maintain their distinct identity out to appropriate distances.

An example of the need to watch both the radial profile and the morphology is best shown by varying the daughter velocity. Both the velocity and lifetime of the daughter will increase or decrease the brightness of the inner radial profile ($< 80{,}000$ km). However, while an increase in the daughter velocity can create a closer fit to the radial profile with the right combination of input parameters (Fig. 4-24), the morphology is completely lost in the process (Fig. 4-23). Thus, other parameters were adjusted to find the best fit to both the morphology and radial profile of the data.

The range of values tested for the daughter velocity was chosen to span the possible velocities the radicals might have, depending on whether they are produced by a gas through photodissociation, or grain through photosputtering or thermal dissociation (see Section 4.3.3). Daughter radicals that photodissociate from a parent gas are emitted with velocities near 1 km/s for the species discussed here. The velocities of radicals produced directly by grains are unknown but may range from very low (negligible) velocities to values at least as high as radicals that are produced through photodissociation. Because we do not know what mechanism produces the radicals originating from grains, values up to twice that of photodissociated radicals were tested.

4.3.5 Lifetimes of Parent and Daughter

Both the radial profile and the morphology are affected by the lifetimes of the radicals and their parents, whether gas or grain. The parameter equivalent to the parent lifetime for a CHON source dictates how long it takes for production from the grains to peak, τ_g. This translates to a distance at which the jet brightness peaks

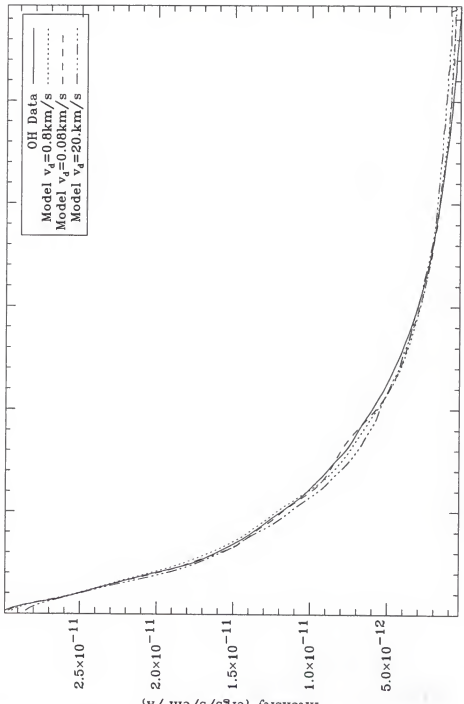

Figure 4-24: Daughter velocity parameter analysis (radial profiles). The profiles here represent the data, the Monte Carlo model that best fits the morphology ($v_d = 0.8$ km/s, and Monte Carlo models whose daughter velocity is too low ($v_d = 0.2$ km/s) and too high ($v_d = 20$ km/s). These profiles correspond to the images in figure 4-23.

with distance from the nucleus. Smaller values of τ_g create jets that are brighter near the nucleus; the resultant morphology resembles a nuclear gas source.

As expected, the radial profile is also affected. If the parent lifetime is too short, the radial profile is too peaked near the nucleus. If the production rate from the grains peaks close to the nucleus, it yields a surplus of observed radicals too close to the nucleus. Renormalizing the radial profile in an attempt to fit the inner 30,000 km creates a dearth farther from the nucleus where only radicals produced from the exponentially decaying isotropic gas source remain (Fig. 4-25).

The reverse occurs with parent lifetimes that are too long. The radicals are produced too far from the nucleus. The resultant radial profile is flattened with either too few radicals in the inner coma or too many radicals produced far from the nucleus (depending on whether the model radial profile is normalized to fit the inner or outer radial profile; Fig. 4-25).

With either a grain or gas source, a shorter daughter lifetime creates a steeper radial profile beyond where the jets are located, and broadens the inner profile, equivalent to producing too many radicals in the inner coma and too few far from the nucleus (Fig. 4-26). The reverse is true for a longer daughter lifetime. The morphology appears 'flattened' with higher daughter lifetimes. In this scenario, the region beyond where the jets exist are brighter and therefore blend in with the jets. The jets stand out more against the isotropic background with lower daughter lifetimes.

While parent and daughter lifetimes affect the radial profile in a similar manner, the lifetime of the CHON parent only affects the profile to the distance corresponding to $2\tau_g$. Recall that the triangular source linearly increases to τ_g and decreases to $2\tau_g$; beyond this time, the CHON grains no longer produce radicals. The daughter lifetime affects the radial profile in a different manner and beyond the distance where the CHON parent lifetime has an affect as described above.

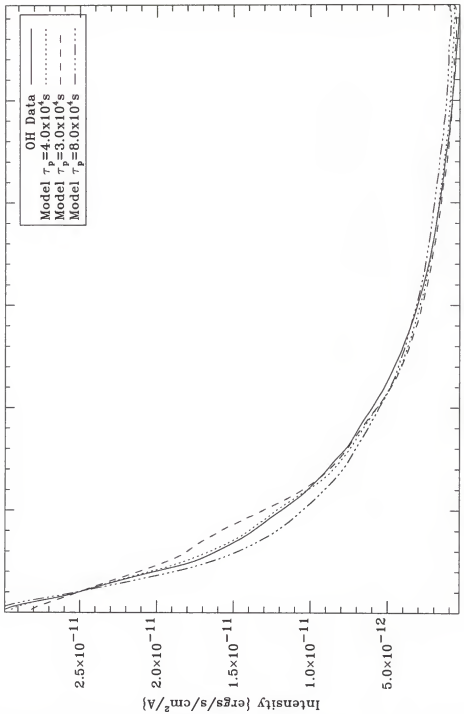

Figure 4-25: Parent lifetime parameter analysis (radial profiles). The radial profiles represent the data, the best fit Monte Carlo model, and Monte Carlo models with parent lifetimes that are too long and too short for the extended CHON grain jet model.

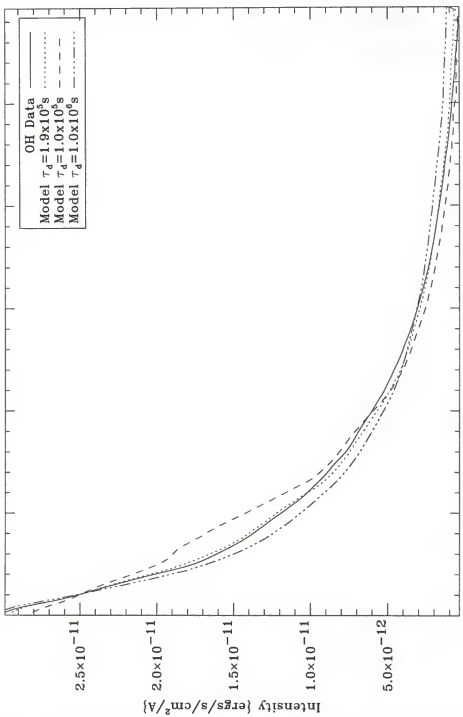

Figure 4-26: Daughter lifetime parameter analysis (radial profiles). The radial profiles represent the data, the best fit Monte Carlo model, and Monte Carlo models with daughter lifetimes that are too long and too short for the extended CHON grain jet model.

4.3.6 Radiation Pressure

Radiation pressure affects the brightness symmetry; it causes the diffuse component to be slightly brighter in the anti-sunward direction, the direction that the radiation pressure is sweeping particles towards, and slightly dimmer in the sunward direction. Radiation pressure is given by

$$m\frac{dv}{dt} = \int \frac{F_\nu}{r^2}\frac{h\nu}{c}\sigma(\nu)d\nu \qquad (4\text{-}1)$$

where m is the particle's mass, F_ν the solar flux at frequency ν, r_h the heliocentric distance of the comet in AU, $h\nu/c$ the momentum of the photon, and σ the cross section of the particle at ν. Typically, 2 cm/s^2 has been used in Monte Carlo models of the gas coma (Combi and Delsemme 1980), and through testing, proved to be the best choice in my models. Higher values created an abnormally high brightness level in the direction of the radiation pressure, i.e., on the left side of the image beyond the distances the jets are located. When radiation pressure is not included or is too small, the brightness asymmetry observed in the data is not re-created (Fig. 4-27).

4.3.7 Phase Angle, PA_{Sun}, Sun's Cometocentric Location

The position angle of the Sun, the phase angle, and the orientation of the comet's rotational pole act together to create our viewing geometry of the comet. The position angle is the angle measured counterclockwise from north (PA=0°) through east as projected on the plane of the sky, where east is PA=90°, south is PA=180° and west is PA=270°. The position angle of the Sun is the direction, projected onto the plane of the sky, that points toward the Sun. It is obtained from the ephemerides of the object. The phase angle is the Sun-comet-Earth angle.

Estimates of the right ascension, α_p, and declination, δ_p, of the pole include: ($\alpha_p = 275°, \delta_p = -57°$) (Jorda et al. 1997), ($\alpha_p = 257°, \delta_p = -61°$) (Sekanina 1998), ($\alpha_p = 270°, \delta_p = -43°$) (Samarasinha et al. 1997), ($\alpha_p = 256°, \delta_p = -53°$) (Samarasinha priv. comm.), ($\alpha_p = 240°, \delta_p = -57°$) (Sekanina and Boenhardt 1997),

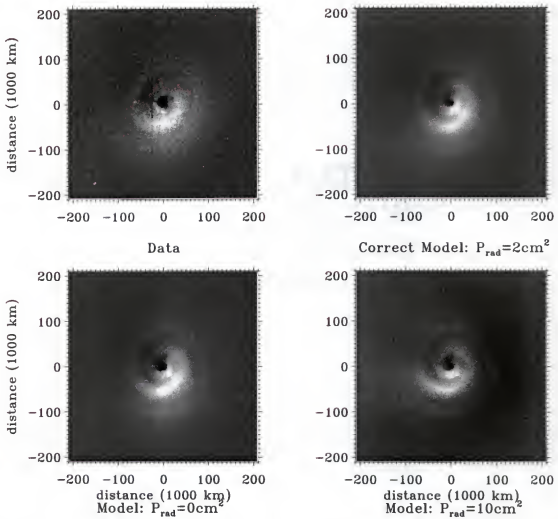

Figure 4-27: Radiation pressure parameter analysis (images). April 26, 1997: OH images of a) the data, b) the Monte Carlo Model with the correct level of radiation pressure, $P_{rad} = 2\text{cm/s}^2$, c) the Monte Carlo Model with no radiation pressure, $P_{rad} = 0\text{cm/s}^2$, and d) the Monte Carlo Model with too much radiation pressure, $P_{rad} = 10\text{cm/s}^2$. With $P_{rad} = 2\text{cm/s}^2$, the slight brightness asymmetry is recreated.

and ($\alpha_p = 275°, \delta_p = -50°$) (Licandro et al. 1997). The morphology evident in my images is best fit using the position of the pole found by VC99 using their May 2, 1997 images: ($\alpha_p = 285°, \delta_p = -55°$). The right ascension and declination are related to the inclination of the comet's equator with respect to the Earth's equator, J_{eq}, and the position of the ascending node, N_{eq}, by

$$J_{eq} = \pi/2 - \delta_p \tag{4-2}$$

$$N_{eq} = \alpha_p + \pi/2$$

Given the geocentric right ascension, α_c, and declination, δ_c, of the comet from the ephemerides of a given date, J, and N, the cometocentric latitude and longitude of the Earth can be calculated from equations given by Rhode and Sinclair (1992):

$$cosBsinU = +cosJ_{eq}cos\delta_c sin(\alpha_c - N_{eq}) + sinJ_{eq}sin\delta_c$$

$$cosBcosU = +cos\delta_c cos(\alpha_c - N_{eq}) \tag{4-3}$$

$$sinB = +sinJcos\delta_c sin(\alpha_c - N_{eq}) - cosJ_{eq}sin\delta_c$$

Here B is the cometocentric latitude of the Earth and (U+π) is the cometocentric longitude of the Earth measured from the ascending node on the Earth's equator (Fig. 4-28).

Similarly, the heliocentric latitude and longitude of the comet can be used to calculate the cometocentric position of the Sun. Using the pole position of VC99, the cometocentric latitude and longitude of the Sun is (70.25, 83.19). VC99 give further details on translating coordinates.

The trajectory of an individual particle is first calculated with respect to the location of the jet. A cone of particles is ejected from the active area with with respect to the center of the jet. The width of the cone is defined by the input parameters, and is listed as the opening angle in Table 4-5. Particles are evenly

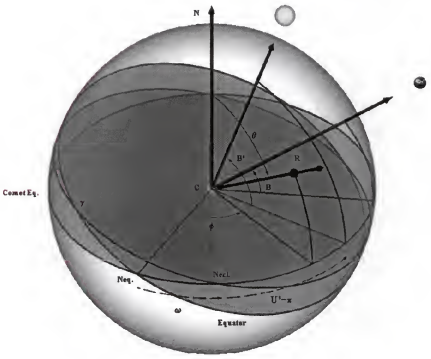

Figure 4-28: Cometocentric coordinate system. N points toward the comet's north pole; (B,U+π) is the cometocentric latitude and longitude of the Earth; (B',U' + π) is the cometocentric latitude and longitude of the Sun; both U and U' are measured along the direction of rotation of the comet from N_{ecl}; ω is the distance between N_{ecl} and N_{eq} measured along the comet's equatorial plane; N_{eq} is the longitude of the comet's ascending node with respect to the Earth's Equator; N_{ecl} is the longitude of comet's ascending node with respect to the ecliptic; (θ, ϕ) are the polar coordinates of the radical, R; γ is the first point of Ares; the Sun and Earth are shown on the diagram; Equator indicates the plane of the Earth's equatorial plane and Comet Eq. denotes the comet's equatorial plane.

distributed within the cone. The jet-centered particle trajectory is translated to its cometocentric position through the equations given by Smart (1977, sections 23 and 32). The angle between the particle's trajectory and the cometocentric position of the Sun are used to determine the proper amount of solar insolation for each area on the comet. The trajectory is then translated from a cometocentric coordinate system, whose pole is defined by the comet's north pole, to a cometocentric coordinate system, whose z-axis is pointing toward the Sun. Finally, the position angle of the Sun and the phase angle are used to translate to geocentric coordinates. This yields an image of the comet as we would see projected onto the plane of the sky. Thus, the Sun's position angle and the phase angle, along with Lambert's Law,[1] affect where the jets are brightest in the image. The Sun-comet-Earth geometry between March and May, 1997 is shown in figure 4-29.

Changing the phase angle or orientation of the comet's rotational axis twists our perspective of the morphology of the jets, dictating whether we see the jets face on, edge on, or some perspective between the two. These effects are seen most readily when comparing the March and April data. The more complex structure of the March data is due, in part, to these parameters. One can also see that the brightest portion of the jets has shifted somewhat from March to April, which depends on the position angle of the Sun. Thus, to first order, these parameters can explain why the morphology observed in March is more complex than April's morphology (Fig. 4-30).

4.3.8 Number and Positions of the Active Areas

An examination of the gas jets show that they connect smoothly from the sunward to the anti-sunward sides. This smooth morphology in the April data (Fig.

[1]Recall that Lambert's Law states that the number of particles ejected in a given direction is proportional to $(1+\cos(\theta))$ where θ is the angle between the particle's direction and the direction pointed directly at the sun.

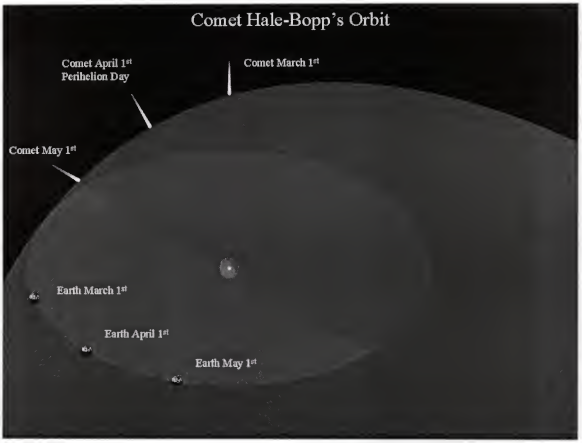

Figure 4-29: Sun-Comet-Earth geometry between March 1 and May 1, 1997. The comet reached perihelion on April 1, 1997 as is noted in the figure.

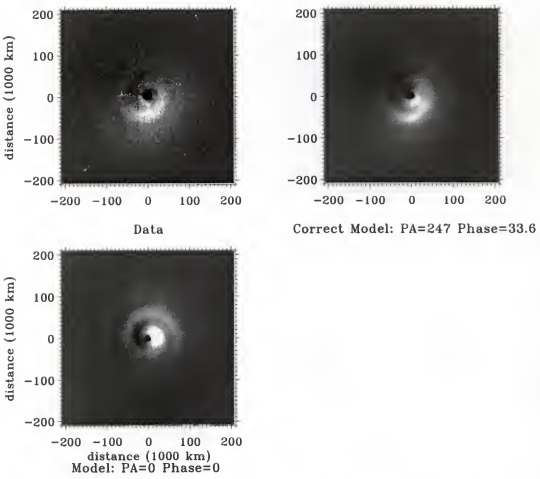

Figure 4-30: Phase angle and position angle parameter analysis (images). April 26, 1997: OH images of a) the data, b) the Monte Carlo Model with the correct position angle (247°) and phase angle (33.6°), and c) the Monte Carlo Model with the wrong position angle and phase angle (0° for both).

4-2) suggests that one active area is primarily responsible for the jets. The Monte Carlo models indicate that several additional jets are required to completely recreate the observed morphology. My models suggest that four to five regions are active during April, and more during March, even though I did not attempt to fit the more complex morphology evident during March. These results are consistent with the results found by VC99, who modeled only the dust jets. Section 4.4.2 describes the parameters used to define each active area, including location, opening angle, and the relative strengths of each jet.

4.3.9 Opening Angle of the Active Areas

Active areas that require a wider opening angle may physically correspond to a larger region spanning a greater range of latitude and longitude. For C_2, wider opening angles are required for all active areas. This implies that the C_2 molecules are not as well collimated as those whose jets can be recreated with smaller opening angles, and not that the regions producing C_2 are physically larger than the regions producing OH or CN. For all species, the active area at 60°N latitude (active area 1) requires a smaller opening angle than the lower latitude areas, suggesting that this region is physically smaller than the lower latitude active areas. This is consistent with the findings of VC99.

The opening angle of an active region on the nucleus has two effects on the morphology. The first is that it acts to 'smear' the jets out. A very narrow opening angle is more concentrated near the center of the jet; this concentration is smoothed out with a wider opening angle (Fig. 4-31). The opening angle also controls the ellipticity of an individual jet; wider opening angles create a more circularized morphology (Samarasinha 2000). This is the only parameter, save pointing the north pole of the comet directly at the Earth, that affects how elliptical the individual active areas are. One might suspect that the range of initial parent velocities, which also acts to increase the width of the jets, might also affect the ellipticity, but it does not

as can be seen in Fig. 4-22. The only other rather ad hoc way to affect the ellipticity is to combine jets at specific locations such that their individual peaks and troughs enhance and cancel each other out, to create a more circular morphology. Controlling the opening angle *and* combining the right set of active areas are required to recreate the circular morphology in the data.

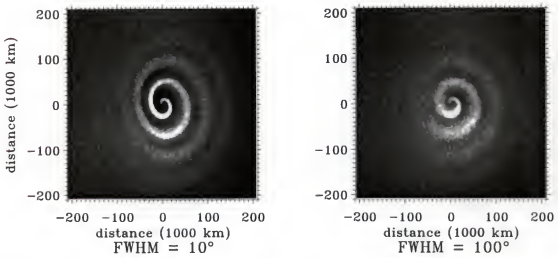

Figure 4-31: Opening angle parameter analysis (images). These images demonstrate that the ellipticity of the jets is controlled by the opening angle. The first image is a single jet that has been created with an opening angle of 10°. The opening angle of the jet in the second image is 100°. The second jet is strongly circularized through widening the opening angle. This figure was created with a jet located at 13°N (corresponding to active area 2) and is valid for the April geometry.

4.3.10 Strength of the Jets and Solar Insolation

The individual jets are given a 'strength' corresponding to its strength relative to the other jets assuming all jets experience the same solar insolation. However, the strength does not translate directly to the total production of each jet. In April, for instance, the jets at the lower latitudes are not exposed to as much sunlight as those at high latitudes. Therefore, they require a much higher strength to attain the same production rate as the active area near the pole. Both strength and relative production rates are listed in Table 4-5.

4.4 Results

Through an analysis of the jets, I am able to constrain the expansion velocity of the coma and the locations of the active areas on the surface. The locations and strengths of the CN and C_2 active areas are the same; however, one active area that is producing the bulk of the OH jet morphology is severely depleted in CN and C_2 compared with the other OH active areas. Three possible sources of the gas jets are discussed including icy grains, a nuclear gas source, and CHON grains. The radial profiles and morphology of the jets support a CHON grain extended source and allow an estimate of the fraction of radicals that originate from the nucleus versus the extended source for each species.

4.4.1 Expansion Velocities and Jet Widths

The projected expansion velocities of the gases increase with distance. For the March data, the advancement of an individual jet through a time sequence of images was used to calculate expansion velocity. The radial profiles are used in conjunction with the processed images to determine where the jets begin, peak, and fade to the point that they can no longer be discerned from the isotropic component. Gaussian profiles are fit to each jet to determine its location. The distance that a particular jet moves from one image to the next, combined with both the time elapsed between images and the comet's rotation, is used to calculate the expansion velocity of the jets.

Projected expansion velocities extracted from the March data show that near the very inner coma (within $\approx 35,000$ km), the gas jets are expanding at rates of 0.2 to 0.5 km/s. By the time the gas jets have reached distances of 80,000 km from the nucleus, they are moving at rates of 2 to 2.3 km/s. In contrast, the dust jets are moving at rates near 0.1 km/s in the inner coma and reach 0.5 km/s at the farthest distances that they can be seen (50,000 km) (Table 4-3). These results are consistent

with those found by Lisse et al. (1997) who followed the shells evident in thermal infrared images taken in April, 1997. They found a dust projected expansion velocity of 0.4 km/s, and an actual expansion velocity (after they accounted for projection effects) of 0.6 km/s.

Table 4-3: Projected expansion velocities.

Species	March [km/s]	April [km/s]
OH (inner coma)	0.1 to 0.5	0.4
OH (outer coma)	1.2 to 2.3	1.3 to 2.1
C_2 (inner coma)	0.2	0.5
C_2 (outer coma)	1.8	1.5 to 1.8
CN (inner coma)	0.2	0.5
CN (outer coma)	1.8 to 2.1	1.8
Dust (inner coma)	0.1	0.3
Dust (middle coma)	0.5	0.4

Note: The projected expansion velocities of dust and gas jets are tabulated for March and April, 1997. The inner coma refers to within ~35,000 km from the nucleus, and the outer coma refers to maximum distances of 85,000 km from the nucleus in March and 100,000 km in April. Velocity for the dust is listed as 'middle coma' due to the limited projected distances that dust jets are observed (<50,000 km) Errors are roughly ±10% in all cases. The low value in each range of values corresponds to velocities when the jets were somewhat closer, and the higher values when the jets were somewhat farther away.

Similar results are found through an analysis of the April data. Two methods were used to calculate the expansion velocity for this month. The first assumes that the innermost jet becomes the second farthest jet exactly one rotational period later, and becomes the farthest jet after an additional rotational period (a valid assumption based on changes observed between April 22 and 26). The second uses the method of Klavetter and A'Hearn (1992). The image is first unwrapped into (r,θ) space (Fig. 4-32). The location of the peak of the jet with respect to the central condensation is then plotted as a function of θ, and the expansion velocity is calculated by translating θ into time using the known rotation rate of the comet (Fig. 4-33; see Section 2.3 for further details). The resultant expansion velocities of the gas jets were found to be

0.4 to 0.5 km/s in the inner coma (within 40,000 km of the nucleus), and 1.7 to 2.1 km/s near the outer coma (85 to 100,000 km from the nucleus). Again, the dust jets were much slower, averaging 0.3 km/s.

The April gas jet models were used to determine the actual (unprojected) expansion velocities (as opposed to the 2-dimensional projected expansion velocities). Actual velocities reached values of 2.3 km/s in the outer coma. This is consistent with OH expansion velocities of 2.2 km/s reported by Colom et al. (1997) when Comet Hale-Bopp was at 0.93 AU. They analyzed radio observations of OH line profiles in conjunction with models.

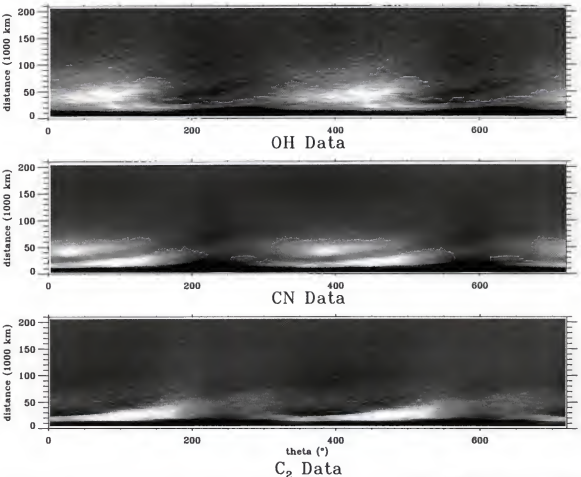

Figure 4-32: OH, CN, and C_2 images in (r,θ) space. April 26, 1997: Each image is unwrapped into (r,θ) space and concatenated with itself to yield an image that is a full 720°. This aids the eye in following each jet as it progresses away from the nucleus.

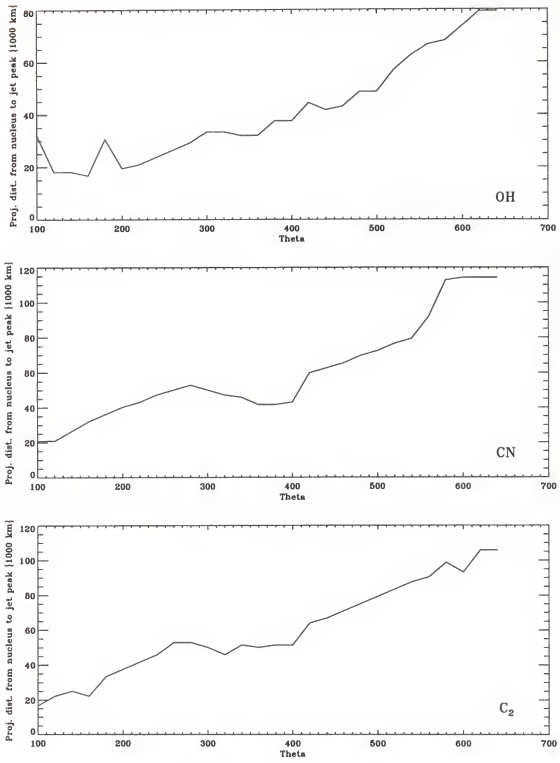

Figure 4-33: Radial profiles used to calculate expansion velocity. The radial profiles correspond to the locations of the jet peaks in the images displayed in Figure 4-32. Theta is translated to time through Comet Hale-Bopp's known rotational period. The slope of the line then yields the expansion velocity in the coma. Comet Hale-Bopp's rotational period is ~11.3 hours (see Section 2.3).

Table 4-4: Projected jet widths.

Species	April Data [km]	April Model [km]
OH (inner coma)	13 to 20,000	15 to 20,000
OH (middle coma)	25 to 40,000	25 to 40,000
OH (outer coma)	50 to 65,000	50 to 60,000
C_2 (inner coma)	12 to 28,000	13 to 23,000
C_2 (middle coma)	30 to 60,000	38 to 62,000
CN (inner coma)	10 to 27,000	13 to 25,000
CN (middle coma)	22 to 35,000	21 to 35,000
CN (outer coma)	40 to 70,000	35 to 70,000
Dust (inner coma)	8 to 12,000	–
Dust (middle coma)	8 to 12,000	–

Note: Widths of dust and gas jets in the April 26, 1997 data and models. The inner coma refers to within 35,000 km, the middle coma to within 65 to 70,00 km, and the outer coma to within 100,000 km from the nucleus. The ranges listed signify the range of jet sizes measures within the coma. Errors are roughly ±5 to 10% in all cases. Only inner and middle coma are listed for C_2 and dust due to the limited extent of the jets. No value is listed for dust jet models because the dust jets were not modeled.

The gas jets are twice as thick as the dust jets and the projected expansion velocity of the gas $\approx 2v_{dust}$ (Fig. 4-8, Tables 4-3, 4-4). This implies that the optically reflecting dust and gas are not totally coupled at the distances the jets are observed. However, continued acceleration of the dust and gas suggests that they are not entirely uncoupled either.

4.4.2 Projected Locations of Active Areas on the Nucleus

The smooth spiral apparent in the April gas jets suggests that one active area is primarily responsible for the spiral morphology. The modeling indicates that several sources are required to generate the morphology we see for all three gas species.

VC99 report that three active areas are required to model the dust jets in their April 10 and May 2, 1997 images. The morphology observed in my OH, CN, and C_2 images can be reproduced by invoking five active regions on the nucleus. Similar to VC99, my models require two to three active areas located near the comet's equator

(two of the active areas creating OH could be a single elongated area), and one at a high latitude. The region located at the high northern latitude (60°N; active area 1), is physically much smaller than the near equatorial active areas. Unlike VC99, my models require an additional active area at a very low latitude (22°S; active area 4). The production from this region may not be strong enough to lift relatively large (optically scattering) dust particles from the surface, but appears to lift sub-micron grains in the gas flow. This would explain why VC99 did not invoke a source at this latitude to reproduce their dust jets, which contain the larger, optically scattering dust particles.

Emphasis was placed on reproducing the OH jets because jets in this species had never been observed without a dust jet counterpart. Furthermore, the main molecular parent of OH is known (H_2O) and characterized better than the molecular parents of either CN or C_2. Precedence was also given to the April images for two reasons. First, the Sun is located at a high cometocentric latitude in April, which dictates that the active areas below $\sim 20°$S latitude are never exposed to the Sun; this limits the number of active areas that must be included in the model and therefore the uniqueness of the model is better constrained. Second, the scientific questions that I posed can be answered through modeling the April data alone. I note that the morphology of the March jets, while not exactly reproduced, is consistent with models generated simply by leaving the jets at the locations determined by the April data and translating to the March geometry (position angle of the Sun and phase angle). Additional active areas are required to fully reproduce the March morphology.

To recreate the April coma jets, the cometocentric locations of the active areas in each species do not precisely coincide, but are close. The morphology of the CN and OH data is more difficult to recreate than the C_2 morphology, and thus the locations of their active areas are better constrained than the areas producing C_2. All four active areas necessary to reproduce the CN morphology can also reproduce

the C_2 morphology. The OH jets are reproduced only when an additional active area is invoked (five total). The additional (5th) active region is located at 12°S latitude and is responsible for almost half of the grain-source OH.

Table 4-5: Locations of model active areas.

Species	Lat (°) [± 5]	Long (°) [± 10]	Opening angle (°) [± 10]	Rel. strength [± 20%]	Q (%) [± 5%]
OH (A. Area 1)	60	175	20	1.0	9
OH (A. Area 2)	20	240	40	3.0	22
OH (A. Area 3)	15	120	60	1.2	8
OH (A. Area 4)	-22	225	60	5.3	17
OH (A. Area 5)	-12	120	120	10.0	44
CN (A. Area 1)	60	175	40	1.0	16
CN (A. Area 2)	13	240	40	4.0	43
CN (A. Area 3)	15	120	60	1.3	16
CN (A. Area 4)	-22	225	40	4.0	25
C_2 (A. Area 1)	60	175	50	1.0	16
C_2 (A. Area 2)	13	240	60	4.0	43
C_2 (A. Area 3)	15	120	90	1.3	16
C_2 (A. Area 4)	-22	225	90	4.0	25

Note: The parameters listed create the best fits to the morphology and radial profiles. The parameters include the latitude and longitude of the center of the active area, the opening angle, the relative strength of the active area compared with the other jets (relative strength denotes the number of particles one active area would produce compared to the other regions producing that species if all active areas were equally illuminated), and the contribution (%) that each individual active region makes to the total production rate of radicals by grains (Q).

The effects caused by each of the active areas are visible on the computer screen; in hardcopy prints, however, it is especially difficult to see how active areas 3 and 4 contribute to the morphology since they contribute a small portion of the total signal. For OH and C_2, the contribution from active area 3 overlaps jets created by other active areas. This region produces 8% of the jet-source OH (less than 5% of the total OH signal) and 16% of the C_2 jet-source signal (less than 10% of the total C_2 signal). However, an equivalent amount of OH and C_2 are produced by active area 1, which can be detected in the images because the morphology created by this

active area is more confined spatially. The addition of certain active areas, such as the fifth OH-producing active area, is required to slightly alter the precise locations of the peaks and the troughs of the jets by as few as 10 to 15,000 km. This effect can also be difficult to discern in the printed copies.

Figure 4-34 shows how each individual active area contributes to the CN morphology. Active area 1 is needed to increase the contrast of both the middle jet (50,000 km from the nucleus) and outermost diffuse jet between position angles of $\approx$ 260 to 290°. Active area 2 contributes nearly half of the jet-source CN and contributes to both the sunward and anti-sunward jets. It is responsible for a portion (between position angles of 0 to 60°) of both the inner and outer anti-sunward jets (upper left quadrant). It also aids in re-creating the correct brightness contrast in the inner and outer sunward jets (PA=180 to 300°). Active area 3 fills in the trough (40 to 50,000 km from the nucleus) between the inner and middle jets at position angles of 90 to 180°; the change in morphology is subtle when viewed on the computer screen, and therefore is very difficult to see in hardcopy images. Active area 4 brightens and extends the inner jet in the lower left quadrant to 40,000 km (PA = 70 to 120°), and aids in circularizing the jet morphology.

In the C_2 images (Fig. 4-35), active area 1 contributes to the jet between position angles of $\approx$260 to 290°; without this active area, the jet is not circular enough in the upper right quadrant. Nearly half of the jet-source C_2 is created by active area 2; it contributes to both the sunward and anti-sunward jet morphology and extends the outer edge of the jet from position angles of 180 to 360°. The contribution from active area 3 overlaps portions of the jet created by the other active areas between position angles of 90 to 180°; the contrast is altered only slightly, and the effects cannot be seen in the hardcopy images. One could argue that the activity in this region is unnecessary to recreate the morphology of C_2; however, it is necessary to reproduce the CN jets. Therefore, this region was included to determine

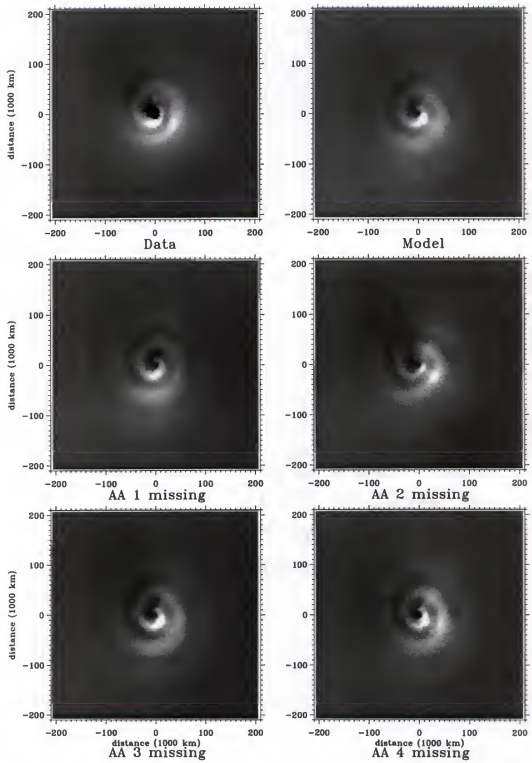

Figure 4-34: CN active area parameter analysis (images). April 26, 1997: CN data and the best fit Monte Carlo model are shown at the top. The remaining images are the Monte Carlo model with each active area turned off to show how each area contributes to the morphology of the jets.

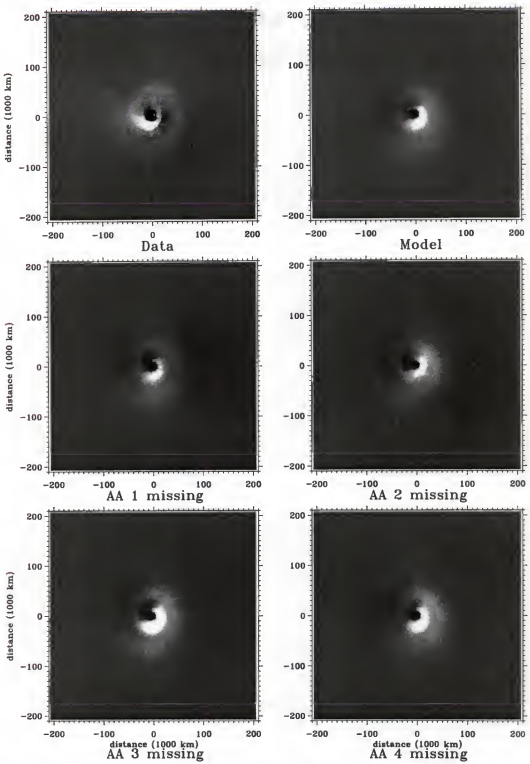

Figure 4-35: C_2 active area parameter analysis (images). Same as Figure 4-34, except for C_2. The morphology is difficult to see in the hardcopy versions, but can be seen on the computer screen. The morphology differences caused by eliminating the active area 3 source is particularly difficult to see, even when viewed on a computer screen.

the consistency between the locations of the CN and C_2 active regions. Active area 4 rounds out the innermost jet from PA = 80 to 120° within 45,000 km; the contrast change is very subtle as viewed on the computer screen, and is difficult to see in the hardcopy images. Because the C_2 morphology does not extend as far from the nucleus, the effects of the jets are more difficult to see than the other two species.

The locations and strengths of the active regions creating the CN and C_2 jets are the same, yet the morphology differs. Other parameters are responsible for these differences. The opening angles of the active areas are larger for C_2, creating a more circular and somewhat more diffuse spiral. The daughter velocity is also larger, creating a similar effect. The daughter lifetime of C_2 is shorter than CN, which explains why the contrast of the C_2 jets is not as high as they move farther from the nucleus. However, while the locations of the jet peaks and the widths created by the C_2 models match the C_2 data, the data jets appear to be somewhat more diffuse than the modeled jets. This could be explained if C_2 is a granddaughter product as opposed to being emitted directly from the CHON grains. My models are not set up to reproduce this breakdown, so I cannot test this theory. However, this scenario is plausible since a number of parent gases (e.g. C_3, C_2H_2) could be produced directly from the CHON grains, and the C_2 could be emitted from the parent gases. All these factors play a role in creating the differences between the morphology of the C_2 and CN jets.

In the OH images (Fig. 4-36), active area 1 brightens the portion of the middle and outer jet between position angles of 225 to 300°. Without this active region, the middle jet appears too wide and too dim, and the outermost jet is too dim. Within the errors (±5°), active area 2 creating OH (at (20, 240)) is likely the same region on the nucleus as the CN and C_2 active area 2 (at (13,240)). This region creates the bulk of the OH morphology. It is responsible for the innermost portion of the anti-sunward jet, within 40,000 km and between position angles of 0 to 90°. It also

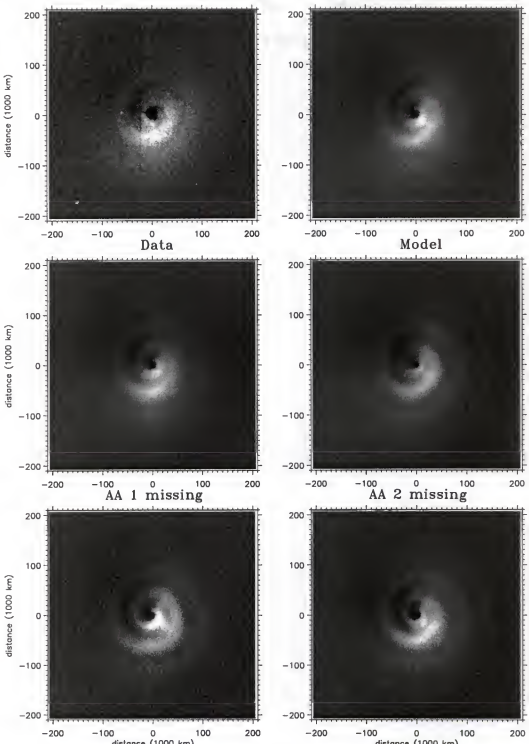

Figure 4-36: OH active area parameter analysis (images). Same as Figure 4-34 for OH. An image demonstrating how the model looks when active area 3 is missing is not shown because this region does not visibly contribute to the comet's morphology. Instead, an image representing the Monte Carlo model with A. Area 5 missing is included in its place.

contributes to signal in the outermost jet between position angles of 270 and 360°, though this may be difficult to see in the printed versions. Similar to C_2, active area 3 does not contribute to the morphology of the OH jets; thus an image with active area 3 missing is not included in Figure 4-36. This region is included strictly to verify that the same mixture of OH:C_2:CN can be emitted from all four active areas that are required to reproduce the CN morphology. Active area 4 is responsible for the additional rounded nature of the spiral at a position angle of 80 to 120°, within ~30,000 km of the nucleus. For consistency with Figures 4-34 and 4-35, the 'A. Area 4 missing' image is in the lower right corner for OH (Fig. 4-36), and 'A. Area 5 missing' image (discussed below) is placed in the lower left corner of the montage.

The latitude of the remaining OH region, active area 5, differs significantly from those of the carbon species. It is located at 12°S latitude and no appreciable amount of CN or C_2 can be emitted from this region without negatively altering the morphology of the carbon species jets. This additional active area creates the bulk of the morphology differences between OH and the carbon species. Without this active area, the jet in the sunward direction extends ~10,000 km farther from the nucleus than the jet in the data or the best-fit Monte Carlo model. Omitting this active area also results in a much larger trough 30 to 35,000 km from the nucleus (between position angles of 180 to 300°). The addition of this active area also decreases the contrast of the anti-sunward jets so that they appear thinner than the CN anti-sunward jets and do not extend as far from the nucleus (though this may be difficult to see).

This analysis indicates that the grains in three of the active regions contain the same mixture of OH:C_2:CN, and one (active area 3) is indeterminate but may contain the same mixture. The relative strengths suggest that active areas 2 and 4 are physically larger than areas 1 and 3. Comparing the relative strengths of the OH active areas with one another implies that a very large additional area (active area

5) in the southern hemisphere exists which is depleted in the two carbon species. This suggests that although Comet Hale-Bopp appears to be a fairly homogeneous mixture, pockets of heterogeneity may exist in the nucleus.

4.4.3 Jet Source: Gas vs Grain

It is important to determine whether the jets originate from a gas or grain source (whether icy grains, CHON grains, or silicate dust grains[2]) before one can characterize the composition of both the ices that are sublimating directly from the nucleus and the CHON grains and silicate dust that are entrained in the sublimating gases. Icy grains have been invoked as a source of gas for both Comets Bowell and Hyakutake. Icy grains were detected in the former comet by Campins et al. (1983) and in the latter comet by Harris et al. (1997). Two other sources of gas jets have been proposed and modeled by Combi (1987) and Klavetter and A'Hearn (1994). Combi's model suggested that an initially confined jet of a parent gas expanding radially away from the nucleus could be sustained by the daughter radicals. Alternatively, a sub-micron "CHON" grain extended source was proposed for the CN and C_2 jets observed in Comet Halley (A'Hearn et al. 1986a, b, Schulz and A'Hearn 1995) and was not ruled out by Combi (1987). Klavetter and A'Hearn demonstrated that the radial profile extracted from CN images was best fit using a diffuse gas source plus a CHON grain extended source. All three possibilities are considered here. I conclude that a sub-micron CHON grain extended source, combined with a diffuse gas source, can best explain the Comet Hale-Bopp observations.

Icy grains

If icy grains were an extended source of OH, it could affect the radial brightness profile and morphology, but the translation from OH production rates to H_2O production rates would not be in error. Furthermore, they would help explain why

[2]all references to grains mean CHON grains unless specifically described as 'icy grains' or 'dust grains', where the latter are silicate dust grains.

such a large fraction of the composition of the extended source (based on the total production rates of each species, see below) is OH compared with CN and C_2.

Ice mantled grains were invoked as a source of OH in Comet Bowell when it was beyond 3 AU from the Sun (A'Hearn et al. 1984). Likewise, Harris et al. (1997) conclude that an extended region of icy grains surrounded the nucleus of Comet Hyakutake and was responsible for two arc-shaped features that trailed the nucleus by 1200 km and 200 km, respectively. They suggest that the icy grains are responsible for a volatile production rate of 23% of the nucleus. This is consistent with the estimate of OH originating from an extended source in the Comet Hale-Bopp images investigated here. However, Harris et al. note that the icy grains ejected while a comet is at 1 AU (the distance of Comet Hale-Bopp at perihelion) would likely sublimate completely within a few hundred kilometers.

For the triangular extended source that explains the Comet Hale-Bopp images, the parents must survive for a maximum lifetime of approximately 6 to 8×10^4 s. Hanner (1981) studied icy grains and predicts that at 1 AU, the lifetime of pure ice grains of radius 1.0 μm would be roughly 4×10^3 s, while the lifetime of a 5 μm icy grain would be $\sim 10^7$ s. Icy grains that are not composed of pure ice must be much larger – 1 mm – to attain a lifetime of 2×10^4 s. One millimeter grains cannot be accelerated to speeds near the gas expansion velocity and, therefore, cannot be the source of the observed gas jets (Combi et al. 1997). Icy grains of the former size would scatter visible light and travel at speeds coincident with the dust grains that scatter visible light; therefore, we would observe gas jets whose expansion velocity was coincident with the dust jets we observed, which is not the case. This is a strong argument against icy grains being the triangular extended source. However, while this rules out icy grains as the source of the gas jets, they were detected in the inner coma of Comet Hale-Bopp ($< 11,000$ km) following an outburst when the comet was at 2.5 AU (Campins et al. 2000).

One might wonder whether the high production rates of Comet Hale-Bopp would produce an environment that is optically thick and thereby might shield the icy grains in the inner coma. Perhaps this could act to extend the lifetimes of the pure-ice grains that are small enough to be accelerated to speeds near that of the gas and delay the peak of the gas production from the icy grains. Due to high production rates, the very inner coma of Comet Hale-Bopp is not optically thin to all photons, and in particular was probably optically thick to photons that photodissociate water. However, photons of $\lambda < 1860$ Å, which break down water to form H and OH, are only effectively shut off to distances of 600 km from the nucleus (Combi et al. 1997). This is not sufficient to extend the lifetime of icy grains appreciably, nor to delay the peak production of the icy grains by 3 to 4×10^4 s. Furthermore, the inner coma is optically thin to most wavelengths; thus water will begin to sublimate from the icy grains immediately upon ejection from the nucleus even though it will not photodissociate into OH until it reaches a distance of at least 600 km from the nucleus. Therefore, this is not a solution.

To confirm the above arguments suggesting that icy grains cannot reproduce the observed OH jets and radial profiles, I generated models that employ icy grains as the source of the jets. The production from icy grains peaks at the nucleus, but the behavior of the decreasing production with distance from the nucleus is dictated by the shrinking surface area of the icy grain (i.e., the production falls off less steeply than the exponential drop off experienced by molecules that photodissociate). The results were somewhat similar to a nuclear gas source, and did not fit the data. Even when only active area 5 (at 12°S latitude) generated icy grains and the remaining active areas produced OH from CHON grains, the radial profile were grossly incorrect and the morphology did not match as closely as the model whose jets were strictly produced by CHON grains (Fig. 4-37). Unless a mechanism is found that would delay the peak production from icy grains to distances of 3 to 4×10^4 km from the

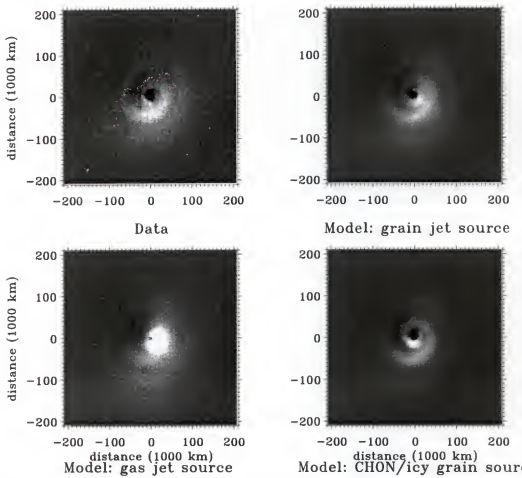

Figure 4-37: OH data and models with gas, CHON grain, and icy grain source jets. April 26, 1997: a) OH data, b) OH model with an extended CHON grain jet source + diffuse molecular gas source, c) OH model with a nuclear gas jet source, and d) OH model that employs an extended CHON grain source for all active areas except at 12°S latitude (active area 5), which is produced via icy grains. The morphology produced in (d) is matches the data somewhat more closely than the gas jet source, however, it does not fit the data as well as the model with all jets created by an extended CHON grain source.

nucleus and extend the lifetimes of sub-micron icy grains, icy grains cannot be a major source of the OH gas jet morphology observed.

Nuclear gas source

Combi (1987) suggested that an initially confined parent jet expanding radially from the nucleus could be sustained by the daughter radicals. He asserts that the daughters would roughly continue in a preferential direction and could account for the asymmetries (half cone angle of 45°) observed. However, he noted that photo-sputtering of the observed radicals from CHON particles could also be the mechanism by which the jets are created. He cited arguments both for and against each source and in the end, Combi could not determine whether a gas or CHON grain source was responsible for the jets in Comet Halley.

To test a nuclear gas source, the parent should be identified to determine the parent lifetime used in the model. Water is the dominant gas source of OH. Significant contributions of OH from gas sources other than water are unlikely. More complex molecular parents recently detected (such as methanol, CH_3OH) contribute such a small fraction of the total composition of a comet (1 to 7% relative to water; Crovisier and Encrenaz 2000), that their contribution to the total OH produced can be neglected. Furthermore, radicals produced by any molecule originating in the nucleus would display a behavior similar to that of a water gas source (i.e., peaked at the nucleus with an exponential decay). Astronomers are not certain of what the gas parent(s) is/are for either the CN or C_2 radicals. HCN is the most likely candidate for CN; C_3 and C_2H_2 may be sources of C_2. Parent lifetimes for each of these possible candidates were tested.

Regardless of which parent molecule might produce the radicals observed for any species, the radial profile of a nuclear gas source peaks at the nucleus and the parent and daughter will exponentially decay. *Both the radial profile and morphology of all species suggest that a nuclear gas source, whether partially or wholly emitted*

from a confined region on the nucleus and with or without collisions, cannot recreate the radial profile (Fig. 4-14) or morphology of any gas species (Figs. 4-11, 4-12, and 4-13).

CHON grain extended source

CHON grains were invoked as a source for Comet Halley's CN and C_2 jets by A'Hearn et al. (1986a, b). They reasoned that CHON grains might give the radicals the ability to retain their identity as jets well beyond the collisional zone. Recall that because gases expand adiabatically from the nucleus, they were expected to become isotropic at distances much closer than the distances the jets were observed; a grain extended source would resolve this issue since grains do not expand adiabatically.

While we understand the mechanism by which a gas source creates a radical (photodissociation of a parent gas), the mechanism responsible for the production of radicals from CHON grains is not known. Two possibilities have been discussed by Combi (1987), and a third by Lamy and Perrin (1988): (1) Vaporization of the grains, (2) photosputtering of the radicals directly from the surface of the grains and (3) thermal dissociation of very hot grains which emit the radicals directly from their surface.

If the grains vaporize, then one would expect that more stable parent molecules would be released from the CHON grains and not the less stable observed radicals. Depending on how complex the molecules are that might vaporize from the grains, the observed radicals could be daughters, granddaughters, or even great granddaughters. With each additional photodissociation necessary for the production of the observed radicals, the jets become less defined for two reasons. First, the velocity dispersion increases from the excess energy of each dissociation. Second, the molecule's direction of motion changes since daughters are ejected isotropically in the parent's rest frame. While collisions in Comet Hale-Bopp's coma might act to reduce the diffusion of radicals that are granddaughter or great-granddaughter product, collisions were

too infrequent at distances where jets were observed in Comet Halley for grain vaporization to be a favored explanation. Thus, grain vaporization might serve to explain Comet Hale-Bopp's jets, but finding a mechanism that is applicable to both comets is preferred.

Combi suggested photosputtering as an alternate mechanism to explain Halley's jets. With photosputtering, a UV photon impacts individual molecules incorporated in the CHON grain, and the radical observed is ejected directly from the surface of the grain. This mechanism has also been proposed as a means of eroding ices from particles in Saturn's rings (Carlson 1980). Assuming the CHON grain halo is equivalent to the distance that the jets are observed, $\sim 8 \times 10^4$ km for Comet Halley, Combi states that the average lifetime of a particle must be of the order 10^5 s. Combi then argues that the lifetimes of even the smallest CHON grains observed in Comet Halley's coma would be an order of magnitude larger (i.e., the gas jets would be observed at distances much greater than $\sim 8 \times 10^4$ km); he concludes that this argument does not support a CHON grain source for Halley's gas jets.

This point has been resolved with the findings of Lamy and Perrin (1988). Assuming that the CHON grains thermally dissociate (instead of releasing radicals through photosputtering), they show that the lifetime of a 0.2 μm grain would be approximately 10^5 s. Lamy and Perrin (1988) also show that small grains (< 0.5 μm) do not absorb UV photons efficiently, but are even poorer at emitting infrared energy. As a result, they are very hot: 450 to 500 K at 1 AU. At this temperature, the grains will likely thermally dissociate directly into the radicals observed while grains of a larger size are cooler and therefore do not thermally dissociate. In addition, the evaporative cooling rate is much smaller than the radiative cooling rate so that the temperature of the grains is unaffected by the thermal dissociation of molecules from the grains. Finally, based on the grain size distribution in Halley, Lamy and Perrin estimate that hot grains smaller than 0.5 μm will contribute less than 10% of the

total scattered light. Thus, the sub-micron grains could produce gas jets, while at the same time, remain undetected in the continuum images.

Combi and Fink (1997) modeled a source function that they suggest would represent a slow speed thermal dissociation of gas from CHON grains. This grain source behaves such that, compared with a nuclear gas source, it produces fewer radicals very close and very far from the nucleus, and more at intermediate locations. Instead of an exponentially decreasing distribution, the emission rate from the CHON grain surface and the surface area exposed to solar insolation are both proportional to the square of the grain radius. The probability of emission is $P = (1 - t_G/\tau_H)^2$ where t_G is the time when the CHON grain is emitted, and τ_H is the grain lifetime, roughly 2×10^5 s. However, the total production from CHON grains still peaks at the nucleus. The models I generated that employed this source did not match the data (Fig. 4-38).

In summary, I was unable to fit the radial profiles of OH, CN, or C_2 with (1) an icy grain source, (2) a nuclear gas source or, (3) a CHON source whose production peaks at the nucleus rather than at some distance away.

A partial contribution from a triangular CHON grain extended source, that does not peak at the nucleus, CAN reproduce the morphology of observed jets in all three species. A triangular extended source function is consistent with a hot sub-micron CHON grain source because it takes time for the grains to warm up after they are released from the nucleus. The jets are best fit with an extended source whose production peaks 3 to 4×10^4 s after release from the nucleus. However, the triangular CHON grain source alone cannot reproduce the radial profile and, therefore, the grains are not solely responsible for the radicals detected. Both the morphology and radial profile are reproduced only when an extended source is combined with a diffuse (isotropic) nuclear gas source (Figs. 4-39, 4-40, and 4-41).

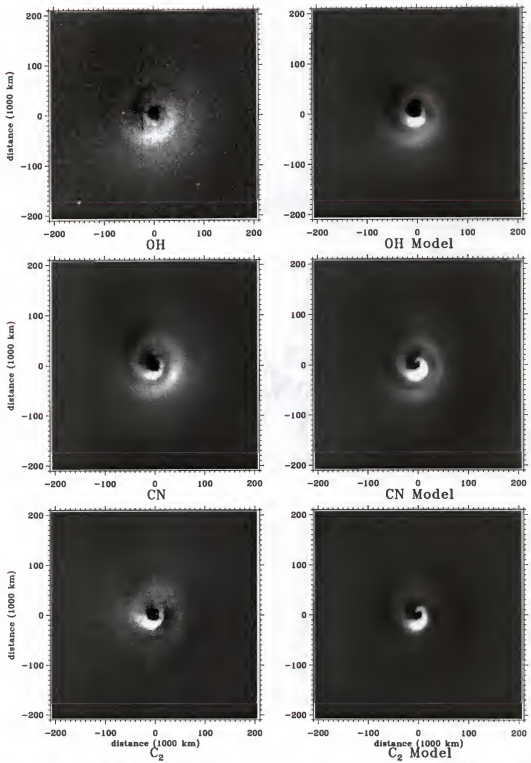

Figure 4-38: Data and models with nucleus-peaked CHON source. The images on the left are OH, CN, and C_2 data. On the right are the corresponding model with a nucleus-peaked CHON grain model, which do not fit the data well.

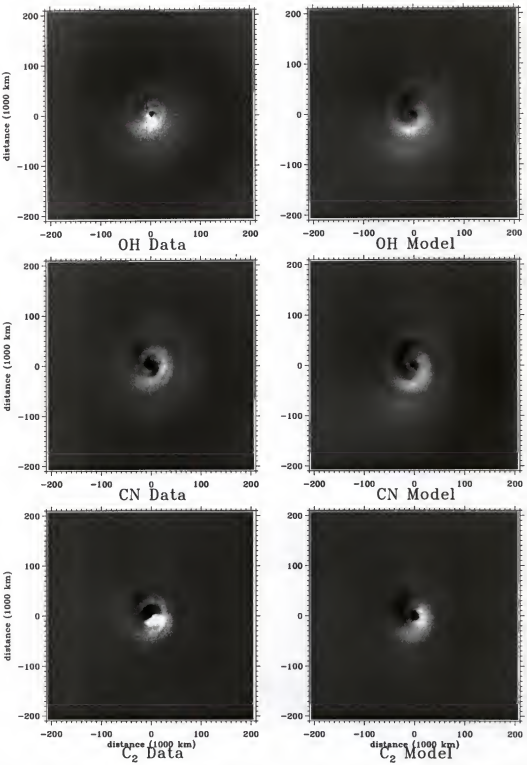

Figure 4-39: Data and models with triangular CHON grain source (April 22, 1997). April 22, 1997: The images on the left are OH, CN, and C_2 data. The images on the right are the Monte Carlo models that best reproduce the data for each species. The jets originate from an extended (CHON grain) source. A diffuse (isotropic) gas source model must be combined with the jet model to reproduce both the morphology seen here as well as the radial profiles.

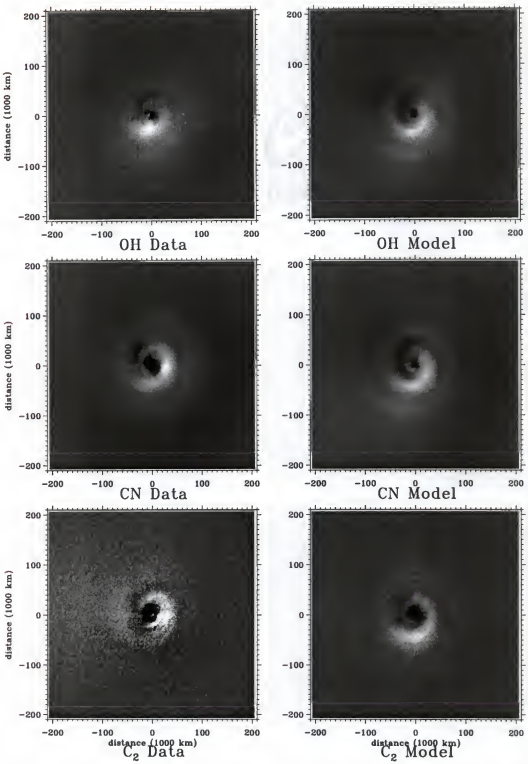

Figure 4-40: Data and models with triangular CHON grain source (April 23, 1997). Same as Figure 4-39, but for April 23, 1997.

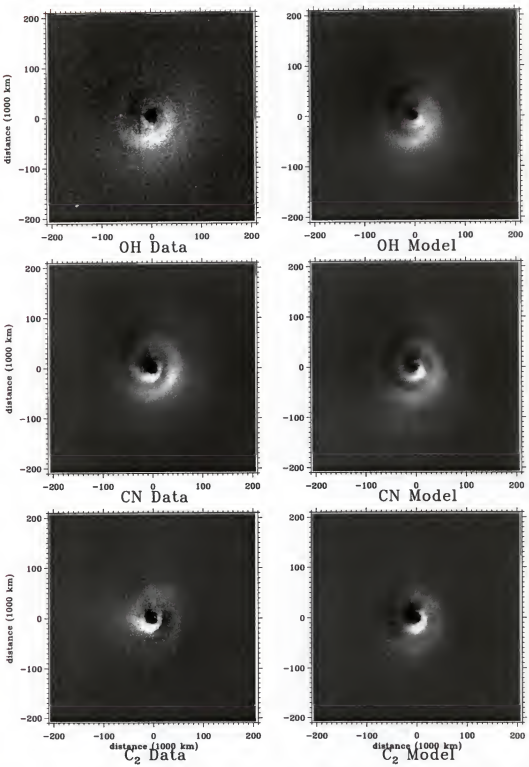

Figure 4-41: Data and models with triangular CHON grain source (April 26, 1997). Same as Figure 4-39, but for April 26, 1997.

The CHON grains, which do not scatter much light at visible wavelengths, must be either abundant and very small (< 0.2 μm) or less abundant and very large (< 100 μm). If the grains were very large, they would not be accelerated to velocities twice those of the dust in the jets seen in the continuum images. Thus, very small grains are favored. Thermal infrared images of Comet Hale-Bopp indicate that a significant number of very small hot grains existed in Comet Hale-Bopp's coma (Lisse et al. 1997). These grains could be the grain source responsible for the gas jets observed.

Nuclear and extended sources: contributions to the coma

In addition to creating the jet morphology, the extended source is responsible for creating a significant portion of the isotropic component of Comet Hale-Bopp's coma. Comparing the radial profile of the data with the radial profile created by the models, I can estimate the fraction of the gas created by an extended source compared with a diffuse nuclear molecular gas source. 'Diffuse source' here means the gas that originates from ices sublimating from the nucleus. Using the Monte Carlo model, I am able to compare the total production rates of the gas and grain components separately. This indicates that 35 to 45% of the OH, 50 to 60% of the C_2, and 65 to 75% of the CN originates from an extended source. The ranges listed for each species are due to the errors associated with the model input parameters, and variations from one day to the next. These fractions are consistent with estimates of CO (roughly 50%) originating in an extended source in Comet Hale-Bopp, when the comet was within 1.5 AU (DiSanti et al. 1999). The balance of the radicals originates from a nuclear gas source that is either emitted isotropically from the nucleus or becomes isotropic very quickly upon ejection from the active areas on the nucleus. Otherwise, the radicals from this source alter the morphology of the jets in a detrimental way.

A'Hearn et al. (1992) concludes that most CN, some C_2, and no NH form from grains in the coma of Comet Halley compared with the gas that is created by

molecules released directly from the nucleus. Klavetter and A'Hearn (1994) estimate that 40 to 60% of the total CN emission in the coma of Comet Halley is due to the CN jets and the total contribution from jets increases as the number of jets increases. Here 40% is estimated for two jets and 60% if three jets are present. Thus, 65 to 75% of the CN originating from 4 active areas on Comet Hale-Bopp is consistent with extended source vs. molecular source estimates found for Comet Halley.

Lamy and Perrin (1988) estimate that a 0.2 μm grain will produce $\sim 3.5 \times 10^4$ molecules/s. Therefore, a relatively small number of grains, compared with molecules from a nuclear gas source, are needed to generate a significant contribution to the gas coma. However, we do not know what the composition of grains is, so studies such as this one yield the most direct estimate of the OH:C_2:CN proportions in the extended source (see Section 4.5.2).

4.5 Discussion

In this section, the differences in the sunward and anti-sunward jets are discussed. The bulk of the anti-sunward gas jets are not emitted at night, but rather originate from the active areas when they are closer to twilight and the production rates are lower. This suggests that the morphology of the gas jets is different from the dust jets because a higher production rate is required to drag the larger dust grains (that reflect visible light) from the surface than the sub-micron CHON grain extended source (that is responsible for the gas jet morphology). The extended source is shown to cause discrepancies in production rates calculated by a Haser model. Finally, the composition of the nuclear and extended sources are compared and implications pointing toward a heterogeneous nucleus are discussed.

4.5.1 Morphology

The brightness of the gas jets in the anti-sunward direction is lower than in the sunward direction; the sunward jets are roughly 10 to 15% brighter for CN and C_2,

and roughly 60 to 70% brighter for OH. Perhaps this difference is smaller than what one would expect given that dust jets are observed only in the sunward direction.

Several factors might be at work here. Without determining the locations of the jets, one would not know whether the anti-sunward jets are actually a result of active areas that remain active during the night (i.e., when the solar insolation is zero), or if they are a result of active regions moving into twilight. It has been suggested that a thermal lag is partially responsible for the anti-sunward production of radicals. If portions of the nuclear surface have a high thermal inertia, one may have a warm active source, even after this source has rotated into the night side of the nucleus. However, a high thermal inertia does not need to be invoked for Comet Hale-Bopp. The best fit morphology is created when the comet is allowed to continue producing radicals (though at a much lower rate) only 30° past sunset. A much higher thermal inertia would cause the comet to produce radicals much longer, and perhaps all night.

Instead, the slightly decreased brightness of the jets in the anti-sunward direction can be explained by the geometry of the nuclear insolation. To demonstrate this, recall that the comet's pole is only 20° away from pointing directly at the Sun. The production rates of the near equatorial jets (those between 12°S and 20°N latitude), which are responsible for the majority of the spiral morphology, will be modulated by the solar incidence angle. The comet produces more gas and dust when the jets are pointed in the sunward direction, but the position of the Sun in April (Fig. 4-28) prohibits the lower latitude jets from ever experiencing a very high intensity of sunlight. While 'noon' for these jets means a higher production rate, difference between their relative noon production versus twilight production will not be very large because the axis of the comet is pointing nearly toward the Sun. Therefore, one should expect a slight difference in brightness in the directions that correspond to noon and twilight for these jets (i.e., sunward and anti-sunward), but not as great a difference as if the

rotation axis was perpendicular to the direction of the Sun. This may also explain why there is a greater brightness difference between the sunward and anti-sunward jets evident in March, when the comet's rotational pole is pointing 50° away from the Sun.

Finally, the existence of anti-sunward gas jets with no coincident dust jets might be a result of the following: the bulk of the morphology of the gas jets are produced by jets near the equator. The southern latitude jets, in particular, are always near twilight where the Sun's intensity is lower, and therefore the production rates per surface area from these areas will be lower than higher latitude jets. The gas production from the southern latitude sources may be low enough that the smaller CHON grains can be lifted from the surface, but the larger, optically scattering grains (that we see as dust jets) cannot be lifted. Recall that the CHON grains must be small enough that they do not scatter much at visible wavelengths.

To fully recreate the sunward/anti-sunward brightness asymmetry, one must account for the geometry of the Sun-comet-Earth locations (phase angle and the position angle of the Sun). Lambert's Law must also be applied. These parameters, along with the location of the comet's north pole, play the most significant role in the differences between the morphology present in March, compared with that in April. The location of the Sun in April is approximately 70°N cometocentric latitude. Thus, any 'active' areas below $\approx$ 20°S latitude on the comet are never exposed to the Sun and therefore are not active in April. Translating the best-fit pole (with respect to the April data) to March places the Sun at a cometocentric latitude of approximately 40°N which allows a much greater area of the comet's southern hemisphere jets to be exposed. Thus, it is likely that additional areas on the nucleus that are not active during April were active during March. This might explain why the entire jet morphology in March is not reproduced with only the 5 active areas used to fit the April data.

4.5.2 Effect on Production Rates

We currently assume OH is an accurate tracer of the water production and that the parent of OH *is* H_2O. If grains are a significant contributor of OH, then assuming all OH comes from water is in error, and the current methods for translating OH abundances to water abundances must be re-evaluated. The Haser model is still widely used to estimate the water content of comets, and thus the effects of an extended source are investigated here.

Cometary production rates calculated by a Haser model are extrapolated from a finite aperture size to yield the total production rate (of a particular species) independent of aperture size. Therefore, measured production rates should be independent of aperture size. However, the production rates calculated by a Haser model increase with increasing aperture size for all three gas species in our observations of Comet Hale-Bopp (Table 4-6). The Haser model has proven to work well with comets in the past, and has yielded consistent production rates with different aperture sizes. Therefore, there must be some characteristic of Comet Hale-Bopp in particular that causes this model to break down. One obvious difference between this and other comets is the observed acceleration in the coma. The Haser model assumption that the outflow velocity is constant is not valid for this comet. The velocity used in the Haser model (traditionally 1 km/s) is underestimated by an increasingly greater amount as the aperture and actual velocity both increase. Therefore, Q should be increasingly underestimated in the case of Comet Hale-Bopp as aperture increases. Physically, the volume density is smaller than it would be if the velocity were constant. This suggests that the Haser model should yield a *smaller* production rate with increasing aperture, which is opposite from that which is observed. Hence, another mechanism must be at work.

If an extended source is present, as is suggested by my results, then the production of radicals actually increases with increasing distance from the nucleus as the

sub-micron organic CHON grains heat up. This suggests that: a) the production rate actually *should* show an increase as the aperture increases, and b) the Haser model assumption that all the parents decay exponentially (which holds if the parent is a gas instead of a grain) is incorrect. The results from the Haser model support the need for an extended source that behaves differently than a nuclear gas source. They also suggest that a Haser model will overestimate the amount of parent *gas* molecules present in the coma if an extended *CHON* source is at work.

The change in Haser model production rates with aperture size reflects the fact that the contribution from a grain source increases with distance from the nucleus. Therefore, one might expect that the differences in total production rates calculated for different aperture sizes will be greater if a larger fraction of the radicals originate from a grain source. This is reflected in Q_p listed in Table 4-6. The total production rates of CN increase by a factor of 1.81 from the smallest to the largest aperture size listed while Q_p for OH and C_2 increases by factors of 1.5 and 1.6, respectively. Recall that roughly 65 to 75% of the CN, 35 to 45% of the OH, and 50 to 60% of the C_2 is created by grains as determined by the Monte Carlo modeling. When the Haser model is applied to *only the isotropic gas source* portion of the coma (as produced by my Monte Carlo models) with no additional contribution from a CHON grain source, the production rates do not change with aperture size. However, when applied to the model whose radicals are created *purely from the CHON grains*, the production rates increase (from the smallest to the largest aperture used) by factors of 2.3 for the OH, 4.4 for C_2, and 3.0 for CN. This demonstrates that the extended source is responsible for the change in production rates with aperture.

4.5.3 Composition of the nucleus and extended source

Both the nuclear and extended sources must be capable of producing OH, C_2, and CN, placing constraints on their compositions. The ratio of OH:C_2:CN, based on Haser model production rates applied to the data, is 200:17:1 if the smallest aperture

Table 4-6: Haser model production rates

Aperture Size (″)	OH	CN	C_2
27.5	1.8E+30	0.91E+28	1.5E+29
38.6	1.9E+30	1.0E+28	1.7E+29
55.1	2.2E+30	1.2E+28	1.9E+29
77.9	2.4E+30	1.4E+28	2.1E+29
109.7	2.7E+30	1.6E+28	2.4E+29

Note: the Haser model production rates, Q_p (molecules/s), of the data are listed as a function of aperture size. Aperture sizes were chosen to allow comparison with the production rates obtained with the photoelectric photometer and are standard sizes used in the Lowell Observatory Cometary Database.

size is used, or 165:14:1 based on the largest aperture. This suggests that the nuclear ices are more enriched in OH than the extended source since the grains contribute a higher percentage of radicals with increasing aperture (for the aperture sizes listed).

Analyzing each source separately through the Monte Carlo models is more informative and confirms this suggestion. The Monte Carlo model is actually a combination of a gas source + grain source. Thus, I can apply the Haser model to the gas source alone which yields insight into the relative ratios of these species in the nuclear ices. The relative production rates of OH:C_2:CN are 250:8:1 for the nuclear gas source. In contrast, the extended source yields 70:3.5:1 if the OH from all 5 active areas is taken into account, or 40:3.5:1 if the 5th active area, which is depleted in CN and C_2, is not included. This indicates that the nuclear gas source has a higher concentration of OH than the extended grain source (roughly 3.5 × higher) and a slightly higher concentration of C_2 (approximately twice as high). One would expect a higher OH fraction in the nuclear ices since H_2O ice is more abundant in comets than any other ice by at least two orders of magnitude (except for CO and CO_2).

4.5.4 Implications for the Heterogeneity of the Nucleus

Comparing jet strengths and locations indicates that three, or possibly four, active areas on the nucleus contain grains with the same relative abundances of OH,

CN, and C_2 (see Table 4-5). If only these four active areas existed, then one would assume that Comet Hale-Bopp was homogeneous. However, one bit of evidence suggests otherwise. The fifth active region, which produces roughly half of the OH that originates from CHON grains, cannot produce measurable quantities of CN and C_2 for the model to reproduce the carbon species jets. This OH-producing region, active area 5, is located at (-12,120). However, active area 4 (at (15, 120)), which produces a relatively small portion of the gas jets, exists at the same longitude as the fourth OH active region. I attempted to resolve the difference in latitude by shifting either the northern latitude region to a more southerly location consistent with the OH active area, or the reverse. Shifting either source by only $\sim 5°$ caused a noticeable (detrimental) difference in the morphology suggesting that the difference in locations is real. The differences in jet morphology between the OH and carbon species supports the possibility of a significant difference in the location(s) of at least one of the active areas.

The opening angle of active region 5 for OH is 120°. The opening angles for active area 4 are 60° and 90° for CN and C_2, respectively.[3] Because the opening angles are wider for all C_2 active areas, I suspect that the wider opening angle does not represent a larger physical area for active area 4, but rather compensates for the fact that this radical may be a granddaughter or great-granddaughter product. For OH, a wide opening angle is only necessary for active area 5 (compared with the other active areas producing OH), implying that region 5 is physically large. The active areas in my models are represented as spherically symmetric regions. This is probably not an accurate representation; active area 5's large opening angle may represent an elongated region that overlaps active area 4. Therefore, it is quite possible that

[3]Because active area 4 does not produce any noticeable morphology in the OH images, the opening angle cannot be constrained for OH.

these two regions actually represent one heterogeneous, elongated, active region of the nucleus that is depleted in CN and C_2 at southerly latitudes.

4.6 Summary

Jets are evident in images of OH, CN, and C_2 and are analyzed to study several aspects of the comet. An extended source, whose production peaks at some distance away from the comet, is responsible for the bulk of the jet morphology observed, as well as a portion of the diffuse component. All evidence currently points toward sub-micron organic CHON grains as the primary extended source. The effect that each input parameter has on Monte Carlo models was discussed. Estimates of the locations of the jets and the expansion velocity of the coma were given. Discussions were included regarding: (1) possible sources of the jet and diffuse components, (2) reasons why differences are observed in the morphology of each gas species, (3) the effect that an extended source has on Haser model production rates, and (4) possible indications that Comet Hale-Bopp is heterogeneous. Conclusions of this work, implications for spacecraft missions bound for comets, and the direction that future research in this area may take are discussed in the final chapter.

CHAPTER 5
CONCLUSIONS

5.1 Introduction

The nucleus of Comet Hale-Bopp has undergone processing with each passage into the inner solar system. The presence of several jets indicates that much of its surface is probably mantled, resulting in discrete active areas on the surface that produce the jets. The extreme depletion of CN and C_2 in one active area suggests that the coma is not produced by a completely homogeneous nucleus. This information invokes questions regarding how and where this comet formed, and how it evolved to its current state: Was the region where this comet formed in the solar nebula not fully mixed? Could the nucleus have collided and merged with another comet while in the Oort Cloud? Are the differences in the composition of the active areas related to how recently they were exposed to the sun's radiation? Future work on this, as well as other comets, may lead to answers to questions such as these that have arisen from this work.

This chapter summarizes the main results of this work, and answers the questions posed in the beginning of chapter 4. An extended grain source is the source of the gas jets. The number and locations of the active areas producing the OH, CN, and C_2 jets are constrained. Jets were used to calculate the projected expansion velocity, estimate the acceleration of the gas in the coma, and confirm the orientation of the comet's rotational pole. Monte Carlo models, in conjunction with the narrowband images of the comet, made possible a comparative study of both the composition of the nuclear and extended sources as well as their relative contributions to the coma. The models also explain why the morphology of the gas species varies.

5.2 New Results

Identification of gas jets. The majority of the results discussed here are unique and robust. Gas jets are clearly evident in the emission from OH, CN, and C_2 fluorescence. These gas jets extend to projected distances as great as 125,000 km from the nucleus of Comet Hale-Bopp, which is within the collisional zone of this comet. This is the first time OH jets have been observed without spatially coincident dust jets in any comet, and this is the first comparative study of jets in these three gas species. The gas jets can best be explained by a hot, sub-micron CHON grain extended source, which peaks in productivity at some distance from the nucleus.

Explanation of anti-sunward gas jets. Dust jets were also observed, but were mainly present in the sunward direction. Gas jets are evident in both the sunward *and* anti-sunward directions. The presence of gas jets in the anti-sunward direction does not require that a high thermal inertia be invoked to allow production of gases throughout the entire cometary night. Rather, the anti-sunward gas jets are produced by active areas that remain in twilight-like conditions throughout the day due to the orientation of the comet's rotational pole. These active areas, located near the comet's equator, have relatively low production rates that can sweep away sub-micron CHON grains, but not a significant number of the larger dust particles that reflect visible light efficiently.

Expansion velocities, jet widths, and the acceleration of the gas jets. Comet Hale-Bopp's high total production rates indicate that the collisional zone is very large (~240,000 km in radius). When collisions between hot hydrogen atoms (that result from the photodissociation of H_2O) and the heavier observed radicals occur, energy is transferred to the heavier radicals, which causes them to accelerate. The acceleration of the gas jets is observed as an increase in the projected expansion velocities with distance from the nucleus. This confirms that collisions affect the coma gases out to distances of at least 100,000 km. In all cases, the gas jets are approximately twice as

wide as the dust jets, and their expansion velocities, similarly, are twice as high. This suggests that the CHON grains responsible for producing the gas jets are very small since they are accelerated to much higher velocities than the larger dust particles detected in the continuum image's jets.

Locations of the nuclear active areas producing the gas jets. The general morphology of the OH, CN, and C_2 jets is similar; however, there are some differences. Five active areas on the surface of Comet Hale-Bopp are necessary to recreate the gas jet morphology and radial profiles extracted from the observations. The locations of the jets producing OH and CN are better constrained than those of C_2, in part because their morphology is more difficult to reproduce. Three of the active areas produce the same mixture of the three gas species. The mixture of a one active area is indeterminate, but may be the same. The fifth active area produces almost half of the jet-source OH, but no noticeable CN and C_2; this area may be physically connected with the active area that is at 13N latitude. This additional active area is responsible for the variations observed between the morphology of the OH jets and the CN and C_2 jets, and suggests that the comet's nucleus is heterogeneous.

Coma sources: extended CHON grain jet source + diffuse nuclear gas source. The morphology and radial profiles can only be reproduced by invoking a source whose productivity of the observed radicals peaks at some distance from the nucleus, combined with a diffuse nuclear gas source. The favored candidate for the extended source is sub-micron CHON grains for two reasons: 1) it is plausible that their production will increase as they move away from the nucleus and heat up, and 2) a significant population of small, hot grains were detected in the coma of this comet. Both the morphology and radial profiles that result from this combination are distinctly different from the jet morphology and radial profiles created by a) a purely nuclear gas source (producing both the jets and diffuse [isotropic] components), b) a diffuse gas source combined with an icy grain source, or c) a diffuse gas source plus a

CHON grain source whose productivity peaks at or near the nucleus. Both the morphology and radial profiles of the images demand that the extended source produces the bulk of the observed OH, CN and C_2 jets, but is only partially responsible for the total production of these species.

Relative composition of, and contribution from, the gas and grain sources. Through an analysis of these jets, I have constrained the composition of the gas and grain sources, and the relative contribution to the coma from each source. The relative ratios of OH:C_2:CN suggest that the grains are depleted in OH by a factor of 4 to 7, and depleted by a factor of 2 in C_2, compared with the nuclear gas source. Approximately 35 to 45% of the OH, 50 to 60% of the C_2, and 65 to 75% of the CN gases originate from an extended source; these estimates are model dependent, and the ranges listed here indicate how the errors in the input parameters affect the estimates. The balance of the radicals is created by a molecular gas source originating from the nucleus which may partially, but not fully, originate in the jets; the majority of the nuclear molecular source must be isotropic to accurately reproduce the morphology. These fractions are consistent with estimates of CO and CN originating from and extended source in Comet Halley (Eberhardt et al. 1987, Klavetter and A'Hearn 1994), and CO originating from an extended source in Comet Hale-Bopp (DiSanti et al. 1999). The need for a significant non-gaseous source is supported through an analysis with a Haser model and emphasizes that care must be taken when extrapolating production rates of daughter products to possible parent gases.

5.3 Directions for Future Work

Though once thought improbable, the existence of gas jets in the comae of comets is now well established for OH, CN, and C_2 radicals. The study of jets gives astronomers the ability to extract information from comets that is otherwise difficult

or sometimes impossible to obtain. This ranges from estimating expansion velocities in the coma, to determining the comet's rotation rate, to constraining the orientation of the comet's rotational pole, to characterizing the composition of both the nuclear ices and refractory grains. All of this information leads to a better understanding of the physics and chemistry responsible for producing a cometary coma.

The advent of CCD's has changed the face of cometary science over the past 20 years. Even more recent improvements in this technology have given us the ability to study comets using a wide range of wavelengths. During this time, only a few comets bright enough for jets to be detected have ventured close enough to both the Sun and the Earth for us to study. The techniques developed to study the jets of Comets Halley and Hale-Bopp can be improved and employed in future studies of comets that have yet to be discovered. The Lowell Observatory Cometary Database catalogs the production rates of comets observed over the last several decades, and has been used to characterize two compositional classes of comets. As we build up a database of comets displaying jets, we can use the information extracted from jets to further characterize comets with respect to their expansion velocities, rotation, the chemical and physical properties of both the gas and dust in the coma, and their activity levels as a function of their dynamic age. A database including the coma's expansion velocities and acceleration as a function of the total production rate of the comet will allow us to test our understanding of how collisions affect heating in the coma. The effects of collisions on the collimation of the jets can also be studied. We have observed jets well beyond the collisional zone in Comet Halley, and within the collisional zone for Comet Hale-Bopp. The catalog will allow us to compare production rates of radicals from CHON grains versus a nuclear gas source. Through studying the relative mixtures of radicals emitted by various active areas, we can determine whether most cometary nuclei appear to be homogeneous or heterogeneous. Furthermore, insight into the processes responsible for jets will help

guide the planning of spacecraft missions to future comets, including those spacecraft that are already on their way to comets as well as those that are in the planning stages of the mission.

Comets are tiny testaments to the origin of the solar system. We are beginning to understand how the interaction of sunlight with the nuclear ices and grains affect the coma. We can use this information to piece together the puzzle of what comets are, how they formed, what the composition of the early solar nebula may have been like, and perhaps where the organics and water necessary for life here on Earth may have originated. An armada of spacecrafts are being designed and sent, within the next decade, to these building blocks of the solar system to yield new insight to the history of the Earth and the solar system we call home.

APPENDIX A
DUST PRODUCTION ($Af\rho$)

As a measure of the relative rate of cometary dust production, A'Hearn has developed the parameter $Af\rho$ which is independent of the aperture size (A'Hearn et al., 1984). The equation used to estimate $Af\rho$ is

$$F_{obs} = f_i n = \frac{nF_o \sigma A(\theta)}{4\pi \Delta^2 r^2} \tag{A-1}$$

where F_{obs} is the total flux observed, f_i the total flux per particle, n is the number of particles, F_o is the flux from the sun at 1AU (the Solar constant), σ the cross section of a particle, $A(\theta)$ the albedo of a particle, $F_o\sigma$ the amount of signal intercepted by a particle, $F_o\sigma A(\theta)$ the amount of scatter, 4π is included to normalize this quantity over 4π ster, and Δ is the distance from the comet to the Earth.

Regrouping A-1 yields

$$n\sigma A(\theta) = 4\pi \frac{F_{obs}}{F_o} \Delta^2 r^2 \tag{A-2}$$

Defining a surface area filling factor, f, as

$$f = \frac{cross\ section\ of\ grains\ in\ the\ FOV}{area\ of\ FOV} = \frac{n(\rho)\sigma}{\pi \rho^2} \tag{A-3}$$

where ρ is distance from the the nucleus and

$$A(\theta) f\rho = 4 \frac{F_{obs}}{F_o} \frac{\Delta^2 r^2}{\rho} \tag{A-4}$$

which estimates the total dust production, independent of aperture size, just as production rates are used to estimate the total number of gas molecules produced per second.

APPENDIX B
THE HASER MODEL

The Haser model is used to estimate the total production rates (molecules/s) of gas outflowing from a comet by extrapolating the signal detected in a finite aperture. The basic assumptions behind this model include (1) a constant, spherically symmetric, collisionless, radial outflow producing Q_p parents per second, (2) daughter products created solely by photodissociation from one parent, and (3) daughter species with the same speed (v) and direction as the parent particles. It is understood that while this model is physically simplistic, however, it does a credible job of estimating the production rates, is computationally inexpensive, and is still widely used today.

The underlying theory assumes that the production rate, Q_p, is related to the velocity, v, scalelengths of the parent, l_p, daughter, l_d, and the column density of particles, $n(\rho)$ at a projected distance, ρ, from the nucleus. The scalelength is the characteristic distance a particle moves before it is destroyed via photodissociation.

Upon setting up the equations to relate the creation and destruction of molecular species, Haser recognized that Bessel functions, $K_o(y)$, represented the solution to the equation of the loss of species X:

$$n(\rho) = \frac{Q_p}{2\pi\rho v} \int_{\rho/l_p}^{\rho/l_d} K_o(y)dy \qquad \text{(B-1)}$$

where $K_o(y)$ is the ordinary Bessel function of the first kind.

For the parent, the density at a distance r is given by:

$$n(r) = \frac{Q_p}{4\pi r^2 v}\, e^{-r/l_p} \qquad \text{(B-2)}$$

For the daughter, the density is:

$$n(r) = \frac{Q_p}{4\pi r^2 v} \frac{l_p - l_d}{l_d} (e^{-r/l_p} - e^{-r/l_d}) \tag{B-3}$$

Our observations give N(r), the number of molecules within a column of finite cross section,

$$N(r) = \int_0^r 2\pi\rho n(\rho) d\rho \tag{B-4}$$

From this we can translate our observations to production rates using:

$$N(r) = \frac{Q_p r}{v} \left[\int_{r/l_p}^{r/l_d} K_o(y) dy + \frac{l_d - l_p}{r} + K_1\left(\frac{r}{l_p}\right) - K_1\left(\frac{r}{l_d}\right) \right] \tag{B-5}$$

REFERENCES

A'Hearn, M. F. 1983. In Solar System Photometry Handbook. R. M. Genet (Ed.). Willmann-Bell, Inc. Richmond, VA.

A'Hearn, M. F., P. V. Birch, and D. A. Klinglesmith 1986b. Gaseous jets in Comet P/Halley. Proc. of the 20th ESLAB Symposium on the Exploration of Halley's Comet, Heidelberg, West Germany **1**, 483-486.

A'Hearn, M. F., S. Hoban, P. V. Birch, C. Bowers, R. Martin, and D. A. Klinglesmith 1986a. Cyanogen jets in Comet Halley. *Nature* **324**, 649-651.

A'Hearn, M. F., D. G. Schleicher, P. D. Feldman, R. L. Millis, and D. T. Thompson 1984. Comet Bowell 1980b. *Astron. J.* **89**, 579-591.

Alvarez, L. W., W. Alvarez, F. Asaro and H. V. Michel 1980. Extraterrestrial cause for the Cretaceous-Tertiary extinction. *Science* **208**, 1095.

Alvarez, W., J. Smit, W. Lowrie, F. Asaro, S. V. Margolis, P. Claeys, M. Kastner, and A. R. Hildebrand 1992. Proximal impact deposits at the Cretaceous-Tertiary Boundary in the Gulf of Mexico: A restudy of DSDP Leg 77 Sites 536 and 540. *Geology* **20**, 697-900.

Biver, N., D. Bockelée-Morvan, P. Colom, J. Crovisier, B. Germain, E. Lellouch, J. K. Davies, W. R. F. Dent, R. Moreno, G. Paubert, J. Wink, D. Despois, D. C. Lis, D. Mehringer, D. Benford, M. Gardner, T. G. Phillips, M Gunnarsson, H. Rickman, A. Winnberg, P. Bergman, L. E. B. Johansson, and H. Rauer 1997. Long term evolution of the outgassing of Comet Hale-Bopp from radio observations. *Earth, Moon, Planets* **78**, 5-11.

Blum, J. D., C. P Chamberlain, M. P. Hingston, C. Koeberl, L. E. Marin, B. C. Schuraytz, and V. L. Sharpton 1993. Isotopic comparison of K/T boundary impact glas with melt rock from the Chicxulub and Manson impact structures. *Nature* **364**, 325-327.

Bockelée-Morvan, D., D. Gautier, D. C. Lis, K. Younge, J. Keene, T. Phillips, T. Owen, J. Crovisier, P. F. Goldsmith, E. A. Bergin, D. Despois, and A. Wootten 1998. Deuterated water in Comet C/1996 B2 (Hyakutake) and its implications for the origins of comets. *Icarus* **133**, 147-162.

Bredichin, T. 1903. Mechanische untersuchungen uber cometenformen in systematischer darstellung. In *Voss' Sortiment*, R. Jaegermann (Ed.), 83-97. St. Petersburg, Leipzig.

Budzien, S. A., M. C. Festou and P. D. Feldman 1994. Solar flux variability and the lifetimes of cometary H_2O and OH. *Icarus* **107**, 164-188.

Campins, H., D. W. McCarthy, S. R. Stolovy, S. D. Kern, S. M Larson, N. H. Samarasinha, and A. Ferro 2000. Comet Hale-Bopp in Outburst: Imaging the Coma and the Nucleus with HST's NICMOS. *Bull. Am. Astron. Soc.*, in press.

Campins, H., G. H. Rieke, and M. J. Lebofsky 1983. Ice in Comet Bowell. *Nature* **301**, 405-406.

Carlson, R. W. 1980. Photo-sputtering of ice and hydrogen around Saturn's rings. *Nature* **283**, 461.

Chang, S., D. Des Marais, R. Mack, S. L. Miller, and G. E. Strathearn 1983. Prebiotic organic synthesis and the origins of life. In *Earth's Earliest Biosphere: It's Origin and Evolution*, J. W. Schopf (Ed.), 53-92. Princeton University Press, Princeton, NJ.

Chyba, C. 1990. Seeding Earth – Comets, oceans and life. *Planetary Report* **10**, 20-23.

Chyba, C. F and C. Sagan 1997. In *Comets and the Origin and Evolution of Life*, P. J. Thomas, C. F. Chyba, and C. P. McKay (Eds.), 147-173. Springer-Verlag, New York.

Clairemidi, J., and G. Moreels 1990. Gaseous CN, C_2 and C_3 jets in the inner coma of Comet P/Halley observed from the Vega 2 spacecraft. *Icarus* **86**, 115-128.

Clairemidi, J., C. Laffont, P. Rousselot, and G. Moreels 1997. Jets and arcs in the three H-Comets: Halley, Hyakutake, and Hale-Bopp. *Bull. Am. Astron. Soc.* **29**, 1035).

Clairemidi, J., G. Moreels and V. A. Krasnopolsky 1990. Spectro-imagery of P/Halley's inner coma in the OH and NH ultraviolet bands. *Astron. Astrophys.* **231**, no. 1, 235-240.

Clairemidi, J., P. Rousselot, F. Vernotte, and G. Moreels 1992. Dust and gas jets: Evidence for a diffuse source in Halley's coma. Lunar and Planetary Inst., Asteroids, Comets, Meteors 1991, 129-132.

Cochran, A. L., and D. G. Schleicher 1993. Observational constraints on the lifetime of cometary H_2O. *Icarus* **105**, 235-253.

Colom, P., E. Grard, J. Crovisier, D. Bockele-Morvan, N. Biver, and H. Rauer 1997. Observations of the OH radical in Comet C/1995 O1 (Hale-Bopp) with the Nanay Radio Telescope. *Earth, Moon, Planets* **78**, 37-43.

Combi, M. R. 1987. Sources of cometary radicals and their jets – gases or grains? *Icarus* **71**, 178-191.

Combi, M. R., and A. H. Delsemme 1980. Neutral cometary atmospheres. I. An average random walk model for photodissociation in comets. *Astrophys. J.* **237**, 633-640.

Combi, M. R., and U. Fink 1997. A critical study of molecular photodissociation and CHON grain sources for cometary C_2. *Astrophys. J.* **484**, 879-890.

Combi, M. R., and W. H. Smyth 1988. Monte Carlo particle-trajectory models for neutral cometary gases. I. Models and equations. *Astrophys. J.* **327**, 1026-1043.

Combi, M. R., B. J. Bos and W. H. Smyth 1993. The OH distribution in cometary atmospheres – A collisional Monte Carlo model for heavy species. *Astrophys. J.* **408**, 668-677.

Combi, M. R., K. Kabin, T. I. Gombosi, D. L. de Zeeuw, and K. G. Powell 1997. Dust-gas interrelations in comets: Observations and theory. *Earth, Moon, Planets* **79**, 275-306.

Cosmovici, C. B., G. Schwarz, W. H. Ip, and P. Mack 1988. Gas and dust jets in the inner coma of Comet Halley. *Nature* **332**, 705-709.

Crovisier, J. 1984. The water molecule in comets – Fluorescence mechanisms and thermodynamics of the inner coma. *Astron. Astrophys.* **130**, 361-372

Crovisier, J. 1989. On the photodissociation of water in cometary atmospheres. *Astron. Astrophys.* **213**, 459-464.

Crovisier, J. 1999. Putting the CO in coma. *Nature* **399**, 640-641.

Crovisier, J., and T. Encrenaz 2000. *Comet Science*, Cambridge University Press, United Kingdom.

Delsemme, A. H. 1999. The deuterium enrichment observed in recent comets is consistent with the cometary origin of seawater. *Planet Space Sci.* **47**, 125-131.

Delsemme, A. H., and D. C. Miller 1971. The continuum of Comet Burnham (1960 II): The differentiation of a short period comet. *Planet. Space Sci. D. C.* **19**, 1229-1257.

DiSanti, M. A., M. J. Mumma, N. Dello Russo, K. Magee-Sauer, R. Novak and T. W. Rettig 1999. Identification of two sources of carbon monoxide in Comet Hale-Bopp. *Nature* **399**, 662-665.

Eberhardt, P., D. Krankowsky, W. Schulte, U. Dolder, P. Lammerzahl, J. J. Berthelier, J. Woweries, U. Stubbemann, R. R. Hodges, J. H. Hoffman, and J. M. Illiano 1987. The CO and N_2 abundance in Comet P/Halley. *Astron. Astrophys.* **187**, 481-484.

Eberhardt, P., M. Reber, D. Krankowsky, and R. R. Hodges 1995. The D/H and $^{18}O/^{16}O$ ratios in water from comet P/Halley. *Astron. Astrophys.* **302**, 301-316.

Edgeworth, K. E. 1949. The origin and evolution of the Solar System. *Mon. Not. R. Astron. Soc.* **109**, 600-609.

Ellis, T. A., and J. S. Neff 1992. A comparison of modeled and observed intensity profiles for C_2, C_3, CN, and the continuum for P/Halley. *Icarus* **97**, 99-110.

Farnham, T. L., D. G. Schleicher, W. R. Williams and B. R. Smith 1999. The rotation state and active regions of Comet Hale-Bopp (1995 O1). *Bull. Am. Astron. Soc.* **31**, 30.01.

Farnham, T. L., D. G. Schleicher, and M. F. A'Hearn 2000. The HB narrowband comet filters: Standard stars and calibrations. *Icarus* 180-204.

Festou, M. C. 1981a. The density distribution of neutral compounds in cometary atmospheres. I. Models and equations. *Astron. Astrophys.* **95**, 69-79.

Festou, M. C. 1981b. The density distribution of neutral compounds in cometary atmospheres. II. Production rate and lifetime of OH radicals in Comet Kobayashi-Berger-Milton. *Astron. Astrophys.* **96**, 52-57.

Finson, M., and Probstein R. 1968. A theory of dust comets. 1. Model and equations. *Astrophys. J* **154**, 327-380.

Gerard, E. 1990. The discrepancy between OH production rates deduced from radio and ultraviolet observations of comets. I - A comparative study of OH radio and UV observations of P/Halley 1986 III in late November and early December 1985. *Astron. Astrophys.* **230**, 489-503.

Gombosi, T. I., T. E. Cravens, and A. F. Nagy 1985. Time-dependent dusty gasdynamical flow near Cometary Nuclei. *Astrophys. J* **293**, 328-341.

Gombosi, T. I., A. F. Nagy, and T. E. Cravens 1986. Dust and neutral gas modeling of the inner atmospheres of comets. *Rev. of Geophysics* **24**, 667-700.

Hanner, M. S. 1981. On the detectability of icy grains in the comae of comets. *Icarus* **47**, 342-350.

Harris, W. M., M. R. Combi, R. K. Honeycutt, and B. E. A. Mueller 1997. Evidence for interacting gas flows and an extended volatile source distribution in the coma of Comet C/1996 B2 (Hyakutake) *Science* **277**, 676-681.

Hartman, W. K., D. J. Tholen, and D. P. Cruikshank 1987. The relationship of active comets, "extinct" comets, and dark asteroids. *Icarus* **69**, 33-50.

Haser, L. 1957. Distribution d'intensité dans la tête d'une cométe. *Bull. Acad. Roy. Belgique*, Classes des Sciences, Ser. 5, **43**, 740-750.

Hoban, S., N. H. Samarasinha, M. F. A'Hearn, and D. A. Klinglesmith 1988. An investigation into periodicities in the morphology of CN jets in Comet P/Halley. *Astron. Astrophys.* **195**, 331-337.

Huebner, W. F. (Ed.) 1990. *Physics and Chemistry of Comets*, Springer-Verlag, Berlin.

Ip, W. H. 1983. On photochemical heating of cometary comae: The cases of H_2O and C_2 rich comets. *Astrophys J.* **264**, 726-732.

Izett, G. A. 1991. Tektites in Cretaceous-Tertiary Boundary rocks on Haiti and their bearing on the Alvarez impact extinction hypothesis. *J. Geophys. Res.* **96**, 20879-20905.

Jessberger, E. K., and J. Kissel 1988. Aspects of the major element composition of Halley's dust. *Nature* **332**, 691-695.

Jessberger, E. K. and J. Kissel 1991. Chemical properties of cometary dust and a note on carbon isotopes. In *Comets in the Post-Halley Era*, R. L. Newburn and and M. Neugebauer (Eds.), 1075-92. Kluwer, Dordrecht, **2**.

Jewitt D., and J. Luu 1993. 1993 RO. *IAUC* **5865**.

Jorda, L, P. Lamy, O. Groussin, I. Toth, M. F. A'Hearn, S. Peschke 1999. ISO-CAM Observations of cometary nuclei. In *ISO Beyond Point Sources: Studies of Extended Infrared Emission*, R. J. Laureijs, K. Leech and M. F. Kessler (Eds.), 61. ESA-SP.

Jorda, L., K. Rembor, J LeCacheux, P. Colom, J. Colas, E. Frappa, and L. M. Lara 1997. The rotational parameters of Hale-Bopp for observations of the dust jets at Pic du Midi Observatory. *Earth, Moon, Planets* **77**, 167-180.

Kidger, M. R., M. Serra-Ricart, J. Licandro, R. Torres, L Schulman, J. N. Gonzalez-Perez 1998. A jet-related colour change in the inner coma of comet Hale-Bopp (1995 O1)? *Astron. Astrophys.* **329**, 1152-1155.

Kissel, J., D. E. Brownlee, K. Buchler, B. C. Clark, H. Fechtig, E. Grun, K. Hornung, E. . Igenbergs, E. K. Jessberger, F. R. Krueger, H. Kuczera, J. A. M. McDonnell, G. M. Morfill, J. Rahe, G. H. Schwehm, Z. Sekanina, N. G. Utterback, H. J. Volk, and H. A. Zook 1986a. Composition of Comet Halley dust particles from Giotto observations. *Nature* **321**, 336-337.

Kissel, J., R. Z. Sagdeev. J. L. Bertaux, V. N. Angarov, J. Audouze, J. E. Blamont, K. Buchler, E. N. Evlanov, H. Fechtig, M. N. Fomenkova, H. von Hoerner, N. A. Inogamov, V. N. Khromov, W. Knabe, F. R. Krueger, Y. Langevin, V. B. Leonas, A. C. Levasseur-Regourd, G. G. Managadze, S. N. Podkolzin, V. D. Shapiro, S. R. Tabaldyev, and B. V. Zubkov 1986b. Composition of Comet Halley dust particles from Vega observations. *Nature* **321**, 280-282.

Kitamura, Y., O. Ashihara, and T. Yamamota 1985. A model for the hydrogen coma of a comet. *Icarus* **61**, 278-295.

Klavetter, J. J. and M. F. A'Hearn 1992. CN jet velocity in Comet P/Halley. *Icarus* **95**, 73-85.

Klavetter, J. J. and M. F. A'Hearn 1994. An extended source for CN jets in Comet P/Halley. *Icarus* **107**, 322-334.

Krasnopolsky, V. A. 1991. C3 and CN parents in Comet P/Halley. *Astron. Astrophys.* **245**, 310-315.

Kuiper, G. P. 1950. Origin of the solar sytem. In *Astrophysics*, J. J. Hynec (Ed.), 357-424. McGraw Hill Book Co., New York.

Lamy, P., and J. M. Perrin 1988. Optical properties of organic grains: Implications for interplanetary and cometary dust. *Icarus* **76**, 100-109.

Lamy, P., L. Jorda, I. Toth, O. Groussin, M. F. A'Hearn, and H. A. Weaver 1999. Characterization of the nucleus of comet Hale-Bopp from HST and ISO observations. *Bull. Am. Astron. Soc.* **31**, 27.03.

Langevin, Y., J. Kissel, J. L. Bertaux, and E. Chassefiere 1987. First statistical analysis of 5000 mass spectra of cometary grains obtained by PUMA 1 (Vega 1) and PIA (Giotto) impact ionization mass spectrometers in the compressed modes. *Astron. Astrophys.* **187**, No. 1-2, 761-766.

Larson, S. 1988. Comet Halley: gas and dust jets in a spin. *Nature* **332**, 681-682.

Larson, S. M., and C. D. Slaughter 1991. Evaluating some computer enhancement algorithms that improve the visibility of cometary morphology. Lunar and Planetary Inst., Abstracts for the International Conference on Asteroids, Comets and Meteors, 1991, 131.

Larson, S. M., C. W. Hergenrother, and J. C. Brandt 1997. The spatial and temporal distribution of CO+ and CN in C/1995 O1 (Hale-Bopp). *Bull. Am. Astron. Soc.* **29**, 1036).

Lawler M.E. 1993. *Composition and properties of dust from Comet Halley.* Thesis (Ph. D.) Wash Univ., Seattle.

Lederer, S. M., H. Campins, D. J. Osip, and D. G. Schleicher 1997. Gaseous jets in Comet Hale-Bopp (1995 O1). *Earth, Moon, Planets* **78**, 131-136.

Licandro, J., L. R. Bellot Rubio, R. Casas, A. Gómez, M. R. Kidger, N. Sabalisk, P. Santos-Sanz, M. Serra-Ricart, R. Torres-Chico, A. Oscoz, L. Jorda, and G. Denicolo 1997. The spin axis position of C/1995 O1 (Hale-Bopp). *Earth, Moon, Planets* **77**, 199-206.

Lien, D. J. 1998. "CHON" particles: The interstellar component of cometary dust. *Exozodiacal Dust Workshop*, 282.

Lisse, C. M., Y. R. Fernández, M. F. A'Hearn, T. Kostiuk. T. A. Livengood, H. U. Kaufl, W. F. Hoffmann, A. Dayal, M. E. Ressler, M. S. Hanner, G. G. Fazio, J. L. Hora, S. B. Peschke, E. Grun, and L. K. Deutch 1997. Infrared observations of dust emission from Comet Hale-Bopp. *Earth, Moon Planets* **78**, 251-257.

Lovell, A. J. 1999. *Millimeter-wave molecular mapping of Comets Hyakutake and Hale-Bopp.* Thesis (Ph. D.) University of Mass.

Marconi, M. L. and D. A. Mendis 1982a. The photochemical heating of the cometary atmosphere. *Astrophys. J.* **260**, 386-394.

Marconi, M. L. and D. A. Mendis 1982b. The photochemistry and dynamics of a dusty cometary atmosphere. *Moon Planets* **27**, 27-47.

Marconi, M. L., and D. A. Mendis 1983. The atmosphere of a dirty-clathrate cometary nucleus: A two-phase multifluid model. *Astrophys. J.* **273**, 381-396.

Meier, R., T. C. Owen, H. E. Matthews, D. C. Jewitt, D. Bockelée-Morvan, N. Biver, J. Croviser, and D. Gautier 1998. A determination of the HDO/H2O ratio in Comet C/1995 O1 (Hale-Bopp). *Science* **279**, 842-844.

Mendis, D. A., H. L. F. Houpis, and M. L. Marconi 1985. The physics of comets. *Fund. Cosmic Phys.* **10**, 1-380.

Mueller, B. E. A., N. H. Samarasinha, and M. J. S. Belton 1997. Imaging of Comet C/1995 O1 (Hale-Bopp) on the WIYN with narrowband CN and continuum filters around perihelion (March-May 1997). *Bull. Am. Astron. Soc.* **29**, 1036).

Oort, J. H. 1950. The structure of the cloud of comets surrounding the Solar System and a hypothesis concerning its origin. *Bull. Astron. Inst. Neth.* **11**, 91-110.

Oró, J. 1961. Comets and the formation of biochemical compounds on the primitive Earth. *Nature* **190** 389-390.

Oró, J. 1999. Organic matter and the origin of life in the Solar System. Bioastronomy 99: A New Era in Bioastronomy. 6th Bioastronomy Meeting - Kohala Coast Hawaii August 2-6, 2999, 110.

Pearce, A. 2000. Comet C/1995 O1(Hale-Bopp). *IAUC* **7345**.

Press, W. H., B. P. Flannery, S. A. Teukolksy, and W. T. Vetterling (Eds.) 1992. In *Numerical Recipes in C: the art of scientific computing*, 195-199. Cambridge University Press, Cambridge, New York.

Rhode, J. R., and A. Sinclair 1992. Orbital elements and rings of satellites. In *Explanatory Supplement to the Astronomical Almanac*, P. K. Seidelmann (Ed.), 325-381. Nautical Almanac Offices, UK and USA, Jet Propulsion Laboratory, Bureau des Longitudes and the Time Service and Astrometry departments, U. S. Naval Observatory.

Rousselot, P., C. Laffont, J. Clairemidi, G. Moreels, and D. C. Boice 1997. Evolution of the activity of Comet Hale-Bopp (1995 O1) from August 1996 to April 1997. *Bull. Am. Astron. Soc.* **29**, 1036.

Sagan, C., and B. N. Khare 1979. Tholins: Organic chemistry of interstellar grains and gas. *Nature* **277**, 102-107.

Samarasinha, N. H. 1992. *Temporal and spatial inhomogeneities in comets.* Thesis (Ph. D.) Maryland Univ., College Park.

Samarasinha, N. H. 2000. The coma morphology due to an extended active region and the implications for the spin state of Comet Hale-Bopp. *Astrophys. J.* L107-L110.

Samarasinha, N. H., and M. S. Belton 1994. The nature of the source of CO in Comet P/Halley. *Icarus* **108**, 103-111.

Samarasinha, N. H. B. Mueller, and M. S. Belton 1997. Coma morphology and constraints on the rotation of Comet Hale-Bopp (C/1995 O1). *Earth, Moon, Planets* **77**, 189-198.

Sarmecanic, J., D. Osip, S. Lederer, M. Fomenkova, and B. Jones 1997. Constraints on the nucleus and dust of Comet Hale-Bopp. *Bull. Am. Astron. Soc.* **29**, 1034.

Schleicher, D. G., S. M. Lederer, R. L. Millis and T. L. Farnham 1997. Photometric behavior of Comet Hale-Bopp (C/1995 O1) before perihelion. *Science* **275**, 1913-1915.

Schulz, R., and M. F. A'Hearn 1995. Shells in the C_2 coma of Comet P/Halley. *Icarus* **115**, 191-198.

Schulz, R., M. F. A'Hearn, P. V. Birch, C. Bowers, M. Kempin, and R. Martin 1993. CCD imaging of Comet Wilson (1987VII) - A quantitative coma analysis. *Icarus* **104**, 206-225.

Sekanina, Z. 1991. Cometary activity, discrete outgassing areas, and dust-jet formation. In *Comets in the Post-Halley Era*, R. L. Newburn and and M. Neugebauer (Eds.), 769-823. Kluwer, Dordrecht, **2**.

Sekanina, Z. 1997. A Determination of the nuclear size of Comet Hale-Bopp (C/1995 O1). *Earth, Moon, Planets* **77**, 147-153.

Sekanina, Z. 1998. Modeling the diurnal evolution of a dust feature in Comet Hale-Bopp (C/1995 O1). *Astrophys. J. Lett* **494**, L121.

Sekanina, Z., and H. Boenhardt 1997. Dust morphology of Comet Hale-Bopp (C/1995 O1) II. Introduction of a working model. *Earth, Moon, Planets* **78**, 313-319.

Sharpton, V. L., and L. E. Marin 1997. The Cretaceous-Tertiary impact crater and the cosmic projectile that produced it. In *Near-Earth Objects, the United Nations International Conference*, J. L. Remo (Ed.), 353. Annals of the New York Academy of Sciences, **822**.

Smart, W. M. 1977. *Textbook on Spherical Astronomy.* Revised by: R. M. Green. Cambridge University Press, Cambridge.

Spray, J. G., S. P. Kelley, and D. B. Rowley 1998. Evidence for a late Triassic multiple impact event on Earth. *Nature* **392**, 171.

Tegler, S. C., and W. Romanishin 1998. Two distinct populations of Kuiper-belt object. *Nature* **392**, 49-51.

Tegler, S. C., and W. Romanishin 1999. Kuiper Belt Objects (Invited). *Bull. Am. Astron. Soc.* **31**, 23.01.

Vasundhara, R., and P. Chakraborty 1999. Modeling of jets from Comet Hale-Bopp (C/1995 O1): Observations from the Vainu Bappu Observatory. *Icarus* **140**, 221-230.

Wallace, L. V., and F. D. Miller 1958. Isophote configurations for model comets. *Astron. J.* **63**, 213-219.

Wickramasinghe, N. C., and M. K. Wallis 1994. The Cometary hypothesis of the K/T mass extinctions. *Mon. Not. R. Astron. Soc.* **270**, No. 2, P 420.

Xie, X., and M. J. Mumma 1996. Monte Carlo simulations of cometary atmospheres: Application to Comet P/Halley at the time of the Giotto spacecraft encounter. II. Axisymmetric model. *Astrophys. J.* **464**, 457-475.

BIOGRAPHICAL SKETCH

Susan Maria Lederer was born on the 29th of September, 1970 in Manitowoc, Wisconsin. She is the daughter of Kenneth K. Lederer and Kathryn M. (Schneider) Lederer. She has one brother, Matthew M. Lederer, two sisters, Katie K. Lederer and Jennifer S. (Lederer) Frederick, and one brother-in-law, Louis J.B. Frederick.

She attended Shawano High School during her first two years of high school, and graduated from Appleton High School West in 1988. She majored in both physics and mathematics at the University of Wisconsin Eau Claire, and earned a Bachelor of Science degree in 1992. During this time, she worked with Dr. Paul Thomas on image processing of Voyager data. She was awarded a National Science Foundation – Research Experience for Undergraduates (NSF REU) internship during the summer of 1991. She studied the air-burst deposits evident in the Magellan spacecraft's synthetic aperture radar (SAR) images under the guidance of Dr. Donald B. Campbell at Cornell University in Ithaca, New York. This opportunity instilled in her a love of planetary science research.

During the summer of 1994, she conducted research at NASA Ames Research Center in Mountain View, California, working with Dr. Kevin Zahnle, Dr. Eric Asphaug, Dr. Mark Marley, and Dr. Virginia Gulick. They studied the effects of atmospheric explosions on the surface of Venus as related to air burst deposits evident in images of Venus' surface. In 1995, she earned her M.S. degree in Astronomy at New Mexico State University, with a minor in Physics. Her masters thesis was entitled 'Consequences of Albedo Feature Inhomogeneities for Jovian Seismology.'

In 1995, she began working with Dr. Humberto Campins at the University of Florida. She spent nearly half of 1996 at Lowell Observatory in Flagstaff, Arizona

collecting data of both Comets Hyakutake and Hale-Bopp, the two brightest comets observed in the last two decades. Both Dr. David Osip and Dr. David Schleicher were instrumental in guiding her in observational astronomy during this time. During the summer of 1997, she attended the Vatican Observatory Summer School in Castel Gandolfo, Italy where she gained a fundamental background in comets, asteroids, and meteorites. Since this time, she has been funded under a NASA Graduate Student Researchers Fellowship studying the gas and dust jets evident in narrowband images of Comet Hale-Bopp that were collected at Lowell Observatory. In September, 2000, she completed her doctorate degree in astronomy and will begin a post-doctoral research associateship through the National Research Council (NRC) at the NASA Johnson Space Center in Houston, Texas in October, 2000. She will study the effects of aqueous alteration in Kuiper Belt Objects and Centaur asteroids with Dr. Faith Vilas.

I certify that I have read this study and that in my opinion it conforms to acceptable standards of scholarly presentation and is fully adequate, in scope and quality, as a dissertation for the degree of Doctor of Philosophy.

Humberto Campins , Chairman
Professor of Astronomy, Univ. of Ariz.

I certify that I have read this study and that in my opinion it conforms to acceptable standards of scholarly presentation and is fully adequate, in scope and quality, as a dissertation for the degree of Doctor of Philosophy.

Elizabeth Lada
Associate Professor of Astronomy

I certify that I have read this study and that in my opinion it conforms to acceptable standards of scholarly presentation and is fully adequate, in scope and quality, as a dissertation for the degree of Doctor of Philosophy.

Richard Elston
Professor of Astronomy

I certify that I have read this study and that in my opinion it conforms to acceptable standards of scholarly presentation and is fully adequate, in scope and quality, as a dissertation for the degree of Doctor of Philosophy.

Stanley Dermott
Professor of Astronomy

I certify that I have read this study and that in my opinion it conforms to acceptable standards of scholarly presentation and is fully adequate, in scope and quality, as a dissertation for the degree of Doctor of Philosophy.

Martin Vala
Professor of Chemistry

This dissertation was submitted to the Graduate Faculty of the Department of Astronomy in the College of Liberal Arts and Sciences and to the Graduate School and was accepted as partial fulfillment of the requirements for the degree of Doctor of Philosophy.

December 2000

Dean, Graduate School

LD
1780
2000
.L473